Thermal Model Development and Simulation of Cavity-Type Solar Central Receiver Systems

by

Lukas Feierabend

A thesis submitted in partial fulfillment of
the requirements for the degree of

Master of Science
(Mechanical Engineering)

at the
UNIVERSITY OF WISCONSIN – MADISON
2009

Approved by

_____
Professor Sanford A. Klein

_____
Professor Douglas T. Reindl

Date: _____

Abstract

The objective of this research is to develop a simulation tool that predicts the thermal performance of cavity-type central receiver systems for solar power towers that can be incorporated into the freely available *Solar Advisor Model* (SAM) software developed by NREL. SAM utilizes the TRNSYS simulation engine to calculate parts of the system performance.

In a solar-tower power plant, radiation from the sun is reflected by a heliostat field and focused onto heat absorbing receiver surfaces. The active receiver surfaces function as a heat exchanger that heats a working fluid (e.g. molten salt, steam). The thermal energy in the fluid is either directly or indirectly used to power a conventional steam cycle (i.e. Rankine Cycle). Therefore, the total thermal efficiency of the solar-tower power plant is the product of the efficiencies of each component: heliostat field, receiver, power cycle.

The developed model utilizes the main heat transfer mechanisms that determine the thermal efficiency of the cavity-type receiver. Radiation incident on the absorbing receiver surfaces is partially re-radiated to the surroundings. Additionally, the high surface temperatures cause significant convective heat losses out of the aperture of the receiver cavity. Black-body radiation heat transfer analysis and convective loss correlations found in the literature were applied in the receiver energy balances to determine the thermal energy gain in the heat transfer fluid.

The numerical model was programmed as a TRNSYS component in Fortran. It handles a range of different input parameters for the receiver geometry and the flow distribution of the working fluid flow through the receiver panels. Yearly simulations are based on solar radiation and weather data inputs from the TMY2 (typical meteorological year) database.

The developed cavity receiver model estimates annual thermal performances similar to the previously established cylindrical receiver model in SAM (Wagner, 2008). Contrary to previous expectations, the cavity shows higher convection heat losses than the external receiver model while neglecting the influence of wind on the total convective energy losses.

Assuming equal absorber areas for both receiver types, the inactive surfaces in the cavity are heated due to radiation exchange, and therefore provide additional hot surface area that contributes to higher thermal convection losses. On the other hand, the radiation heat losses from sheltering cavity designs can be reduced compared to the cylindrical, external receiver design.

Acknowledgments

The year and a half I spent studying at the Solar Energy Lab has greatly improved my ability as an engineer and researcher. Special gratitude is directed to my advisors Professor Sanford A. Klein and Professor Douglas T. Reindl. Their knowledge, motivation and interest were essential to the successful completion of this project and made it a very rewarding experience.

I also would like to thank the National Renewable Energy Laboratory and the DAAD (German Academic Exchange Service) for the financial support of my research. I am thankful to the NREL team for also providing their knowledge and input for this work. Especially Mike Wagner, a former SEL student, who always made himself available for discussion and questions about his work, knowledge and experience. Cliff K. Ho and Siri Sahib S. Khalsa from Sandia National Laboratories voluntarily contributed numerical flow simulations for verification of the presented model. I would like to thank them as well.

Thanks to all Solar Energy Laboratory members, especially my office mates Mike, Matt, Ty, Will, Amanda, Rote, and Mike, for their friendliness and helpfulness in any questions concerning studies and life.

Finally, I would like to thank my parents for their continuous support and encouragement.

TABLE OF CONTENTS

List of Figures

LIST OF TABLES

NOMENCLATURE

A	Surface area [m^2]
c	Specific heat [J/kg-K]
C	Constant factor [-]
D	Diameter [m]
F	Radiation view factor [-]
g	Gravitational constant [m/s^2]
Gr	Grashof number [-]
H	Height [m]
h	Heat transfer coefficient [W/m^2-K]
k	Thermal conductivity [W/m-K]
L	Characteristic length scale, also magnitude of ray between emitting surface and target surface for the ray tracing calculations [m]
l	Tubing section [m]
$\dot{m}$	Mass flow rate [kg/s]
N	Integer number for counting surfaces, tubes, and nodes
Nu	Nusselt number
p	Pressure [Pa]
P	Surface perimeter [m], also probability of number between 0 and 1 [-]

Pr	Prandtl number [-]
$\dot{q}$	Heat flux [W]
$\dot{q}"$	Area-specific heat flux [W/m^2]
R	Radius [m], also heat transfer resistance [K/W]
Ra	Rayleigh number
Re	Reynolds number
Ri	Richardson number
T	Temperature [K]
u	Velocity [m/s]
V	Wind velocity [m/s]
W	Width [m]
x	Length section for receiver angle calculations, also coordinate for ray tracing method [m]
y	Coordinate for ray tracing calculations [m]
z	Coordinate for ray tracing calculations [m]

GREEK LETTERS

α	Angle between two surfaces for the view factor calculations, also angle between the panel sections of the receiver cylinder [rad]
β	Volume expansion coefficient of air [1/K]
Δ	Finite difference
ε	Surface emissivity [-]
Φ	Inclination angle in the spherical coordinate system [rad]
η	Efficiency [-]
μ	Dynamic viscosity [Pa-s]
ν	Kinematic viscosity [m^2/s]
θ	Receiver angle, also azimuth angle in the spherical coordinate system [rad]
ρ	Density [kg/m^3]
σ	Stephan-Boltzmann constant [$W/m^2\text{-}K^4$]

SUBSCRIPTS

∞	Ambient conditions
amb	Ambient conditions
A	Receiver aperture
avg	Averaged value
b	Bulk mass of air inside the receiver cavity
bends	Tube bends in each receiver panel
bn	Beam normal
coils	Coiling of the tubes in a single receiver panels
cond	Conduction
conv	Convection
c	Air flow leaving the receiver
cold	Cold receiver coolant inlet temperature
cz	Convective zone of the cavity receiver
dp	Dew point
e	Electric
field	Heliostat field
flow	Coolant flow
helio	Heliostat
hot	Desired hot coolant outlet temperature

HTF	Heat transfer fluid
in	Inlet/Inflow
inc	Incident radiation
L	Characteristic length
lam	Laminar flow regime
loss	Mixed heat losses
node	Single surface node
nodes	Vertical surface nodes per panel
out	Outflow
P	Panel
pump	Tower coolant pumping system
rad	Radiation
rec	Receiver
s	Interior cavity surface
solar	Solar radiation from the heliostat field
st	Stagnant zone of the receiver
t	Tubing in the convective zone of the cavity receiver, also thermal used for thermal power
temp	Temperature
thermal	Thermal
total	Total interior cavity area, also total radiation power

tower	Total tower height
trans	Transition between laminar and turbulent flow
tube	Denotes single receiver tube
tubes	Denotes the tube bundle in a single receiver panel
turb	Laminar flow regime
w	Wall
X	Denotes guess value

ACRONYMS

CFD	Computational Fluid Dynamics
CPU	Central Processing Unit
CRL	Critical Radiation Level
CRS	Central Receiver System
CSP	Concentrating Solar Power
EES	Engineering Equation Solver
HTF	Heat Transfer Fluid
IEA	International Energy Agency
IR	Infrared radiation
LEC	Levelised Energy Cost
NREL	National Renewable Energy Laboratory
PS	Planta Solar
PTGen	Power Tower Generator
RN	Random number between 0 and 1
SAM	Solar Advisor Model
TMY	Typical Meteorological Year
TRNSYS	Transient Energy System Simulation Tool
DOE	United States Department of Energy

1 Introduction

Solar energy technologies have the potential to play a significant role in the world's energy future. Among a mix of other renewable energy sources, it can provide a long-term solution for "carbon-neutral" and sustainable electricity generation. There are currently two approaches for generating electricity from solar energy: conversion of solar radiation directly into electricity (via photovoltaic panels) and conversion of solar radiation into a high temperature fluid stream that can serve as the "fuel" source for conventional power plant cycles. Large-scale solar-thermal power generation is best accomplished with concentrating solar power systems (CSP) that focus the direct solar irradiation with mirrors onto surfaces that transfer the thermal energy into a heat transfer fluid. The fluid drives a conventional power cycle. Four competing CSP designs have shown successful application either for demonstration projects or commercial purposes.

1.1 CSP Technology

1.1.1 Parabolic Trough Systems

Currently, CSP power plant designs based on parabolic trough collectors account for the largest renewable-based electrical power capacity worldwide. The parabolic trough technology employs long rows of single-axis sun tracking parabolic concentrating mirrors as shown in Figure 1.1. The mirrors focus and concentrate incident solar radiation on a linear heat absorbing target (a pipe) that conveys a liquid heat transfer fluid. To reduce the convective heat losses from the heat collection element, an evacuated tube can be installed around the inner tube containing the working fluid. Synthetic oils are commonly used due to their low freezing temperature (14°C) and advantageous heat transfer properties. Disadvantages of the oil-use include high capital cost and fluid temperature restrictions of a maximum temperature around 400°C, which reduces the efficiency potential of the steam cycle. Trough plants that incorporate storage capacities often have a separate cycle that

utilizes molten salts as the storage medium. This indirect thermal storage further increases the total plant investment costs because of the additional heat exchangers. Therefore, research to identify and develop molten-salt mixtures with sufficiently low freezing points (B. Bradshaw, personal communication, October 15, 2009) that can be directly pumped into the storage tanks after being heated in the receiver elements is ongoing. The ability to store thermal energy is important to better match the production of electricity with demands for electricity that occur during periods when solar radiation is not available. Storage units that provide up to 16 hours of electricity generation will establish these large-scale CSP systems as competitors for base-load electricity generation. Due to a high deployment capacity compared to the other solar-thermal power systems, the industry has gained a substantial amount of experience with the parabolic trough systems and therefore the risks are relatively small.

Figure 1.1: 30 MW parabolic trough SEGS plant in Kramer Junction, CA (Patnode, 2006)

1.1.2 Linear Fresnel Systems

Similar to the parabolic trough system, the linear Fresnel collector heats a linear receiver element that carries a liquid or gaseous heat transfer medium (usually water/steam). Instead of parabolic concentrators, the solar radiation is reflected by a series of parallel arranged, long and flat mirrors that focus the radiation on a single line-collector that is placed above the mirror field as shown in Figure 1.2. Studies(Häberle, et al., 2002) indicated that linear Fresnel collector systems achieve only approximately 70% of the thermal efficiencies accomplished with parabolic trough systems. But due to simpler component geometry and mechanics the capital and operating costs are also lower compared to the trough technology.

Figure 1.2: Compact linear Fresnel collector in Bakersfield, California by Ausra

1.1.3 Central Receiver Systems

Solar tower power plants are in the class of central receiver systems that employ an elevated solar receiver that becomes the focal point of a field of mirrors (heliostats) that concentrate the radiation onto the heat absorbing surfaces of the receiver as shown in Figure 1.3. The receiver surface is usually constructed with welded absorber tubes that absorb the concentrated solar radiation from the heliostat field and transfer the absorbed thermal energy to a coolant that is pumped through the tubing system. The high temperature heat transfer fluid can then be used to drive a conventional power cycle or stored in tanks for later use. Successful operation has been shown for receivers and storage systems that operate with molten salts or steam as the working fluid. Molten salt is liquid across the typical operating temperature ranges of 290-560°C. Therefore, it requires less volume capacity and capital costs to store the same amount of energy as for a pressurized steam storage system. Because of the relatively low freeze point temperature, careful operation is required to make sure that the salt does not solidify in the receiver when the solar flux levels become too low. Parabolic trough systems like the Andasol 1-3 plants in Spain (Solar Millennium, 2008) use synthetic oil as the heat carrier in the mirror field and either transfer the heat directly to the boiler of the power cycle to produce steam, or the heat is stored in molten salt storage tanks for later use. This requires an additional heat exchanger to thermally connect the oil and the salt cycle. In contrast, power towers usually operate under higher fluid temperature ranges that simplify the application for available molten salt mixtures in the receiver. The heated molten salt is directly pumped into the storage tank, which saves the additional heat exchanger and reduces the investment costs compared to the trough technology with indirect thermal storage.

The tower technology has the potential for higher overall thermal collection efficiencies compared to the previously mentioned technologies because a large solar flux from the heliostat field is concentrated on the comparatively small surface area of the central receiver. Since the losses of the receiver depend on its geometry and the receiver surface temperatures, the losses are not proportionally affected by the solar flux levels. Due to the highly

concentrated solar radiation it is also possible to achieve higher temperatures of the working fluid, which increases the efficiency of the power conversion cycle. However, higher temperatures of the working fluid lead to higher surface temperatures and therefore to higher thermal losses of the receiver. This tradeoff must be optimized. These considerations are currently limited by the maximum bearable solar flux levels (1.2 MW/m^2 for Solar Tres (Lata, Rodriguez, & Lara, 2006)) of the materials used for the receiver and also the metallurgical restraints for maximum temperature in steam turbines. Research on approaches that will allow increasing the receiver flux limits as well as the development of high-efficiency supercritical steam turbines for the solar power tower plants that operate with steam temperatures up to 650°C (Sargent & Lundy LLC Consulting Group, 2003) is ongoing.

Figure 1.3: Abengoa's PS10 11MW solar power tower in Sanlucar la Mayor, Spain.

1.1.4 Dish-Stirling Systems

Dish-Stirling systems are compact CSP plants utilizing a concentrating surface ideally shaped like paraboloid of revolution that focuses the solar radiation onto a receiver located at the focal point of the dish mirror as shown in Figure 1.4. The small-scale cavity receiver transfers heat to a Stirling engine which converts the thermal energy to electrical energy. Due to their modular design, the systems provide flexibility for implementation in small-scale power generation as well as utility-scale electricity generation when installed in a field arrangement with large numbers of dish-Stirling modules. Unfortunately, the dish-Stirling technology does not provide economy of scale effects or optimized efficiencies for larger plant sizes because each module is a separate system with its own Stirling engine to generate power. Hydrogen is usually used as the working fluid in the Stirling engines and problems with leakage of the hydrogen were encountered in the past (Mancini, 1997). Water is not required for the energy conversion process in contrast to the conventional power cycles employed in the other CSP technologies. This is an advantage especially in warm, arid areas that have a high solar irradiance throughout the year but are also the most suitable for CSP plants due to their low flora and population density. Power generation systems that use the dish-Stirling technology operate under efficiencies of up to 30% (Sandia National Laboratories, 2008). In this case the efficiency is defined as the fraction of the total solar radiation hitting the mirror surface that is converted into electrical power. Despite the high conversion efficiencies, the technology is has not been proven competitive and reliable for long-term operation and large-scale applications. Another disadvantage is the lack of an inherent energy storage technology.

Figure 1.4: SES dish-Stirling systems at the Sandia Laboratory in Albuquerque, NM

1.1.5 CSP Technology Outlook

Although the currently installed and planned worldwide CSP capacity is mainly generated by parabolic trough plants, studies indicate that the power tower technology has a higher potential to reduce the cost of electricity. Today's electricity generation costs with the parabolic trough systems are around 15 US cents/kWh (Richter, Teske, & Short, 2009). A long-term study by Sargent & Lundy LLC Consulting Group (2003) shows that the levelised energy costs could be reduced by employing the tower technology to 3.5-5.5 cents/kWh by 2020, which is more than 10% lower than the estimated costs for electricity generated with a trough system of the same capacity. The strongest driver for the price reduction is expected to be the economy effects of large-scale utility plants. The major cost component for a solar tower power plant is the heliostat field with around 43% (for the Solar Tres plant) of the total direct costs (Sargent & Lundy LLC Consulting Group, 2003). Technology improvements and a high-volume production can decrease the costs significantly.

One of the problems for CSP plants is the condenser cooling in the power cycles. The suitable locations that experience a high solar irradiation throughout the year usually have

little water resources. Water is used in most conventional power plants to allow steam to condense at lower pressures, which increases the efficiency of the power cycle. Analyses (U.S. Department of Energy, 2008) show that air or hybrid wet/dry cooling can eliminate 80 to 90% of the water usage with an increase of the electricity production costs by approximately 2 to 9% depending on location and other assumptions. The study showed that for pure air cooling the electricity output drops around 4.5-5% for trough plants, but only 1.3% for power towers because higher steam temperatures were assumed.

In summary, the solar power tower technology shows feasibility from demonstration projects and one commercially operating power plant, the PS10 11 MW power tower in Sanlucar la Mayor, Spain, which is operated by Abengoa. The technology has been tested since 1981 with the Solar One project in the California Mojave Desert. By employing the technology with higher capacities and sufficient storage systems, the power tower technology among the trough systems can replace a significant fraction of critical base and peak load generating fossil fuel plants. Table 1.1 was found in the Global CSP Outlook summary for 2009 by SolarPACES, Greenpeace and ESTELA (2009).

Technology	PARABOLIC TROUGH	CENTRAL RECEIVER	PARABOLIC DISH	FRESNEL LINEAR REFLECTOR
Applications	Grid-connected plants, mid to high-process heat (Highest single unit solar capacity to date: 80 MWe. Total capacity built: over 500 MW and more than 10 GW under construction or proposed)	high temperature process heat (Highest single unit solar capacity to date: 20 MWe under construction, Total capacity ~50MW with at least 100MW under development)	Stand-alone, small off-grid power systems or clustered to larger grid connected dish parks (Highest single unit solar capacity to date: 100 kWe, Proposals for 100MW and 500 MW in Australia and US)	Grid connected plants, or steam generation to be used in conventional thermal power plants. (Highest single unit solar capacity to date is 5MW in US, with 177 MW installation under development)
Advantages	• Commercially available – over 16 billion kWh of operational experience; operating temperature potential up to 500°C (400°C commercially proven) • Commercially proven investment and operating costs • Modularity • Good land-use factor • Lowest materials demand • Hybrid concept proven • Storage capability	• Good mid-term prospects for high conversion efficiencies, operating temperature potential beyond 1,000°C (565°C proven at 10 MW scale) • Storage at high temperatures • Hybrid operation possible • Better suited for dry cooling concepts than troughs and Fresnel • Better options to use non-flat sites	• Very high conversion efficiencies – peak solar to net electric conversion over 30% • Modularity • Most effectively integrate thermal storage a large plant • Operational experience of first demonstration projects • Easily manufactured and mass-produced from available parts • No water requirements for cooling the cycle	• Readily available • Flat mirrors can be purchased and bent on site, lower manufacturing costs • Hybrid operation possible • Very high space efficiency around solar noon.
Disadvantages	• The use of oil-based heat transfer media restricts operating temperatures today to 400°C, resulting in only moderate steam qualities	• Projected annual performance values, investment and operating costs need wider scale proof in commercial operation	• No large-scale commercial examples • Projected cost goals of mass production still to be proven • Lower dispatchability potential for grid integration • Hybrid receivers still a R&D goal	• Recent market entrance, only small projects operating

Table 1.1: Comparison of main technology types for CSP (Richter, Teske, & Short, 2009)

1.2 Technology Overview

The focus of this project is on Central Receiver Systems using a sensible energy change working fluid (e.g. molten salt). Figure 1.5 illustrates the main components of a Central Receiver System operating with molten salts as the working fluid and a two-tank storage system for the hot salt at 565°C and the cold receiver inlet temperature of 290°C.

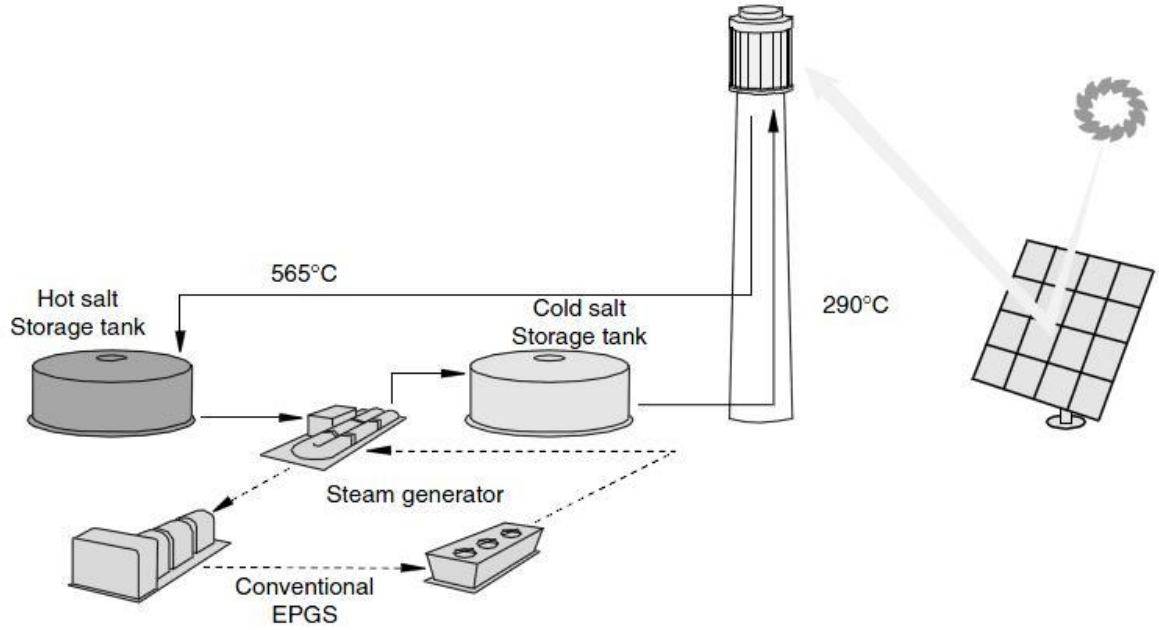

Figure 1.5: Scheme of a Central Receiver System (CRS) using molten salt as the working fluid (Romero-Alvarez & Zarza, 2007).

In the following discussion, electricity generating solar tower power plants will be subdivided into four different components:

- Heliostat field: An array of two-axis sun-tracking mirrors that are surrounding the tower focus solar radiation onto the receiver
- Receiver: The thermal energy from the solar radiation is transfer from the hot absorbing surfaces into a coolant that is pumped through heat exchanger tubes.

- Storage systems: The heated working fluid is stored in tanks. Cold fluid returning from the power cycle is usually stored in a separate tank containing the feed for the receiver.

- Power cycle: The heat from the coolant is used to power the steam boiler of the power cycle. This pressurized and hot steam is then expanded in turbines that drive generators to produce the electricity. In systems where the receiver working fluid is steam, the receiver acts as the boiler for the Rankine cycle and no intermediate heat exchanger is necessary (Figure 1.5). Otherwise the boiler is basically a heat exchanger that transfers thermal energy from the coolant (molten salt) to the working fluid of the power cycle (steam for Rankine cycles).

1.2.1 Heliostat Field

The heliostat field is makes up for approximately 40% of investment costs and the operational costs (Romero-Alvarez & Zarza, 2007) of the power tower. Each of the heliostats individually follows the solar azimuth and elevation angle relative to its specific position in the field so that the focal point is located on the receiver. Most heliostats have a rectangular mirror surface subdivided into multiple cant panels to reduce the influence of the heliostat size on the size of the image produced by a heliostat on the receiver. It is desired to reflect small heliostat images onto the receiver surface in order to aim precisely without spillage. Therefore, the cant heliostats are a Fresnel approximation to focusing. Heliostats are usually designed with a surface area of around $100m^2$. Figure 1.6 shows a single heliostat of the PS10 solar power plant in Spain.

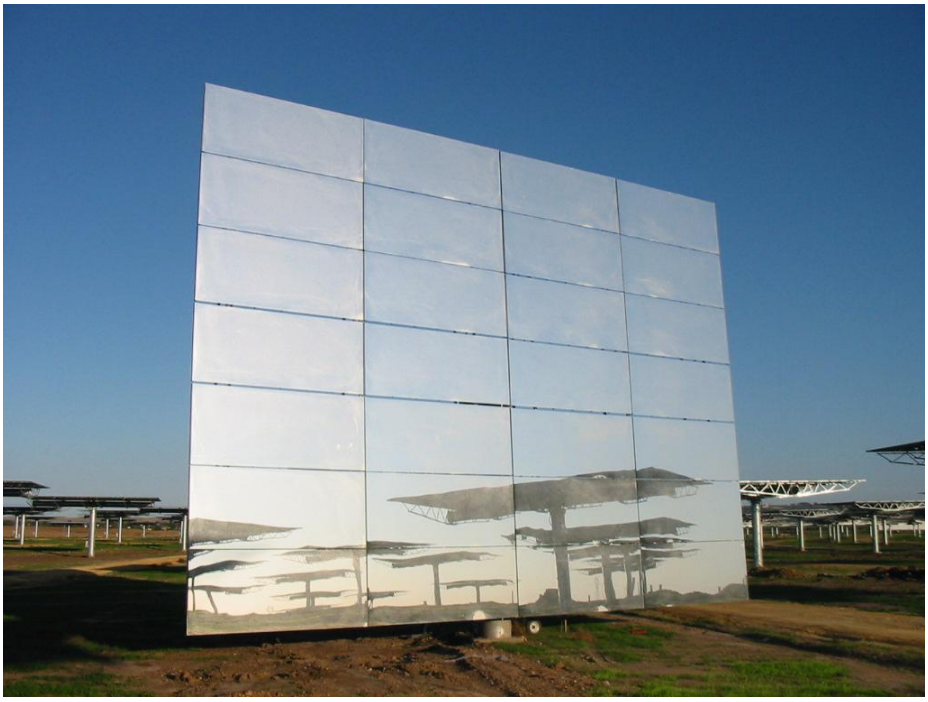

Figure 1.6: One of 624 Sanlucar 120 heliostats (120m^2) for the PS10 power plant (Abengoa).

Depending on the receiver design, the heliostat field can be completely surrounding the tower (cylindrical receiver design) or only cover the northern side of tower (cavity receiver). The aerial views in Figure 1.7 show the north-based field for the PS10 tower employing a cavity-type receiver technology and the surround field for the Solar Two plant that has a cylindrical receiver design.

Figure 1.7: Aerial views of the north-based heliostat field of the 11MW PS10 plant in Spain (left) and the surround field of the 10MW Solar Two plant in Daggett, California.

The layout for the field can be calculated by using a radial staggered method which is further explained in Wagner (2008). Codes like DELSOL3 by Sandia National Laboratories (Kistler, 1986) were developed to design and predict the field layout and performance, respectively, based on an optimized land use with reduced radiation losses due to mutual shading and blocking in between the heliostats. North-based heliostat fields are more efficient compared to surrounding fields because the surface area of heliostats located on the southern side of the receiver area is less effectively utilized than for the northern mirrors. This effect is called cosine attenuation because the effective area for reflection is reduced by a factor that is calculated as the cosine of half the angle between incoming and leaving radiation rays from the sun. Figure 1.8 illustrates the cosine effect. Additionally, a number of different losses occur during the energy transport from the incident solar radiation directly from the sun to the receiver surface regardless of the heliostat location. These are further explained in Section 3.1.

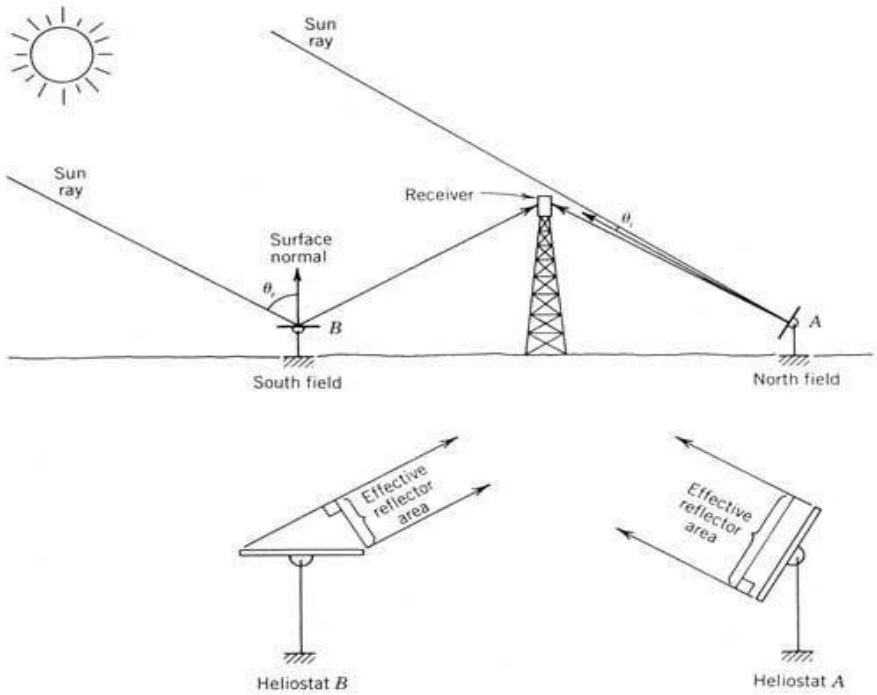

Figure 1.8: Effective reflector area reduction due to cosine effects (Stine & Geyer, 2001).

For the present study, the heliostat field is modeled with DELSOL3 and PTGen, a program to facilitate the use of the DELSOL code by Wagner (2008). For the transient simulation, a TRNSYS heliostat component originally developed by R. Pitz-Paal was modified by Wagner (2008).

1.2.2 Central Receiver

The receiver unit absorbs solar radiation reflected from the heliostat field and converts the concentrated radiation to thermal energy in a working fluid that can be used in power cycle. In general the receiver can be designed in two different ways:

1. Cylindrical, external receiver design as for the Solar Two (Pacheco, Reilly, Kolb, & Tyner, 2000) and Solar Tres (Ortega, Burgaleta, & Téllez, 2008) plants.

2. Cavity-type receiver design as for the PS10 solar tower (Solúcar, 2006).

In both cases, the irradiated surfaces heat a secondary fluid (e.g. molten salt) that is pumped through a welded tubing system that forms the active surfaces of the receiver. The external receiver of the Solar Two plant was constructed by a circular arrangement of 24 1m wide and 14m tall, rectangular panels where each is formed by 32 vertically aligned stainless steel tubes (Litwin, 2002). The complete surface area of the approximated cylinder serves as active heat absorption area. For the design of the receiver on top of the PS10 tower, the active tube panels form the absorbing surface inside of a shielded cavity. The radiation is focused on the aperture of the cavity such that the solar is distributed over the four adjacent panels that form the semi-cylindrical interior absorbing surface with a radius of 7m. Each panel has a height of 12m and is 5.38m wide (Solúcar, 2006).

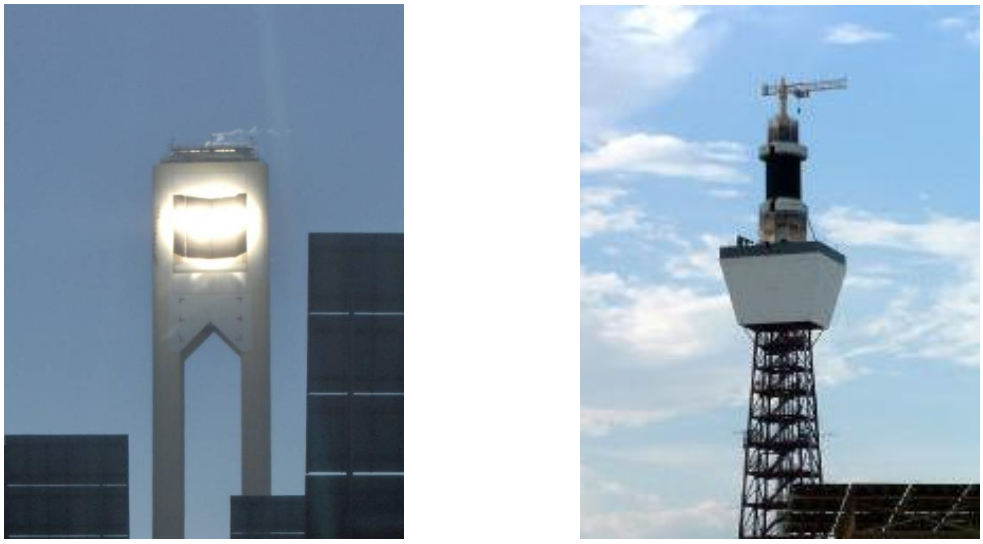

Figure 1.9: Cavity-type receiver design (left) of the PS10 plant in Sanlucar la Mayor, Spain; cylindrical receiver (right) of the Solar Two plant in Barstow, California

Both techniques have been successfully implemented in commercial and demonstration applications; however, a detailed performance study with sufficient experimental results from large-scale systems has not been reported in the literature at this point in time. Therefore, the differences in the thermal performance between both systems can only be estimated by using analytical techniques and experimental correlations established with approximated designs (see Chapters 2 and 3). It is widely believed that the cavity receiver design shields the hot surfaces from the surroundings and therefore reduces heat losses to the surroundings. Research and modeling for this project work show that this is true for the radiation losses from the receiver but not necessarily for the convection heat losses at low ambient wind conditions. Wagner (2008) developed a thermal model for external receiver designs. The objective of the present work is the development of an analogous model and TRNSYS component for cavity-type receivers. The availability of models of both designs provides an opportunity to compare their performances.

Apart from the tubular receiver design, research progress has been achieved with open volumetric air-cooled receiver designs (Romero-Alvarez & Zarza, 2007). Instead of conducting the heat to the coolant through tube walls as in tubular receivers, the concentrated solar radiation penetrates deeply into a porous structure which is cooled by an air stream that

flows through the pores of the absorbing medium (Figure 1.10). The main advantages are the free and fully available cooling air, no freezing risks, higher achievable outlet temperatures, no phase change, and a fast response to transient changes in the incident flux. Although the system indicates some advantages over the tubular receiver designs with liquid or steam coolants, successful operation in the past has shown that the thermal performance is not yet competitive to the tubular absorption design. This design approach is not further covered in the framework of the present research project.

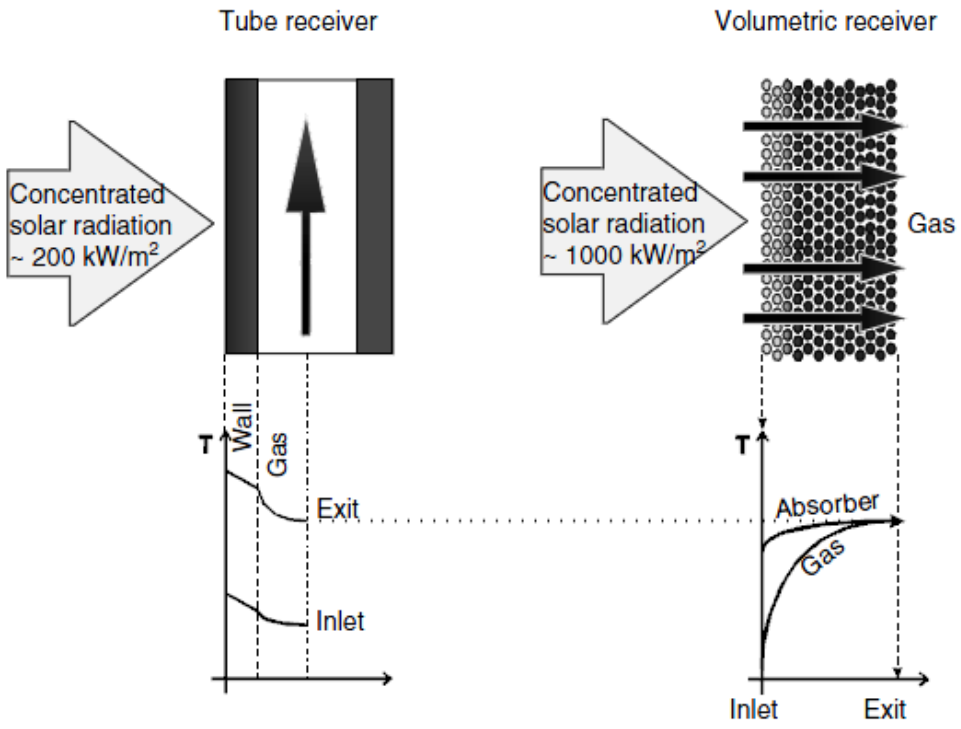

Figure 1.10: Heat transfer principles in tubular and volumetric receivers (Romero-Alvarez & Zarza, 2007)

1.3 Project Overview

The National Renewable Energy Laboratory in Golden, Colorado, is developing an integrated solar technologies analysis software tool known as “Solar Analysis Model” or

SAM. This tool allows NREL, outside researchers, and industry to examine a variety of solar technologies to better understand their performance, costs, value, and tradeoffs. SAM is capable of simulating and evaluating the performance of solar technologies including concentrating solar power (CRS), photovoltaic and solar heating. An existing transient renewable energy system simulation engine, TRNSYS (TRNSYS, 2009) has been selected to provide some of the system performance calculations within SAM. The TRNSYS engine was chosen because of the extensive existing solar modeling content within TRNSYS for all relevant technologies, the general acceptance of TRNSYS within the solar modeling community, its flexibility and modularity and the fact that it can be re-distributed freely once incorporated into SAM.

The main focus of this research project is the development of a thermal model for the cavity-type central solar receiver for future incorporation into SAM. The cavity receiver model is intended to provide SAM users an alternative to the cylindrical receiver. This numerical model was written in Fortran and computes the receiver's thermal performance. The model will rely on readily available input such as local weather data (hourly) along with user input parameters like plant location, desired power output, receiver geometry, etc. Based on the inputs, the model estimates the heat losses from the receiver and the transferred thermal energy to the working fluid.

A new TRNSYS component was established for the cavity receiver model which interacts with the existing solar power tower components. Several tests and comparisons were done to evaluate the performance and the behavior of the model. A steady-state comparison of a cavity receiver modeled in CFD and the TRNSYS model was conducted with Fluent (Fluent Inc., 2009) model results received through personal communication with the Sandia researchers Clifford K. Ho and Siri Sahib S. Khalsa (C. K. Ho and S. S. S. Khalsa, personal communication, 2009). The results of the simulations and comparisons indicate that the convection losses from a cavity receiver can be larger than those for a external receiver of comparable size.

⇗⇗2 Convective Heat Losses

The geometry of cavity-type receivers offers the potential to reduce long-wave radiation losses as well as convective heat losses compared to the external receiver type, where the active heat transfer surface is more exposed to the surroundings. In a cavity receiver, convective losses can be reduced because the absorbing surfaces are protected from direct wind influence and the heated air inside the cavity is inhibited from escaping to the environment by the ceiling construction. Furthermore, the radiation losses from the active surfaces are partly absorbed by inactive surfaces on the side walls, which reheat the air inside the cavity. Consequently, the air inside of the cavity is assumed to be at higher temperatures than the ambient air.

Convection losses can be separated into natural convection due to buoyancy and forced convection driven by ambient winds. A review of the literature shows a number of investigations on natural convection losses cavity receivers; however, most of those published studies are for small-scale cavity receivers found in dish-Stirling systems (Taumoefolau, Paitoonsurikarn, Hughes, & Lovegrove, 2004; Prakash, Kedare, & Nayak, 2008). Some papers also include studies on the heat losses from cavities due to wind velocity and direction (Ma, 1993; Prakash, Kedare, & Nayak, 2008). However, it is unclear whether these correlations can be confidently applied for the significantly higher wall temperatures and larger Rayleigh numbers that are present at central receivers of CSP towers.

2.1 Forced Convection Heat Losses

Based on a limited amount of experimental data, Clausing (1983) claims that the ambient wind influence on the convection is negligible at normal wind speeds (up to 8 m/s). Later experiments (Clausing, Lister, & Waldvogel, 1989) showed that inertia effects on convection become significant and the natural convection correlations may not be representative

anymore at Richardson numbers lower than 0.2. The range of Richardson numbers for central cavity receivers is usually in the range of 1-1000. The Richardson number is the defined as

$$Ri = \frac{Gr}{Re^{2}}, \tag{2.1}$$

and it represents the ratio of potential to kinetic energy. If it is greater than unity, buoyancy is the dominant flow driver. Ri numbers much lower than unity indicate that the convective effects due to flow is negligibly influenced by buoyancy. However, the influence of ambient winds on forced convection has not been sufficiently studied.

Experimental data from the Central Receiver Test Facility (Siebers & Kraabel, 1984) showed no systematic behavior of the convection losses due to the wind influence. On the other hand, Siebers and Kraabel (1984) mention that measurements from the IEA cavity receiver in Spain showed wind effects on the convective losses. For the present work, forced convection losses were neglected. If further studies show more reliable forced convection results, an additional term could be incorporated into the thermal receiver model.

2.2 Natural Convection Heat Losses

The amount of research conducted on free convection heat losses for large, central cavity receivers is very limited. Clausing (1983; 1989) has published analytical and experimental modeling results based on test cavities in the cryogenic wind tunnel of the University of Illinois at Urbana-Champaign. In his early paper (Clausing, 1983), Clausing presented natural convection heat transfer correlations that were updated with experimental work published in 1987. In addition to Clausing's correlations, Siebers and Kraabel (1984) reported an equation that solves for the heat lost through the aperture due to natural convection. The Nusselt number correlation reported by Siebers and Kraabel is derived from experimental work on cubical cavities reported by Kraabel (1983).

2.2.1 Siebers & Kraabel Convection Model

The Siebers & Kraabel (1984) Nusselt number correlation for the total convective heat loss from the receiver cavity to the ambient is defined by

$$Nu_L = 0.088\, Gr_L^{\frac{1}{3}} \left(\frac{T_w}{T_\infty}\right)^{0.18} \tag{2.2}$$

The correlation is applicable for Grashof numbers in the range: $10^5 \leq Gr \leq 10^{12}$. All properties in the dimensionless numbers are evaluated at ambient temperature. The characteristic length scale L in Equations (2.2) and (2.3) is the interior height of the receiver. The wall temperature T_w is the average of all internal cavity surface temperatures. The Grashof number is defined as

$$Gr_L = \frac{g\beta(T_w - T_\infty)L^3}{\nu^2} \tag{2.3}$$

The Nusselt number provides the heat loss coefficient $h_{conv,0}$.

$$h_{conv,0} = \frac{Nu_L\, k}{L} \tag{2.4}$$

The influence of an upper and lower lip as well as the receiver tilt angle is correlated with equation (2.5):

$$h_{conv} = h_{conv,0} \left(\frac{A_1}{A_2}\right) \left(\frac{A_3}{A_1}\right)^{0.63} \tag{2.5}$$

Figure 2.1 illustrates the area definitions A_1, A_2, and A_3. A_2 is the complete interior surface area A_1 minus the lower lip area. A_3 is the wall area below the horizontal plane passing through the bottom edge of the upper lip. The total convection losses are calculated with

$$\dot{q}_{conv} = h_{conv} A_w (T_w - T_\infty) \tag{2.6}$$

where A_w is the complete interior wall area.

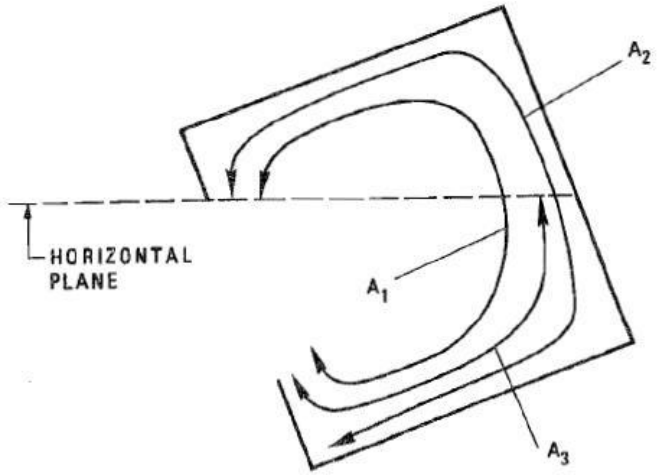

Figure 2.1: Area definitions to be used to account for the effect of tilt and aperture lips. Side wall areas are to be included (Siebers and Kraabel, 1984).

2.2.2 The Clausing Natural Convection Models

In his analysis of cavity receivers, Clausing (1983) indicated that the internal heat transfer resistances dominate the overall convective heat losses. In his analytical model, the wind velocity is considered in the bulk flow velocity inside the cavity. Additional studies point out that wind velocities lower than 8 m/s have negligible influence on the convective heat losses (Clausing, 1983). The basic idea behind the Clausing model is shown in Figure 2.2. It displays a simplified geometry for a cavity central receiver that is divided into two volumes, the stagnant zone and the convection zone. The hot receiver surfaces at the back wall are covered with heat transfer tubes that interact with air in the cavity. The heated cavity air rises and leaves the receiver through the upper portion of the aperture. This effect causes the development of an eddy flow in the convection zone as shown in Figure 5. Due to the large difference between surface and ambient temperatures, the density of air varies strongly over the vertical receiver length. The stratification due to the density gradient causes a stagnation of hot air in the region that is above the upper lip of the aperture.

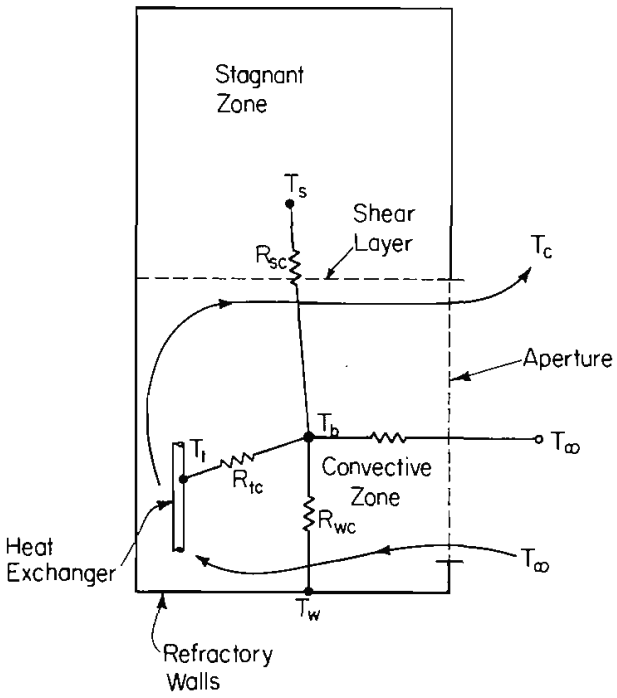

Figure 2.2: Side view of cavity showing the resistance network representation of heat loss mechanism (Clausing, 1983)

2.2.2.1 1983 Clausing Model

The circulating flow inside the cavity is mainly caused by buoyancy effects at boundary layers of the active surfaces; however, depending on its direction, incoming wind may affect this bulk flow. The lost energy from convection is associated with the heated air flow that exits the cavity through the aperture:

$$\dot{q}_{conv} = \rho_\infty u_1 C\, A_A\, c_{p,\infty}(T_c - T_\infty) \tag{2.7}$$

The air properties in (2.7) are evaluated at ambient temperature, T_∞. The aperture area, A_A, is multiplied by the constant factor $C = 0.5$. This approximation assumes that the incoming and out flowing air streams each occupy half of aperture area. u_1, the average velocity of the inflow, is a function of the wind velocity in the environment, u_∞, and the velocity u_2 to

which a fluid element near the back wall is accelerated over the vertically projected aperture height L_A due to buoyant forces,

$$u_1 = 0.5\left(u_2^2 + (0.5u_\infty)^2\right)^{\frac{1}{2}} \tag{2.8}$$

where $u_2 = \sqrt{g\beta(T_c - T_\infty)}$.

The resistance network model for the heat transfer processes in Figure 2.2 leads to an alternative expression for the convective term:

$$\dot{q}_{conv} = h_t A_t(T_t - T_b) + h_w A_w(T_w - T_b) + h_{st} A_{st}(T_{st} - T_b) \tag{2.9}$$

with $T_b = (T_\infty + T_c) \,/\, 2$

T_b is the temperature of the bulk air inside of the cavity's convective zone. It is approximated as the average of the incoming temperature T_∞ and the exiting air temperature T_c. The active tube area A_t, the inactive wall area A_w, the free shear layer area A_{st} and the aperture area A_A are known quantities of the receiver cavity. The corresponding temperatures, T_t, T_w, and T_s , are expected to be little influenced by the convective heat losses due to the large radiant solar and IR fluxes. The bulk temperature of the stagnant zone T_s is assumed to be the mean temperature of the active and inactive wall areas in the stagnant zone.

The area A_{st} is defined by the geometric boundary between convective zone and stagnant zone, which are separated by the horizontal plane that passes through the bottom edge of the upper lip. Treating the shear layer as an adiabatic wall provides a lower limit of the heat loss from the stagnant zone due to the air's poor conducting properties. LeQuere, Penot, and Mirenayat's data (1981) of experiments on natural convection from cubical cavities suggest the use of correlations for downward heated horizontal surfaces (Equation (2.10)) with a weighting factor 0.3 to adjust the coefficient to the reduced heat transfer shown in the experiments.

The heat transfer coefficients for the convective energy transport from the wall surfaces to the air inside the cavity are described by a Nusselt number correlation that Clausing (1983)

derived from experiments on vertical surfaces. The correlation accounts for the effect of variable properties due to a high temperature ratio T/T_∞, where T is the specific wall temperature.

$$Nu = 0.084\, Ra^{\frac{1}{3}} \left[-0.9 + 2.4 \left(\frac{T}{T_\infty} \right) - 0.5 \left(\frac{T}{T_\infty} \right)^2 \right] \cdot z(Z_w) \qquad (2.10)$$

$$Ra > 1.6 \times 10^9 \; ; \; 1 < T/T_\infty < 2.6$$

If the temperature ratio exceeds 2.6, it is recommended to use a value of 2 for the temperature polynomial until further data are available. However, at higher ratios the influence of $f(T/T_\infty)$ becomes less significant. $z(Z_w)$ is a function of the surface inclination Z_w, which is 0 for an upward facing horizontal surface.

$$\begin{aligned} z(Z_w) &= 1 && , 0 \le Z_w \le 135° \\ z(Z_w) &= \frac{2}{3}\left(1 + \frac{\sin(Z_w)}{\sqrt{2}} \right) && , 0 \le Z_w \le 135° \end{aligned} \qquad (2.11)$$

The Rayleigh number in correlation (2.10) is the product of the Grashof number and the Prandtl number:

$$Ra = Gr \cdot Pr = \frac{g\beta}{\nu\alpha}(T - T_\infty)L^3 \qquad (2.12)$$

The properties in equation (2.12) are evaluated at film temperature, the mean temperature of the corresponding surface temperature and the ambient temperature. For vertical walls, the significant length L is the height of the plate. If the plate is oriented horizontally, L needs to be calculated as the ratio of the surface area divided by the perimeter, which is $L = A/P$.

To solve the convective heat transfer problem, equations (2.7) and (2.9) are set equal at first to obtain the bulk air temperature.

2.2.2.1 1987 Clausing Model

In later studies, Clausing (1987) presented additional correlations to his initial model. The correlations were obtained from cryogenic wind tunnel experiments on cubical, isothermal cavities with a variety of aperture geometries. The cavity had a side length L_{cav} of only 0.4 m, but conditions were applied that are likely to represent the range of important dimensionless numbers (i.e. high wall to ambient temperature ratios T_w/T_∞ and large Rayleigh numbers) found in operating large-scale cavity receiver systems.

As in the initial model, the total convective heat losses are described with equation (2.7). Using the bulk temperature, that is $T_b = (T_c + T_\infty)/2$, instead of the temperature of the exiting air T_c, equation (2.7) becomes

$$\dot{q}_{conv} = C\ \rho_\infty u_2\ A_A\ c_{p,\infty}(T_b - T_\infty). \tag{2.13}$$

This model was developed for natural convection only. Thus, the mixed velocity u_1 (equation (2.8)) was replaced by the velocity u_2 due to buoyancy:

$$u_2 = \sqrt{2g\beta(T_b - T_\infty)} \tag{2.14}$$

For a better correlation with the obtained data, the constant C was changed to 0.36 instead of 0.5. In contrast to his first analytical model (Clausing, 1983), where multiple Nusselt number correlations were solved for heat transfer coefficients that determine the heat transfer from different single surfaces to the bulk air flow inside the cavity, the newer correlation determines only the heat transfer coefficient for the total convective losses out of the aperture. If not denoted otherwise, all properties are evaluated at film temperature. The Nusselt number is given as a function of gc, fc and bc, which are explained in detail below.

$$Nu = \frac{h\,L}{k} = gc \cdot fc \cdot bc \tag{2.15}$$

The rate of heat convection is defined by equation (2.16):

$$\dot{q}_{conv} = gc \cdot fc \cdot bc \cdot \frac{k}{L} \cdot A_{cz} \, (T_w - T_\infty) \tag{2.16}$$

A_{cz} is the convective zone area which represents the entire wall area below the shear layer plus the aperture area. Clausing chose this area to make the correlation independent of the geometry above the upper lip, the stagnant zone. Therefore, the wall temperature T_w in this model is the average of the active and inactive surface temperatures in the convective zone below the upper lip. The characteristic length, L, is defined as the height of the aperture L_A plus $L_{cav}/2$. For the experimental setup in Clausing's report, L_{cav} is defined as the side length of the cube that resembles the cavity. The reasoning for this definition of the length scale definition can be found in the original paper (Clausing, 1987). However, in the turbulent regime, the results are not dependent on the choice of L because in the corresponding correlation gc is a function of the Rayleigh number to the third power. Therefore, the characteristic length cancels out when solving for the heat transfer coefficient. The variable gc is a function of the Rayleigh number and accounts for natural convection from the interior surfaces to the air in the convective zone of the receiver operating at a bulk temperature T_b. The term fc accounts for the variable properties as a function of the Rayleigh number and the ratio of the averaged wall temperature and the ambient temperature T_w/T_∞. The following functional forms for fc and gc based on the flow regime.

<u>Laminar regime:</u> $Ra < 3.8 \times 10^8 \equiv Ra_{lam}$

$$gc = 0.63 Ra^{\frac{1}{4}}$$
$$fc_{lam} = 1 \tag{2.17}$$

Transitional regime: $Ra_{lam} < Ra < 1.6 \times 10^9 \equiv Ra_{turb}$

$$gc = 0.63Ra^{\frac{1}{4}}$$

$$fc_{trans} = (fc_{turb} - 1)\frac{Ra^{1/3} - Ra_{lam}^{1/3}}{Ra_{turb}^{1/3} - Ra_{lam}^{1/3}} + 1 \tag{2.18}$$

Turbulent regime: $Ra > Ra_{turb}$

$$gc = 0.108Ra^{\frac{1}{4}}$$

$$fc_{turb} = 0.2524 + 0.9163\frac{T_w}{T_\infty} - 0.1663\left(\frac{T_w}{T_\infty}\right)^2 \tag{2.19}$$

where $Ra = \frac{g\beta}{\nu\alpha}(T_w - T_\infty)L^3$

Function bc accounts for the difference between the convective heat transfer from the hot cavity walls to the heated bulk temperature instead of air at ambient temperature. That means, bc is unity if the bulk air mass inside the cavity is at the ambient temperature. The bulk temperature inside the cavity is higher than the ambient temperature, therefore bc will be in between 0 and 1.

$$bc = \frac{T_w - T_b}{T_w - T_\infty} \tag{2.20}$$

Equating the convective energy transport rates from equation (2.13) and (2.16) leads to an implicit expression for bc that must be solved iteratively:

$$bc = 1 - 1.57\left(\frac{gc \cdot fc \cdot bc\frac{k}{k_\infty}}{\sqrt{Ra_\infty Pr_\infty \frac{L_A}{L}\frac{A_a}{A_{cz}}}}\right)^{\frac{2}{3}} \tag{2.21}$$

2.2.3 Comparison Between the Convection Models

Due to the resistance network approach, the initial Clausing model can directly estimate the influence of the convective energy loss on the different surface temperatures inside the cavity. However, the Siebers & Kraabel model, as well as the newer Clausing correlation, only provides a heat transfer coefficient for the total convection rate out of the aperture, assuming an averaged isothermal wall temperature. The authors of all three presented models assume the convective losses have a negligible effect on the receiver surface temperatures due to the comparatively high solar radiation flux onto the receiver surfaces.

In order to compare the three presented models, the receiver model is initially solved without considering convection to the ambient. The resulting surface temperatures are then used to calculate the natural convection losses to the ambient. The comparison is conducted using the cavity receiver model, which is described in detail in Chapters 3 and 4. To calculate a realistic temperature distribution, a prototypical flux map with a total radiation of 44.95 MW was incident on the active receiver surfaces. The molten salt (60% $NaNO_3$/40% KNO_3) flows in parallel through each of the four panels from the bottom to the top with a fixed inlet and outlet temperature of 533 K and 866 K, respectively. The receiver model adjusts the mass flow rate in each panel to achieve the desired outlet temperature. The temperature range covers the operating extremes expected for this particular salt. At lower temperatures, the salt freezes and at temperatures in excess of 866 K, it decomposes. Each panel is vertically divided into 10 sub-surface nodes for calculating the black body radiation and heat transfer to the fluid. Fluid properties are evaluated at each node temperature (the nodal approach is further explained in Chapter 3). Figure 2.3 illustrates the receiver shape and the geometric quantities for this case.

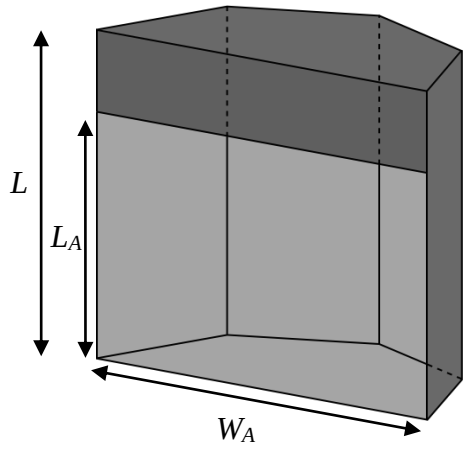

Item	Unit	Value
Interior height L	m	12.0
Aperture height L_A	m	9.0
Aperture width W_A	m	14.0
Convective zone area A_{cz}	m^2	388.2
Total interior area A_{total}	m^2	437.8
Aperture area A_A	m^2	126.0

Figure 2.3: Receiver geometry showing the significant values for the heat loss calculations

Table 2.1 shows the total incident solar radiation on the receiver ($\dot{q}_{inc}$), the thermal energy absorbed by the heat transfer fluid ($\dot{q}_{HTF}$), the thermal losses due to radiation ($\dot{q}_{rad}$), the thermal losses due to convection ($\dot{q}_{conv}$), the thermal efficiency of the receiver ($\eta_{thermal}$) the percentage of the convective losses relative to the total incident radiation (Conv. Per.), the percentage of the radiative losses (Rad. Per.), and the percentage difference in the convection heat losses between the models:

Conv. Diff. 1: Convection loss percentage differences of the 1983 Clausing model to the remaining two models

Conv. Diff. 2: Convection loss percentage differences of the 1987 Clausing model to the remaining two models

Conv. Diff. 3: Convection loss percentage differences of the Siebers & Kraabel model to the remaining two models

Model	$\dot{q}_{inc}$	$\dot{q}_{HTF}$	$\dot{q}_{rad}$	$\dot{q}_{conv}$	$\eta_{thermal}$
	kW	kW	kW	kW	
1983 Clausing	44950	40320	3298	1339	0.897
1987 Clausing	44950	39610	3298	2050	0.881
Siebers & Kraabel	44950	39680	3298	1972	0.883

Model	Conv. Per.	Rad. Per.	Conv. Diff. 1	Conv. Diff. 2	Conv. Diff. 3
	%	%	%	%	%
1983 Clausing	2.98	7.34	0.00	41.96	38.24
1987 Clausing	4.56	7.34	41.96	0.00	3.88
Siebers & Kraabel	4.39	7.34	38.24	3.88	0.00

Table 2.1: Results for simulations with three different convective heat loss models

Note that the surface temperatures are assumed to be negligibly affected by the convective losses for this comparison; therefore, the radiation losses to the surroundings are constant. The convection correlations estimate convection heat rates with relatively large differences. In particular, the initial Clausing correlation from 1983 predicts much smaller losses compared to the remaining models. The newer Clausing correlation and the Siebers and Kraabel model produce very similar results for these particular temperature conditions and geometry configuration.

The assumption of isothermal temperatures for the inner cavity surfaces, that is the influence of convective energy transport out of the aperture is neglected, was made without verification. To lend support to this assumption, two different application methods of the older Clausing model were compared. The first method assumes that convection has no effect on the wall temperatures (Isothermal Clausing); the second method solves the energy balances around each surface including the convective terms in order to estimate their effects on the surface temperatures (Non-isothermal Clausing). This comparison is only directly possible with the Clausing formulation from 1983 because heat transfer coefficients for the different wall zones in the cavity are determined. Therefore, the temperature change can be

iteratively calculated by including a convective loss term in the temperature node energy balances. Table 2.2 reports the results from the simulations that use the same model setup as for the results in Table 2.1.

	Isothermal Clausing		Non-isothermal Clausing		Difference
	kW	%	kW	%	%
$\dot{q}_{inc}$	4495	100.00	4495	100.00	0.000
$\dot{q}_{HTF}$	4039	89.85	4052	90.14	0.316
$\dot{q}_{rad}$	3298	7.34	3136	6.98	5.157
$\dot{q}_{conv}$	1340	2.98	1.296	2.88	3.395

Table 2.2: Comparison between simulation results applying the 1983 Clausing model

As expected, the convective losses are lower for the non-isothermal case, but the difference of less than 3.5% out of the approximately 3% convective heat losses of the total incident radiation is relatively small. The surface temperature drop affects the radiation losses more than the convection losses, but the total difference in heat losses of about 8.5% affects the total energy gain by less than a half percent. In conclusion, it is judged to be sufficiently accurate to calculate the energy transferred to the heat transfer fluid with radiation mechanisms only and sequentially subtract the convection losses determined with the previously estimated surface temperatures without further iteration to determine updated surface temperatures. Note that multiple iteration steps are easily possible with the analytical model used for this comparison, but the intention is to show that the possibly more accurate experimental Clausing from 1987 or the Siebers & Kraabel model could be applied confidently without worrying about the relatively small effect of the heat lost to the ambient due to convection on the different surface temperatures. As mentioned earlier, the correlations presented by Clausing in 1987 as well as the Siebers & Kraabel correlation only provide one heat transfer coefficient to determine the totally convected heat to the surroundings assuming isothermal surfaces.

In addition to the reported simulations with the completed receiver model, Figure 2.4 and 2.5 compare the Nusselt number correlations over a range of Rayleigh numbers. The graphs also include two correlations for vertical, flat plates. Siebers (1983) conducted measurements for natural convection heat losses from large, vertical surfaces and reported the following correlation:

$$Nu = 0.098\, Gr^{\frac{1}{3}} \left(\frac{T_w}{T_\infty}\right)^{-0.14} \tag{2.22}$$

The properties in the dimensionless numbers are evaluated at ambient temperature and the characteristic length is the plate height. Nellis and Klein's (2009) heat transfer textbook provided an additional correlation for the turbulent region:

$$Nu = \frac{0.13 Pr^{0.22}}{(1 + 0.61 Pr^{0.81})^{0.42}} \frac{Ra^{\frac{1}{3}}}{1 + (1.4 \times 10^9)\frac{Pr}{Ra}} \tag{2.23}$$

for a range of $Ra < 10^{12}$. The properties must be evaluated at the film temperature.

Figure 2.4 shows the Nusselt number as a function of the Rayleigh number for a cubical cavity with isothermal surfaces at $T_w = 700\, K$ and an ambient temperature of $T_\infty = 300\, K$. The aperture covers one entire side wall of the cube. In contrast, Figure 2.5 shows the correlations assuming that an upper lip with a height of $0.25 \times$ cube height is attached to the ceiling above the aperture. The area definition is the total interior surface area including the area of the stagnant zone the second case where an upper lip was included.

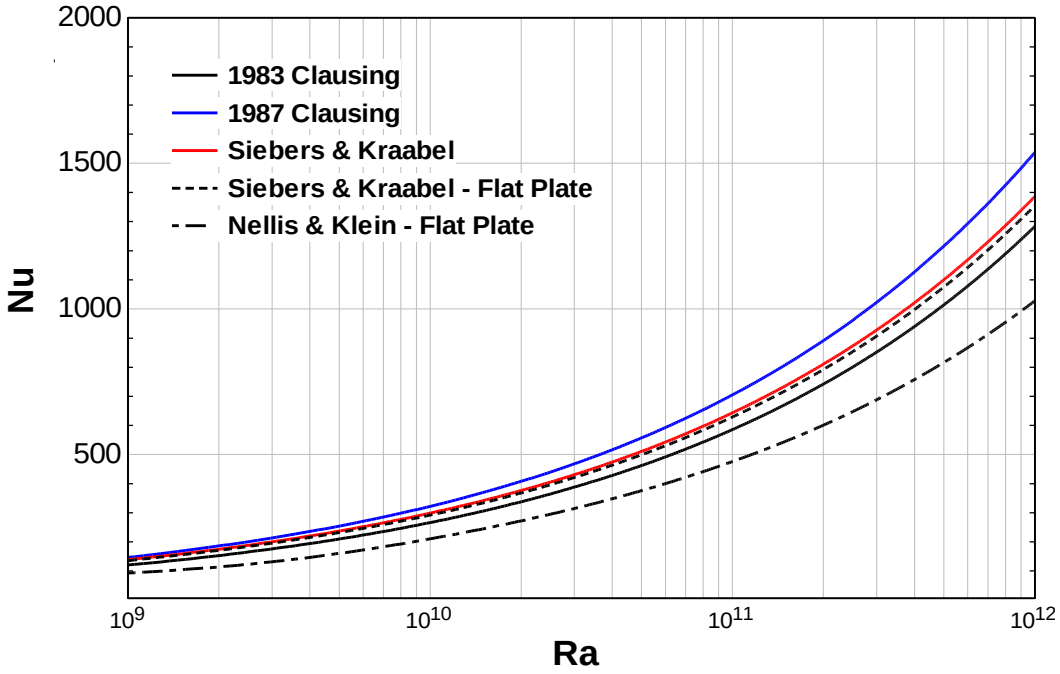

Figure 2.4: Correlations for natural convection from an isothermal, side-facing cubical cavity where the aperture covers one entire side wall also including flat-plate correlations.

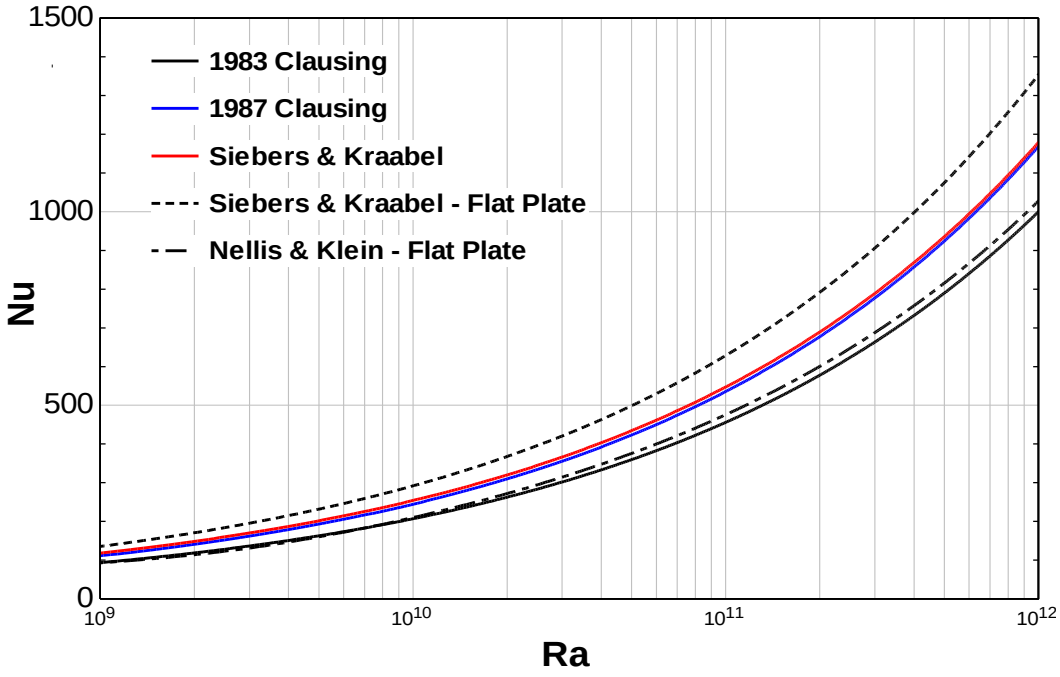

Figure 2.5: Same as Figure 2.4 except an upper lip attached to the cavity opening such that the aperture area is 0.75 x (cube height x cube width).

The characteristic length in the dimensionless numbers of Fig. 2.4 and 2.5 is the aperture height. All the properties were evaluated at the film temperature, $T_{film} = 500\,K$. The averaged heat transfer coefficients in the Nusselt numbers were calculated with the convective heat loss rate resulting from the model definitions divided by the product of total interior surface area that includes the surface area in the stagnant zone and the temperature difference:

$$h = \frac{\dot{q}}{A_{total}(T_w - T_\infty)} \tag{2.24}$$

For the flat plate correlations, the receiver plate surface was assumed to have a height of cavity aperture and width such that the total surface area is identical to the interior surface area of the cubical cavity.

It seems contrary to conventional understanding that the free convection heat losses in Fig. 2.4 from a side-facing cubical cavity are higher than those from a vertical plate with the same height and surface area. However, this phenomenon is consistent with findings from Siebers (1983) and Kraabel's (1983) experiments on vertical flat plates and cubical cavities, respectively. In Figure 2.6, the experimentally-determined heat transfer coefficients for natural convection from cavities and flat plates is plotted over the Grashof number to the third power multiplied by the conductivity of air and divided by the characteristic length: $Gr^{1/3}k/L$. The properties are evaluated at ambient temperature.

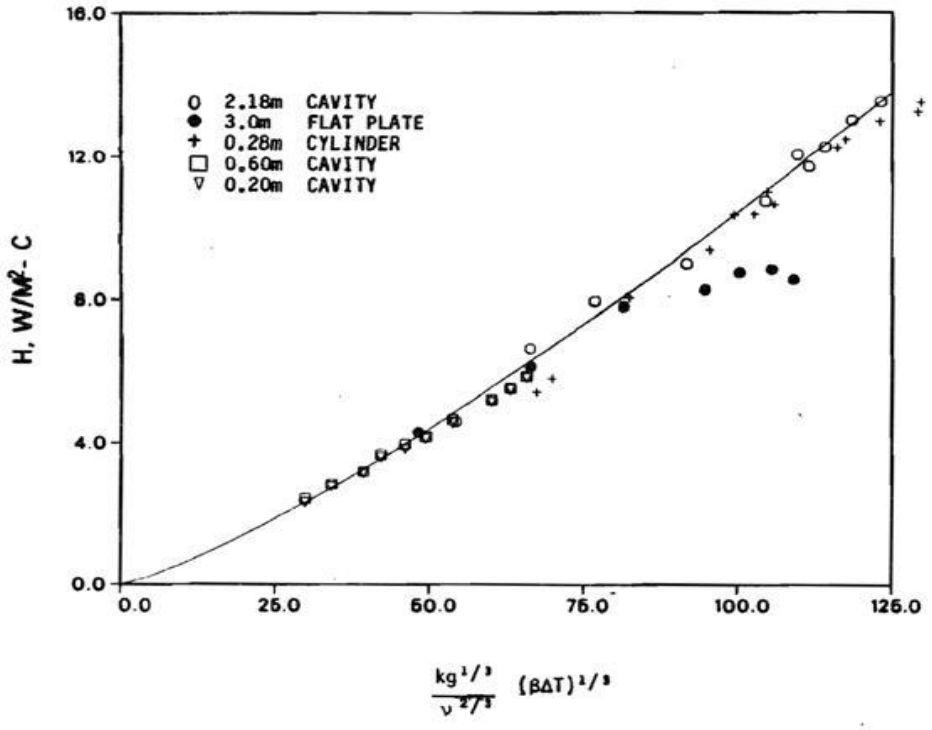

Figure 2.6: Turbulent convection heat transfer coefficient versus the modified Grashof number (Siebers and Kraabel, 1984).

The presented experimental results indicate higher averaged heat transfer coefficients than for vertical flat plates. The introduction of a lip mounted above the aperture results in a reduction of the convection losses from the cavity. It is assumed that the heated air rises to the top of the receiver and gets trapped in the zone above the upper lip. Figure 2.7 shows how the lip size reduces the natural convection losses from the cavities.

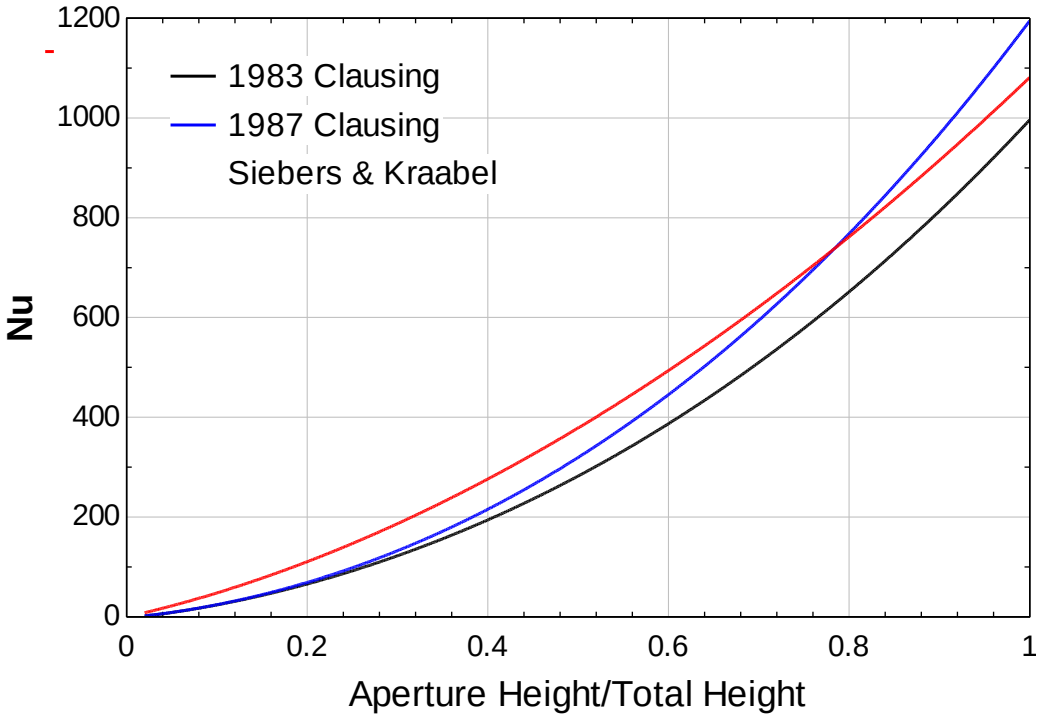

Figure 2.7: Correlations for natural convection heat loss from an isothermal, side-facing cubical cavity with a side length of 5m and varying upper lip size (lip is 5m wide).

Figure 2.7 indicate that the Siebers & Kraabel and the newer Clausing correlations intersect at an aperture height of approximately 0.78 of the total cavity height. This observation is consistent with the good agreement of the Siebers & Kraabel correlation with the updated Clausing model in Figure 2.5 where the aperture height to total height ratio is 0.75. Note that the agreement between the two models is also due to the particular surface temperature conditions. Figures 2.8 and 2.9 show the Nusselt numbers as a function of the averaged wall temperature normalized by the ambient temperature. The results were obtained for cubical cavities with a side length of 5m.

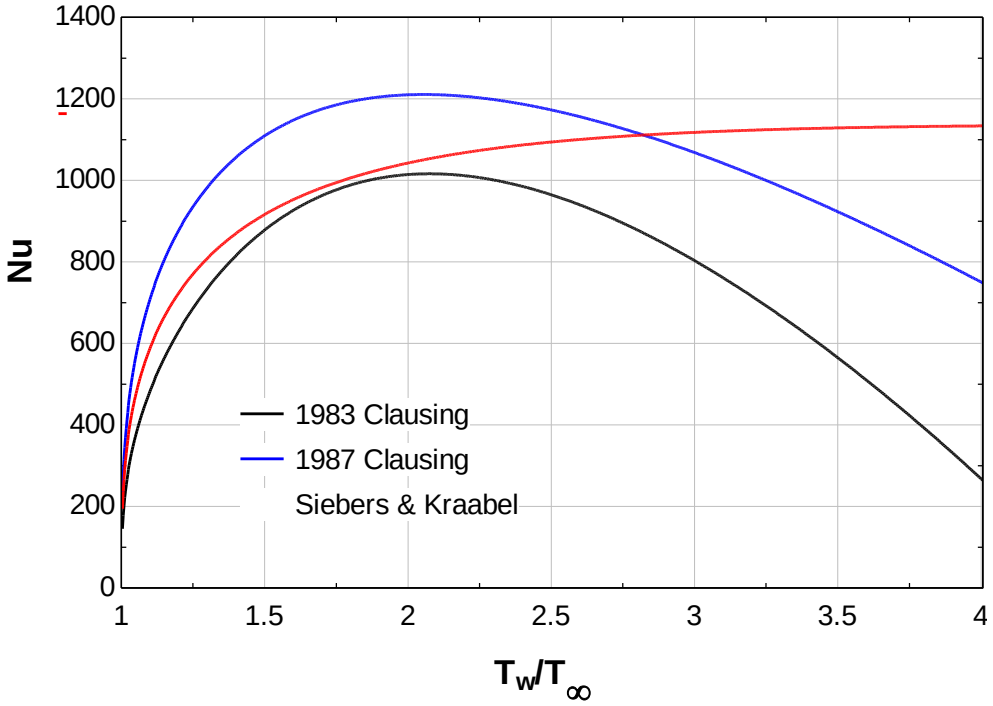

Figure 2.8: Natural convection from an isothermal, side-facing cubical cavity where the aperture covers one entire side wall as a function of wall to ambient temperature ratio.

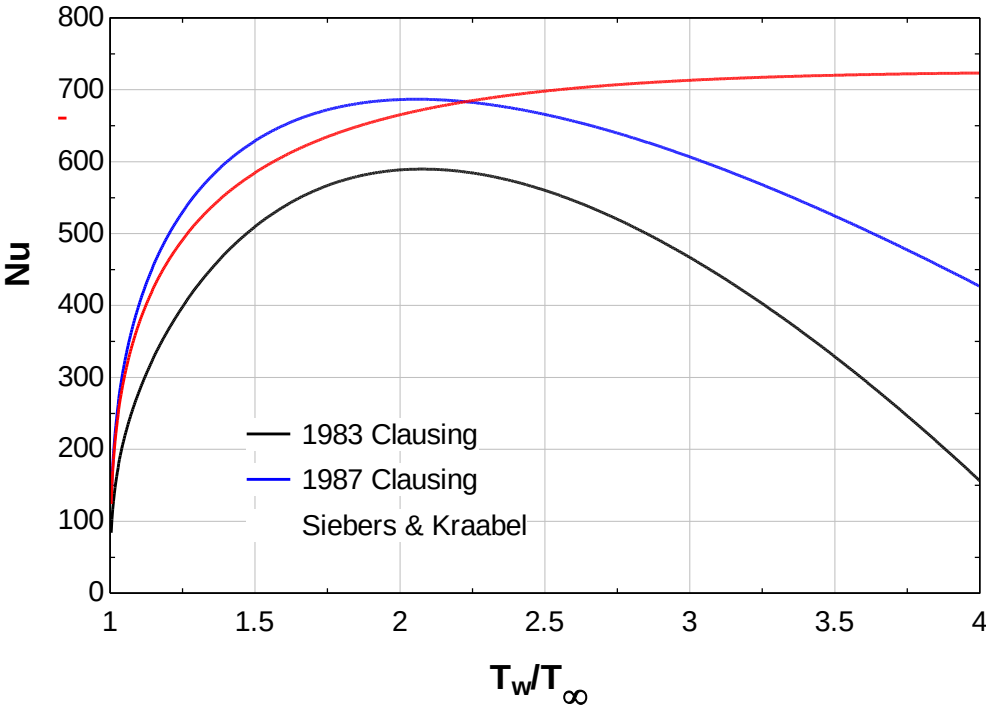

Figure 2.9: Same as Figure 2.8 except an upper lip attached to the cavity opening such that the aperture area is 0.75 x (cube height x cube width).

2.2.4 Conclusions

The results lead to the assumption that either the updated Clausing convection loss model (1987) or the Siebers & Kraabel correlation (1984) is the most accurate choice of the available correlations. Both correlations were developed with data from experiments on cubical receivers. The experiments were conducted at conditions that are comparable to the range of Rayleigh and Prandtl numbers for the large central receivers. The models also account for the large difference between the wall and ambient temperatures. For example, Clausing's experiments were conducted over a range from $1 < T_w/T_\infty < 3$. The cavity receiver for the demonstrated case operates under a maximal T_w/T_∞ ratio of approximately 2.8. Clausing conducted experiments on cavities with a number of different aperture geometries to include the effect of the aperture shape and size on the heat losses. Both correlations are independent of the receiver size in the turbulent region. At such high Rayleigh numbers, the length scale cancels out of the dimensionless numbers because the correlations are a function of the Rayleigh number to the third power. Kraabel (1983) also states that his correlation shows good agreement with data from measurements on different cavity sizes. Furthermore, both authors claim that their correlation is applicable to a variety of cavity geometries.

⇗3 Radiation Heat Transfer

Thermal energy transferred to the working fluid by the receiver panels which are heated by absorbing incident solar radiation. The solar radiation incident on the cavity receiver panels is the beam solar component reflected by a field of reflective heliostat surfaces which focus the beam radiation onto the receiver surface. In addition, there is long-wave radiative exchange within the cavity receiver itself due to the high temperature of surfaces that are either active (having heat transfer fluid) or non-active surfaces (structural only). Lastly, the high temperature surfaces within the cavity will exchange long-wave radiation to the ambient environment through the aperture opening. This radiative transfer mechanism results in an energy loss from the receiver.

The following section explains the methods used for determining the distribution of the solar flux on the panel surfaces. Section 3.2 and its subsections cover the internal radiation exchange between cavity surfaces and the ambient.

3.1 Incident Solar Radiation

During this research, the short-wave radiative flux on the receiver surfaces from heliostat field was modeled with DELSOL3, a Fortran computer code written by researchers at Sandia National Laboratories in the 1980's. Utilizing a radially staggered method, the software is able to calculate an optimized heliostat field layouts for a given receiver design (Kistler, 1986). Although DELSOL3 is capable of calculating overall performance of solar thermal central receiver power plant, the assumptions for the thermal losses from a cavity receiver are overly simplified. The losses are assumed to be independent of time and the only scaling factors are the aperture size and the cavity area. Constant values were assumed for the remaining factors that influence the thermal losses which include: an average wall temperature ($T_w = 753\ K$), the ambient temperature ($T_\infty = 293.15\ K$), receiver surface emissivity of ($\varepsilon = 0.9$) and an average ambient wind speed ($u_\infty = 7.2\ m/s$).

The present receiver model makes use of two main capabilities of the DELSOL3 code. That is the calculation of an overall efficiency of the heliostat field and the solar flux distribution on the active receiver surfaces. The radiation hitting the heliostats is reduced by a number of factors before it arrives on the receiver panels. The losses are caused by the following factors.

- *Cosine attenuation*: If the heliostat surface is not orthogonal to the incident radiation, the effective reflecting area is smaller than the complete heliostat surface
- *Shading and blocking effects*: Surrounding heliostats shield parts of the incoming radiation or block the reflected radiation.
- *Atmospheric scatter*: Particles in the air absorb or reflect part of the radiation on its way to the receiver.
- *Reflection losses from the receiver*: The receiver absorptivity is dependent on the coating material and the incident radiation angle. Angles different than perpendicular increase the reflected fraction of the incident radiation.
- Spillage: A fraction (called the spillage) of the reflected heliostat image does not the target surface due to multiple sources (tracking inaccuracies, sway of the tower, shape of the sun, etc.)
- Tracking Errors: Deviations from positioning individual heliostats to reflect incident radiation onto the receiver surfaces
- Other: Lack of maintenance on the heliostats in the field including accumulation of debris on reflective surfaces or other surface defects.

Detailed descriptions of the radiation losses in the field are provided by Wagner (2008) and Stine and Geyer (2001). Stone and Jones (1999) explain issues with the controlling and field tracking algorithms. The equations used in DELSOL3 for the loss calculations are explained

by Kistler (1986). The overall heliostat field efficiency utilized by the cavity receiver model is defined as the incident radiative power on the receiver, which is the product of the average solar flux $\dot{q}''_{inc}$ and the active receiver surface A_{rec}, divided by the total radiation on the heliostat field $\dot{q}_{helio,total}$.

$$\eta_{field} = \frac{\dot{q}_{helio,total} - \dot{q}_{loss,field}}{\dot{q}_{helio,total}} = \frac{\dot{q}''_{inc}\, A_{rec}}{I_{bn} A_{helio} N_{helio}} \tag{3.1}$$

The radiation power on the heliostat field is the product of the direct beam normal radiation I_{bn} and the total heliostat surface area, i.e. the product of the effective surface area of one heliostat A_{helio} and the number of heliostats in the field N_{helio}. the term $\dot{q}_{loss,field}$ represents the accumulated losses described above. In the cavity receiver model, Equation (2.2) is solved for the incident solar radiation on the receiver surfaces, where the field efficiency is provided by PTGen, a program developed by Wagner (2008) that facilitates the use of the DELSOL3 code.

Ideally, the incoming radiative flux is spread uniformly on the active receiver surface to maximize the opportunity to absorb the incident radiation without exceeding the material flux limits. In reality, the solar flux is distributed in patterns that show maximum flux rates on the surface center to reduce spillage losses. DELSOL provides options for a single-point aiming technique (where the complete flux is focused on a central point of the receiver panels) a smart aiming technique (where the flux is vertically and horizontally spread out along the absorbing surface), and other aiming strategies.

Figures 3.1 and 3.2 show examples of DELSOL3-generated flux distributions on the receiver surface utilizing the single-point and smart aiming techniques, respectively. Note that the receiver panels have been “unwrapped” and laid out flat to the complete plot area. Using default settings, cavity receiver flux maps generated with DELSOL3 have 120 flux points, 10 in the vertical direction and 12 in the horizontal direction.

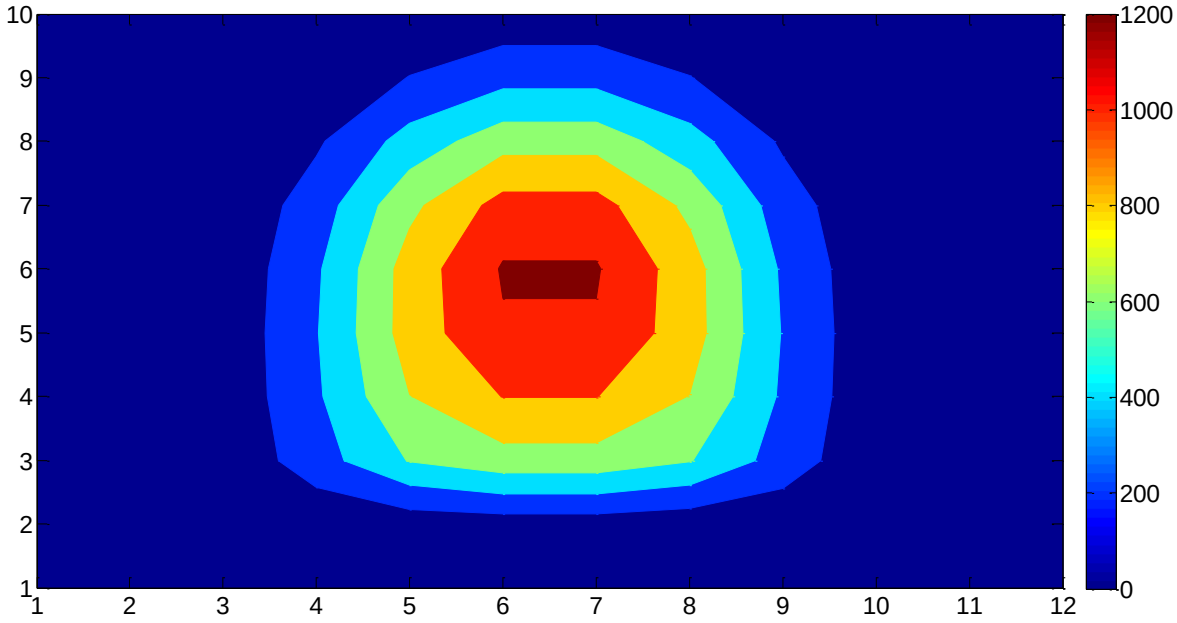

Figure 3.1: Flux distribution, generated with the single-point aiming technique, in kW/m^2 on the active receiver surface at noon when the solar azimuth and zenith angle is -10° (sun is south at 0°) and 33°, respectively. The plant is located in Daggett, CA.

For both cases shown in Figures 3.1 and 3.2, the total radiation power hitting the receiver is 58 MW. While stainless surfaces (stainless steel 316) have a technical flux limitation of around 850 kW/m^2 (at the Solar Two external receiver (Wagner, 2008)), the distribution in Figure 3.1 shows flux peaks of at 1200 kW/m^2, which would cause local hot spots and destroy most receiver panels. Figure 3.2 shows that with a more uniform pattern, the radiation intensity peaks can be reduced by a factor 2 in this case.

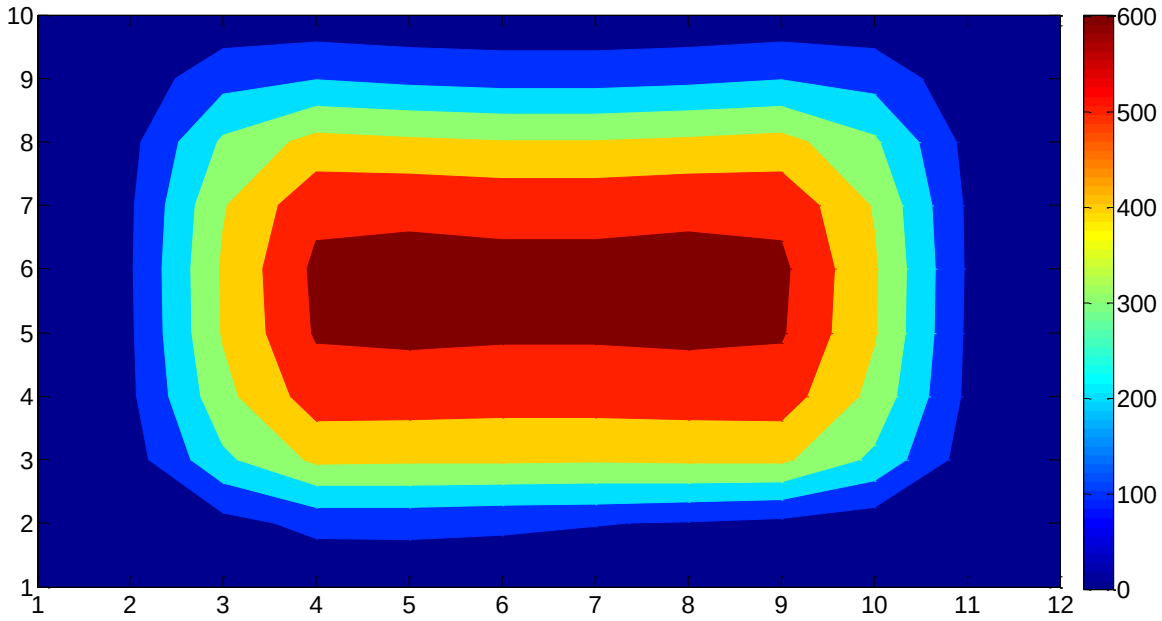

Figure 3.2: Flux distribution in kW/m^2 on the active receiver surface, when the solar azimuth and zenith angle is -10° (sun is south at 0°) and 33°, respectively. The plant is located in Daggett, CA and the distribution is generated with the smart aiming technique.

3.2 Radiation Heat Exchange Inside the Cavity

Depending on the reflectivity of the material and the incidence angle of the incoming radiation, a small portion of the incident radiation on the panels is directly reflected to the surrounding panels, inactive surfaces and out of the aperture back to the ambient. The major portion of the radiation is absorbed by the active panel surfaces that are cooled with the working fluid. Due to the radiation absorptivity and emissivity of the coating material of above 90%, the surfaces are assumed to be black for the radiation calculations in the present receiver model. That means, the influences of reflected radiation are not considered and assumed to be small in this analysis. However, part of the absorbed radiation from the active panels will be re-emitted to the surroundings. The remaining energy will be conducted to the fluid in the heat exchanger tubes. Assuming black body radiation mechanisms only, the radiation exchange between surfaces at different temperatures relies purely on the geometry

and the surface temperature. The net thermal radiation rate from each surface i to all surfaces $j = 1..N$ is given by Equation (2.4). In this case, the interior cavity area including the aperture surface is divided into N different surfaces, each is assumed to be at a uniform temperature. Each surface is assumed to emit thermal radiation diffusely, i.e., with no preferred direction.

$$\dot{q}_{rad,net,i} = \sigma A_i \sum_{j=1}^{N} F_{i-j}(T_i^4 - T_j^4) \tag{3.2}$$

where σ is the Stefan-Boltzmann ($\sigma = 5.67 \times 10^{-8} \frac{W}{m^2 K^4}$); A_i is the surface area of the emitting body; T_i and T_j are the temperatures of the exchanging surfaces; and F_{i-j} is a dimensionless ratio (view factor) that quantifies how much diffuse radiation emitted from surface i hits surface j. The view factors for radiation exchange between discrete surfaces will range between 0 and 1. The view factor between surface i to j, F_{i-j}, will be zero when neither surface can "see" each other. In this case, no radiation heat transfer will occur between surface i and surface j. The view factor between surface *i* and *j* will be unity when all of the emitted radiation from surface i arriving at surface j. Equation (2.2), describes the net radiation exchange rate and is included in the total energy balance for each surface i, as further explained in Chapter 5. The radiation heat losses from the receiver are explicitly determined by formulating an energy balance around the aperture surface.

3.2.1 Geometric Cavity Model for the View Factor Calculations

In order to calculate view factors F_{i-j}, the receiver must have a defined geometric design. The design of the receiver on the PS10 Solar Tower in Spain was considered to be a useful prototype of a model receiver. The core of the receiver contains four rectangular panels that absorb the concentrated radiation from the heliostat field. Each panel is formed by a set of

cooling fluid tubes, which are made of materials that can resist the high operating temperatures and provide good absorption characteristics for solar radiation. The 12 m high panels approximate a vertical semi-cylinder with a radius of 7 m (Solúcar, 2006). The tower construction with parts of the receiver can be seen in Figure 3.4.

Figure 3.3: Three of four receiver panels are assembled on the PS10 tower (Solúcar, 2006)

With the provided data, a model receiver (Figure 3.5) was created that resembles the approximate shape of the PS10 receiver using a four-node approximation of a semi-cylindrical absorbing surface (i.e. four rectangular panels that are aligned on a semi-circle). In attempts to minimize convective and long-wave radiative losses from the cavity, the open area of the aperture is reduced by including an "lip" that extends from the cavity ceiling downward. The full front face area is defined by the panel height H_P and the aperture width W_A. The sum of the aperture height H_A and the lip height H_L equal the panel or internal height as shown in Figure 3.5.

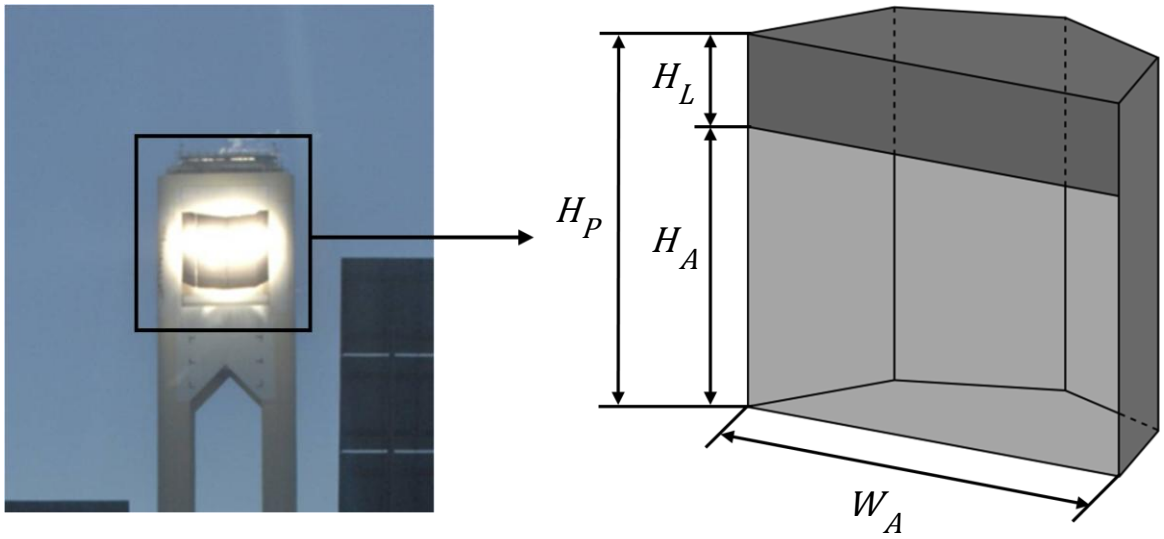

Figure 3.4: Approximation of the PS10 cavity receiver geometry

3.2.1.1 Surface Discretization

Due to the gradients in the solar flux distribution across the receiver panels and the flow distribution of the cooling fluid in the panel pipes, the receiver surfaces will not be at uniform temperature. To simplify the complex radiation heat transfer problem, the active receiver surfaces were subdivided into discrete nodes assumed to operate at a uniform temperature as an approximation of the panel temperature distribution. In the first step, each receiver surface was split into four vertical nodes as shown in Figure 3.6(b). Later, the view factor calculation program was generalized to handle any number of nodes in the vertical direction as shown in Figure 3.6(c). Each node has the height

$$H_{node} = \frac{H_P}{N_{nodes}}, \tag{3.3}$$

where H_P is the complete panel height and N_{nodes} the number of vertical nodes per panel.

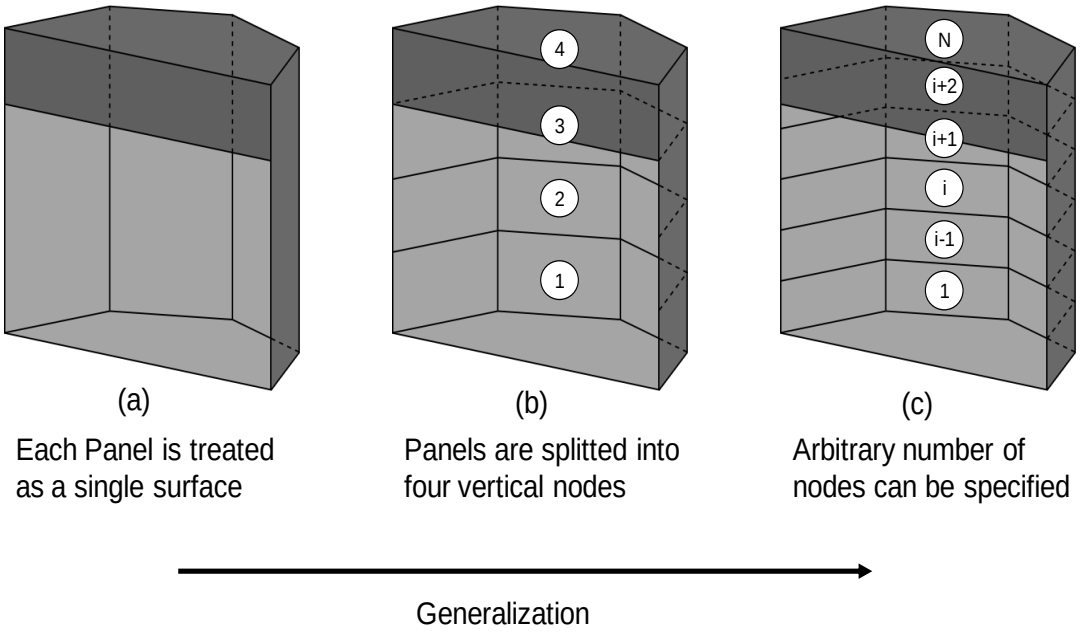

Figure 3.5: Refinement steps of the panel subdivision.

One rationale for the vertical break-up arrangement is due to the assumed flow pattern of the cooling fluid. The fluid tubes are lined up horizontally along the panel width, but they curl up from the bottom to the top so the main temperature gradient will be in the vertical direction. The horizontal temperature gradients across the panel width are assumed to be small compared to the vertical temperature change. The discretization of panels is also needed to accomplish an accurate distribution of the incoming solar flux from the heliostats. The combination of flux distribution and the fluid circuiting results in segments of the panel surfaces that will operate at different temperatures.

3.2.1.2 Receiver Dimensions

In order to provide some degree of flexibility, the dimensions of the model receiver can be adjusted with geometric parameters that are set as free variables in the view factor calculations. Figure 3.7 shows a plan view on the basic cavity receiver panel setup, where the panel nodes 1-4 are shown from left to right. The edges of the four absorbing rectangular

receiver panels are aligned on a section of a circle with the radius R_{rec}. The extent of the receiver section is determined by the angle θ_{rec}.

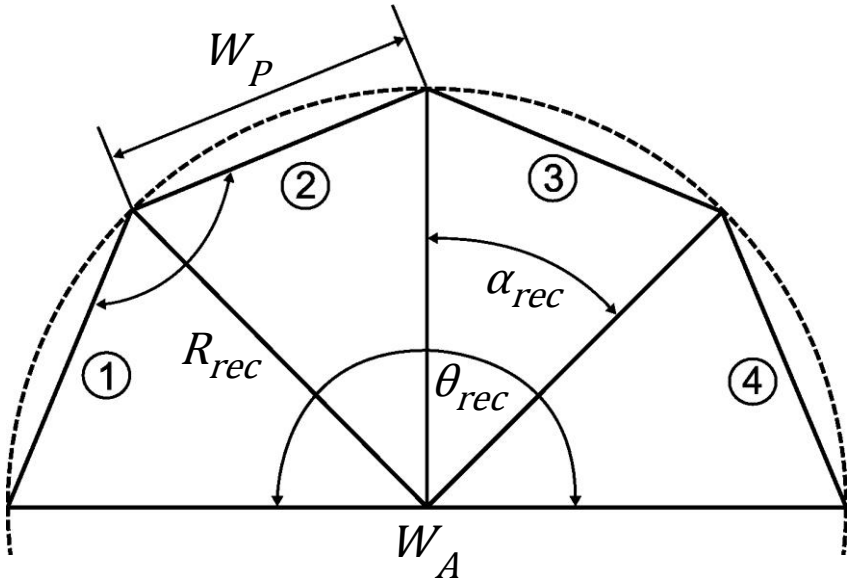

Figure 3.6: Top view on the panel setup and the basic geometric relationships

Assuming the four receiver panels have equal widths and their edges are adjacent with the neighbor panels, each panel has the width, W_P. The radius, R_{rec}, angle, θ_{rec}, and panel height, H_P, are free parameters in the model. Given these parameters, all other important quantities can be determined with basic geometric relationships:

$$\alpha_{rec} = \theta_{rec}/4 \tag{3.4}$$

$$W_P = 2R_{rec}\sin(\alpha_{rec}/2) \tag{3.5}$$

$$W_A = 2R_{rec}\sin(\pi - 2\alpha_{rec}) \tag{3.6}$$

The length W_A is the aperture width if the aperture is considered to be the opening of the semi-cylinder formed by the panels.

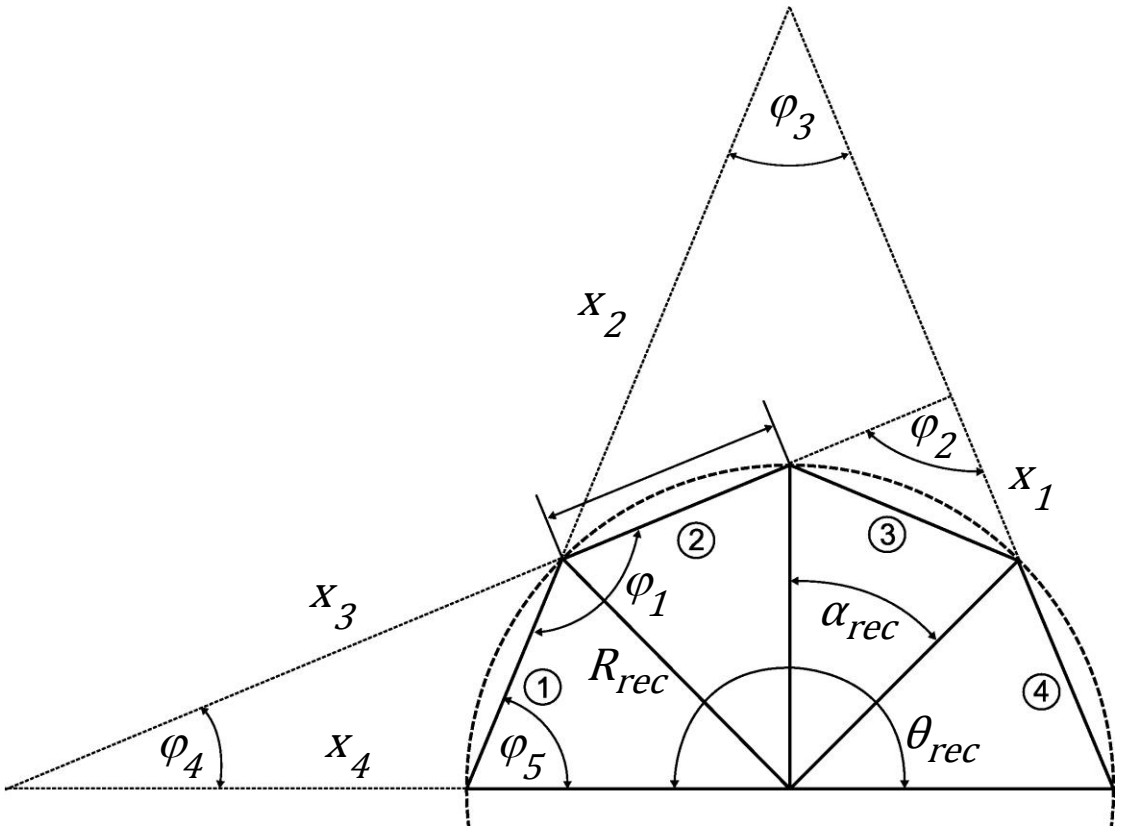

Figure 3.7: Angles between receiver panels and aperture

Further relations between the dimensions are necessary to completely describe the receiver geometry. φ_1 is the angle between two adjacent panels shown in Figure 3.8. The angle between panels framing one panel is φ_2, and the angle between the outer panels is defined as φ_3. For the calculation of the view factors between the inner panels and the aperture and the outer panels and the aperture, angles φ_4 and φ_5, respectively, need to be defined as well.

$$\varphi_1 = \pi - \alpha_{rec} \tag{3.7}$$

$$\varphi_2 = \pi - 2\alpha_{rec} \tag{3.8}$$

$$\varphi_3 = \pi - 3\alpha_{rec} \tag{3.9}$$

$$\varphi_4 = 3\alpha_{rec}/2 \tag{3.10}$$

$$\varphi_5 = \alpha_{rec}/2 \tag{3.11}$$

The lengths x with the indices 1 through 4 appearing in Figure 3.8 are obtained with

$$x_1 = R_{rec}\frac{\sin(\alpha_{rec}/2)}{\cos(\alpha_{rec})} \tag{3.12}$$

$$x_2 = R_{rec}\frac{\sin(\alpha_{rec})}{\sin\left(\frac{\pi - 3\alpha_{rec}}{2}\right)} \tag{3.13}$$

$$x_3 = R_{rec}\left(\frac{1+\cos(\pi - 2\alpha_{rec})}{\sin\left(\frac{\alpha_{rec}}{2}\right)} - 2\sin\left(\frac{\alpha_{rec}}{2}\right)\right) \tag{3.14}$$

$$x_4 = R_{rec}\left(\frac{1+\cos(\pi - 2\alpha_{rec})}{\tan\left(\frac{\alpha_{rec}}{2}\right)} - \sin(\pi - 2\alpha_{rec})\right) \tag{3.15}$$

3.2.2 View Factor Calculations

A general relationship for the calculation of the view factor from surface i to j (Figure 3.3) is given by (Nellis & Klein, 2009):

$$A_i F_{i-j} = A_j F_{j-i} = \int_{A_j}\int_{A_i} \frac{\cos\theta_i \cos\theta_j}{\pi r^2} dA_i dA_j \tag{3.16}$$

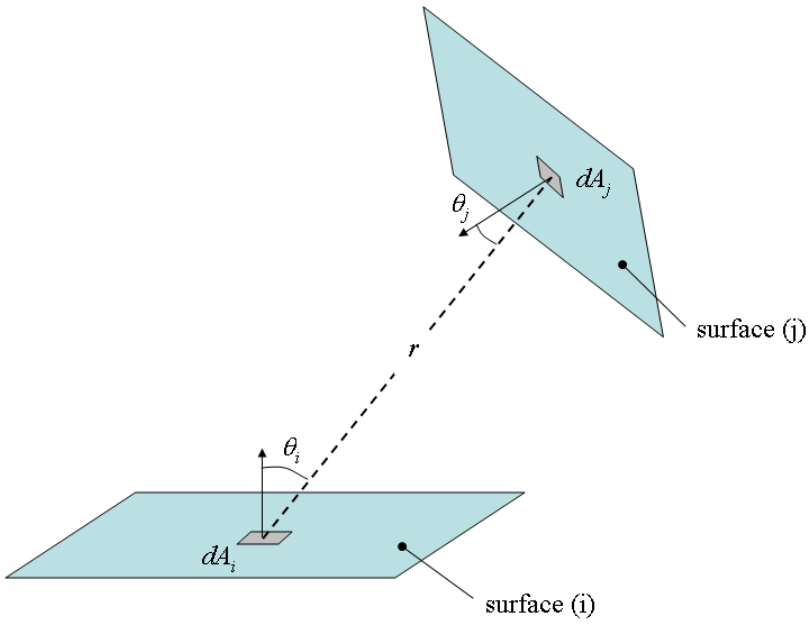

Figure 3.8: Radiation exchange between two arbitrarily positioned surfaces (Nellis & Klein, 2009)

Siegel and Howell (2001) have gathered a large collection of two-dimensional and three-dimensional view factor relationships for many different geometries. However, not every factor that is needed for a complete description of the cavity receiver can be determined with these existing relations.

A few simple rules helped to determine some of the missing view factors. Reciprocity, for example, is described by the generally applicable equation:

$$F_{i-j}A_i = F_{j-i}A_j \tag{3.17}$$

Furthermore, the combination of two surfaces can be expressed as:

$$F_{i-jk} = F_{i-j} + F_{i-k} \tag{3.18}$$

The enclosure rule is used for computation of the last missing view factor, because in an enclosure the sum of all the view factors for radiation from surface i equals 1.

$$\sum_{j=1}^{N} F_{i-j} = 1 \tag{3.19}$$

Equation (2.5) with other assumptions was also used to validate the results of the implemented functions.

A numerical Monte-Carlo ray tracing method was implemented to calculate the view factors for radiation exchange with the complex shaped top and bottom surfaces where no analytical relationships were found in the literature.

3.2.2.1 Analytical View Factor Relationships

All geometric relationships needed to compute the view factors between the vertical surfaces in the receiver are provided through Equations (3.3)-(3.15). Gross, Spindler, & Hahne (1981) developed an analytical relation to calculate the view factors between plane rectangular surfaces of arbitrary position and size with parallel boundaries as shown in Figure 3.9.

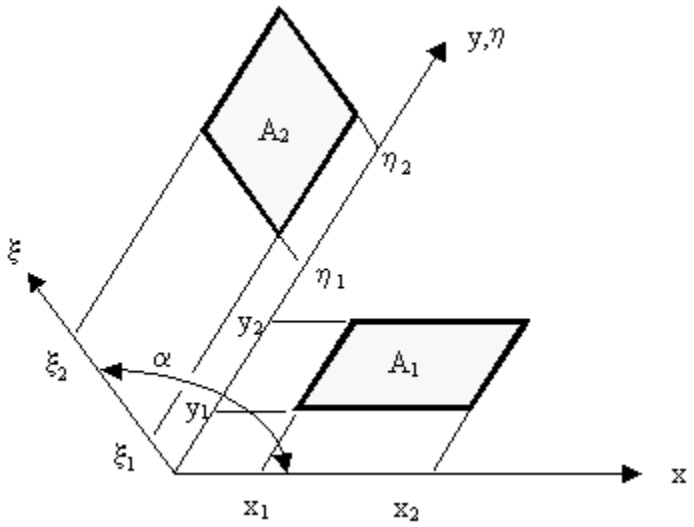

Figure 3.9: View factor between inclined rectangles 1 and 2. All rectangle edges are parallel or perpendicular to the intersection line of the rectangle planes (Siegel & Howell, 2001).

The values of $\eta_1, \eta_2, y_1, y_2, \xi_1, \xi_2,\ x_1,\ x_2,$ and α are determined with the set of earlier derived lengths and angles.

$$F_{1-2} = \frac{1}{A_1}\sum_{k=1}^{2}\sum_{j=1}^{2}\sum_{i=1}^{2}[(-1)^{(i+j+k)}\ G(x_i, y_j, \eta_k)] \tag{3.20}$$

with

$$G(x, y, \eta) = -\frac{(\eta - y)\sin^2\alpha}{2\pi}\int_{\xi} f(x, y, \eta, \xi)\ d\xi \tag{3.21}$$

where

$$\begin{aligned} & f(x, y, \eta, \xi) \\ & = \frac{(x - \xi\cos\alpha)\cos\alpha - \xi\sin^2\alpha}{(x^2 - 2x\xi\cos\alpha + \xi^2)^{\frac{1}{2}}\sin^2\alpha}\tan^{-1}\left(\frac{(\eta - y)}{(x^2 - 2x\xi\cos\alpha + \xi^2)^{\frac{1}{2}}}\right) \\ & + \frac{\cos\alpha}{(\eta - y)\sin^2\alpha}\left\{[\xi^2\sin^2\alpha + (\eta - y)^2]^{\frac{1}{2}}\tan^{-1}\left(\frac{x - \xi\cos\alpha}{[\xi^2\sin^2\alpha + (\eta - y)^2]^{\frac{1}{2}}}\right)\right. \\ & \qquad \left. - \xi\sin\alpha\tan^{-1}\left(\frac{x - \xi\cos\alpha}{\sin\alpha}\right)\right\} \\ & \qquad + \frac{\xi}{2(\eta - y)}\ln\left(\frac{x^2 - 2x\xi\cos\alpha + \xi^2 + (\eta - y)^2}{x^2 - 2x\xi\cos\alpha + \xi^2}\right) \end{aligned} \tag{3.22}$$

For each view factor calculation, the function G in Equation (3.20) is evaluated 8 times with Equations (3.21) and (3.22), where the integral in Equation (3.21) is solved numerically.

Note that numerical integration of Equation (2.9) was not possible for the cases where

$$\eta - y = 0 \tag{3.23}$$

or

$$x_1 = \xi_1 = 0. \tag{3.24}$$

Hence if the input geometry is set for either of these conditions, adjustments to the geometry are made so that the zero is replaced with small values. A few tests showed that values of $1e-6[m]$ are sufficiently small such that changes in the results for the view factors were recognized only in the sixth or seventh decimal place.

A procedure to calculate the view factors between all panel surface nodes and the lip and aperture surfaces was written in the Engineering Equation Solver (Klein, 2008). A listing of the EES program is provided in Appendix A.

3.2.2.2 Monte-Carlo Ray Tracing

Because the literature did not provide suitable relationships to compute the view factors between the vertical surfaces and the bottom or ceiling surface due to their odd shapes, a Monte-Carlo ray tracing technique was applied and coded into Fortran to nu numerically obtain the remaining view factors. The function for each required view factor simulates radiation as a diffuse source-emitting surface. In the analysis, a large number of rays leave the radiating surface in randomly generated directions and the path of each ray is tracked to determine whether it hits the target surface. The view factor is then simply the ratio of the number of rays that hit the target to the totally generated number. The accuracy of the Monte-Carlo depends strongly on the number of generated rays and, in order to generate reliable results, the computational effort can become significant.

At first, a convenient coordinate system has to be identified. All the necessary view factors are for the radiation from rectangles (panel nodes, lip surface and aperture) to the more complicated bottom and top surface shapes. It was convenient to choose the coordinate system such that the rectangle was in the z =0 plane as shown in Figure 3.10.

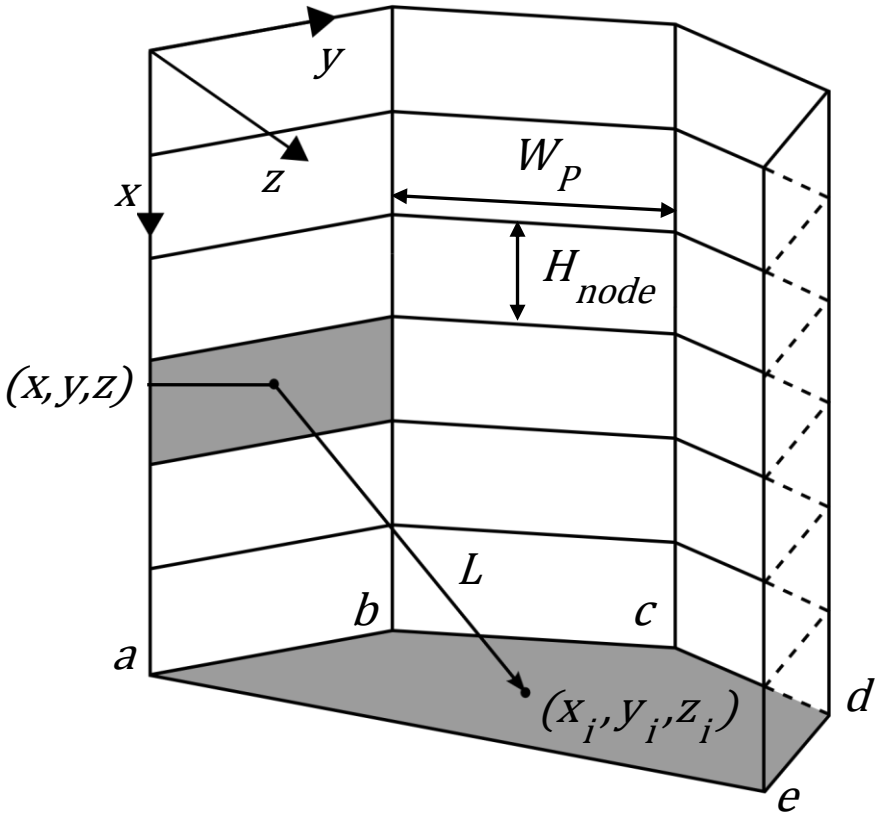

Figure 3.10: Coordinate system for ray tracing from a panel node to the bottom surface

The coordinates of a randomly generated ray origin on the radiating surface are:

$$x = (i-1)H_{node} + RN \cdot H_{node} \tag{3.25}$$

$$y = RN \cdot W_P \tag{3.26}$$

The z-coordinate is 0 for all ray origins by definition of the Cartesian coordinate system. RN in Equations (3.25) and (3.26) is a randomly generated number between 0 and 1. The integer i identifies the panel number in the vertical direction counting from the top to the bottom and it ranges from $i = 1..N_{nodes}$. Thus, the computer code sequentially calculates the view factors for radiation between each receiver panel subsurface and the floor and ceiling surface, respectively, from the top to the bottom.

The ray direction is calculated with a probability distribution (Nellis & Klein, 2009):

$$P_\theta = \sin^2 \theta \tag{3.27}$$

$$P_\Phi = \frac{\Phi}{2\pi} \tag{3.28}$$

The probabilities P_θ and P_Φ are also random numbers between 0 and 1. Polar coordinates are used to describe the ray direction with the angles θ and Φ. The possible range for a ray leaving the origin surface is $0 < \Phi < \pi/2$ and $0 < \theta < 2\pi$. Expressing the direction of a direction vector $\underline{r}$ in Cartesian coordinates requires a transformation from the polar coordinates with

$$\underline{r} = (\sin\Phi\cos\theta)\underline{i} + (\sin\Phi\cos\theta)\underline{j} + (\cos\Phi)\underline{k} \tag{3.29}$$

where $\underline{i}$, $\underline{j}$, and $\underline{k}$ are the unit vectors in the coordinate directions x, y, and z. The coordinate systems are illustrated in Figure 3.11.

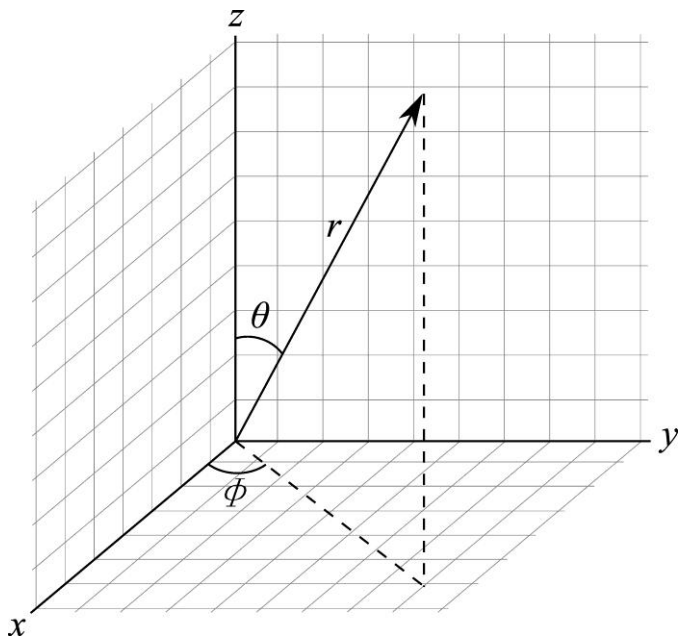

Figure 3.11: Spherical coordinate system

Accordingly, the randomly generated direction has to be tracked to determine if the ray strikes the target surface. In our case, a huge amount of rays can be excluded by checking whether $\pi/2 \leq \Phi \leq \pi 3/2$ or $\theta = 0$. In that case, the ray will never hit the surface because of the perpendicular arrangement of the surfaces to each other. Otherwise, the impact point of the ray on the target plane has to be calculated. The equation for a vector with the origin coordinates $(x, y, 0)$, a length of L and the direction of $\underline{r}$ is

$$\underline{R} = (x + L \sin\Phi \cos\theta)\underline{i} + (\mathrm{y} + \mathrm{L}\sin\Phi \cos\theta)\underline{j} + (L\cos\Phi)\underline{k} \tag{3.30}$$

The length of the vector is described by

$$L = \frac{H_P - x}{\sin\Phi \cos\theta} \tag{3.31}$$

Therefore, the impact coordinates of the ray on the plane $x = x_i = H_P$ are given as

$$y_i = y + (H_P - x)\tan\Phi \tag{3.32}$$

$$z_i = \frac{H_P - x}{\cos\Phi \tan\theta} \tag{3.33}$$

Subsequently, it has to be determined if this intersection point lies within the polygon that represents the bottom surface. The coordinates of the polygon vertices in terms of the receiver model input parameters are

$$a = \begin{bmatrix} H_P \\ 0 \\ 0 \end{bmatrix}, b = \begin{bmatrix} H_P \\ W_P \\ 0 \end{bmatrix}, c = \begin{bmatrix} H_P \\ W_P(1 + \cos(\alpha_{rec})) \\ W_P \sin(\alpha_{rec}) \end{bmatrix},$$

$$d = \begin{bmatrix} H_P \\ W_P + 2R_{rec}\sin(\alpha_{rec})\cos(\alpha_{rec} + \arccos(R_{rec}\sin(\alpha_{rec})/W_P)) \\ 2R_{rec}\sin(\alpha_{rec})\sin(\alpha_{rec} + \arccos(R_{rec}\sin(\alpha_{rec})/W_P)) \end{bmatrix},$$

$$e = \begin{bmatrix} H_P \\ W_a\cos(\alpha_{rec}) \\ W_a\sin(\alpha_{rec}3/2) \end{bmatrix}$$

A “point-in-polygon” subroutine(Point in polygon (ray casting algorithm), 2009) uses the vertices and the impact coordinates as inputs to determine whether the impact point lies within the polygon or not. In order to speed up the code, only points that lie inside of a rectangle that frames the target polygon are given to the “point-in-polygon” function. The vertices of the framing rectangle are

$$a = \begin{bmatrix} H_P \\ 0 \\ 0 \end{bmatrix}, b = \begin{bmatrix} H_P \\ W_P(1+\cos(\alpha_{rec})) \\ 0 \end{bmatrix}, c = \begin{bmatrix} H_P \\ W_P(1+\cos(\alpha_{rec})) \\ W_a \sin(\alpha_{rec}3/2) \end{bmatrix}, d = \begin{bmatrix} H_P \\ 0 \\ W_a \sin(\alpha_{rec}3/2) \end{bmatrix}$$

Note that these vertices represent the case of a coordinate system originating in the corner of the outer panels as in Figure 3.10. For different panels and the lip or aperture surface, the coordinate system should be moved to the corresponding positions in the specific surface. This will also change some of the coordinates of the polygon and rectangle vertices.

The Fortran code containing the algorithms for the ray-tracing Monte-Carlo method is attached in Appendix B.

For demonstration and verification purposes, Figures 3.12 and 3.13 show the ray intersection points with the $x = H_P$ plane for a number of 100000 totally emitted rays from the radiating surface. The intersection points that fall within the boundaries of the polygon are marked with red crosses. The coordinate origins are in the bottom left corner of each polygon and the emitting surfaces are located on the most left edge of each polygon.

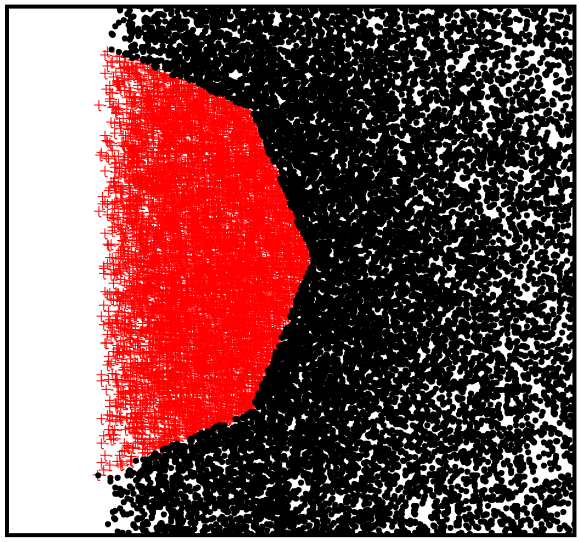

Figure 3.12: Ray impacts for the computation of the view factor from the aperture to the floor surface

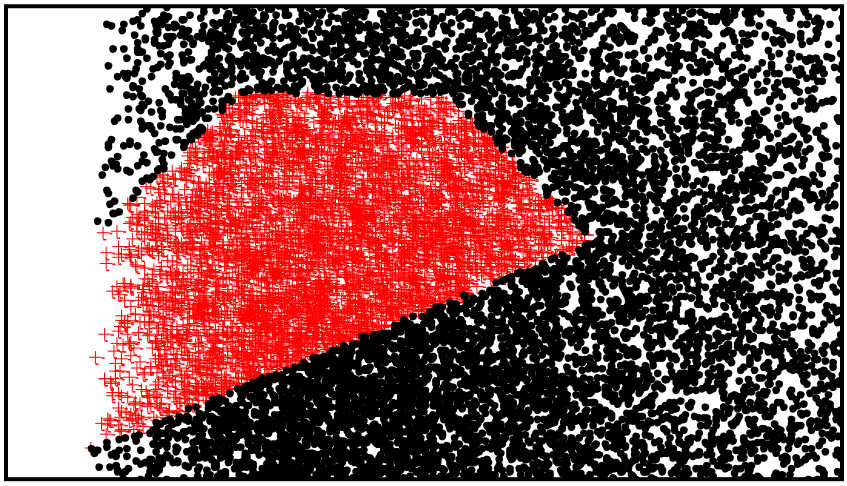

Figure 3.13: Ray impacts for the computation of the view factor from an outer panel to the floor surface

3.2.2.3 Verification of the View Factor Routines

First, the analytical routine for the view factors between the vertical surfaces in the cavity was checked at the special cases where the surfaces had an angle of 90° to each other. For the surface configurations at this angle, existing view factor functions were found in the Siegel and Howell (2001) library that are also programmed in the EES view factory library. Figure 3.14 shows the orientation of two surfaces for the three cases at angles of 90 degrees.

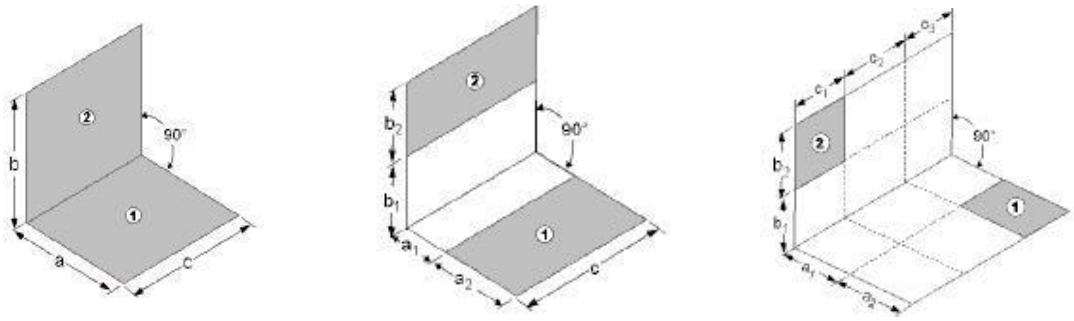

(a) **(b)** **(c)**

Figure 3.14: (a) Finite perpendicular plates with a common edge, (b) Perpendicular offset rectangles, (c) Perpendicular rectangles with no common points.

For an included angle of 90°, the implemented view factor relationship from Section 3.2.2.2 and the corresponding correlations for the special case found in the literature produced equal results.

Krishnaprakas (1997) used the view factor calculation method presented by Gross, Spindler, & Hahne (1981) and compared it to the view factor algebra method using known methods for simpler geometries and the reciprocity and summation rules. A few results of the tested cases were compared against computations with the present implementation of the described method. Two cases were used for the comparison:

Case 1: $x_1 = 1, x_2 = 2, y_1 = 1, y_2 = 2, \eta_1 = 2.5, \eta_2 = 3.5, \xi_1 = 2.5, \xi_2 = 3.5$

Case 2: $x_1 = 0, x_2 = 1, y_1 = 0, y_2 = 1, \eta_1 = 0, \eta_2 = 1, \xi_1 = 1, \xi_2 = 2$

Table 3.1 shows that the view factor function was implemented correctly; all results agree well.

Case 1			Case 2		
Angle	**Present Work**	**Krishnaprakas**	**Angle**	**Present Work**	**Krishnaprakas**
10°	0.002888	0.0028882	**10°**	0.055843	0.055843
30°	0.012919	0.0129187	**30°**	0.081072	0.0810722
45°	0.014967	0.0149665	**45°**	0.072791	0.072791
60°	0.013433	0.0134329	**60°**	0.059066	0.0590663
90°	0.00776	0.0077599	**90°**	0.032809	0.0328088

Table 3.1: View factor routine verification

Besides testing every single function at the known case at a 90 degree angle between the surface planes and the comparison in Table 3.1, the sum of the complete set (except for the top and bottom part) of view factors for radiation that is leaving one receiver surface was evaluated at a large range of panel heights (Figure 3.15). This plot indicates that the sum of the view factors approach one with at an infinitely tall cylinder as it would be for a 2D enclosure.

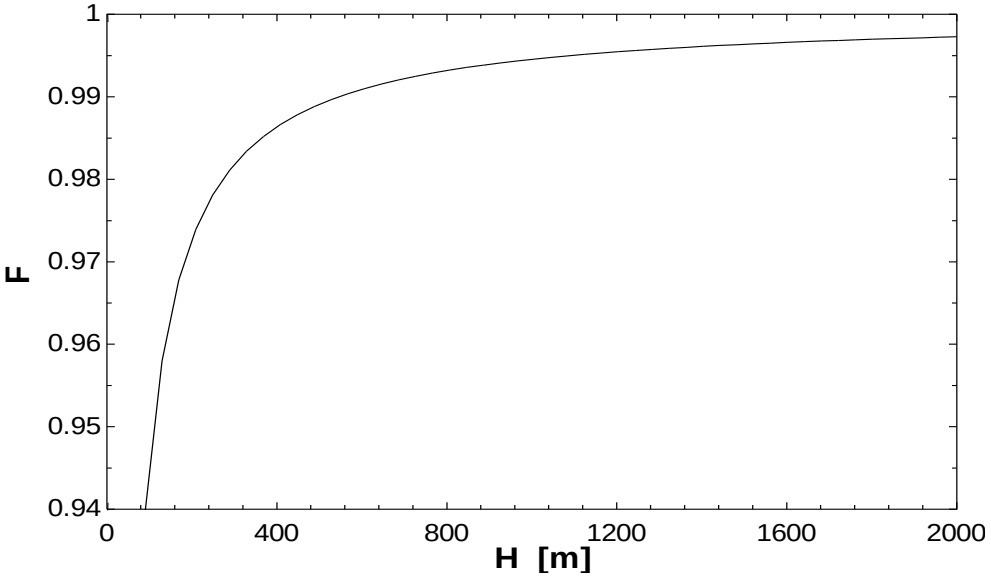

Figure 3.15: The sum F of the view factors from one panel node to the remaining nodes, the aperture and the lip is plotted as a function of the panel height.

The view factors computed with the Monte-Carlo technique complemented with the ones obtained through analytical routines were compared to values provided from Fluent simulations that were conducted by Clifford K. Ho and Siri Sahib S. Khalsa which is further discussed in Chapter 6. Table 3.2 compares samples of the view factor. The table contains the view factors between the non-active surfaces (bottom wall, top wall, lip) and the aperture as well as the factors for the radiation of the top five nodes of an outer panel (Panel: 1, Nodes: 6-10) to the inactive surfaces. Figure 3.16 illustrates the receiver configuration with the panel subdivision.

Emitting Surface		Target Surface		Fluent	Present Work
Node	Panel	Node	Panel	View Factor	
Aperture		Bottom Wall		0.0628	0.0629
Aperture		Top Wall		0.0434	0.0430
Bottom Wall		Top Wall		0.0234	0.0219
Lip		Bottom Wall		0.0021	0.0023
Lip		Top Wall		0.3900	0.3906
10	1	Aperture		0.3058	0.3064
10	1	Bottom Wall		0.0046	0.0046
10	1	Lip		0.1400	0.1396
10	1	Top Wall		0.3057	0.3048
9	1	Aperture		0.5160	0.5163
9	1	Bottom Wall		0.0062	0.0062
9	1	Lip		0.0304	0.0306
9	1	Top Wall		0.1432	0.1422
8	1	Aperture		0.5634	0.5649
8	1	Bottom Wall		0.0085	0.0085
8	1	Lip		0.0097	0.0100
8	1	Top Wall		0.0777	0.0768
7	1	Aperture		0.5803	0.5809
7	1	Bottom Wall		0.0121	0.0123
7	1	Lip		0.0040	0.0041
7	1	Top Wall		0.0454	0.0450
6	1	Aperture		0.5858	0.5867
6	1	Bottom Wall		0.0180	0.0180
6	1	Lip		0.0021	0.0019
6	1	Top Wall		0.0277	0.0279

Table 3.2: Comparison of the view factors computed with the numerical method in the Fluent CFD package and the presented Monte-Carlo ray tracing method.

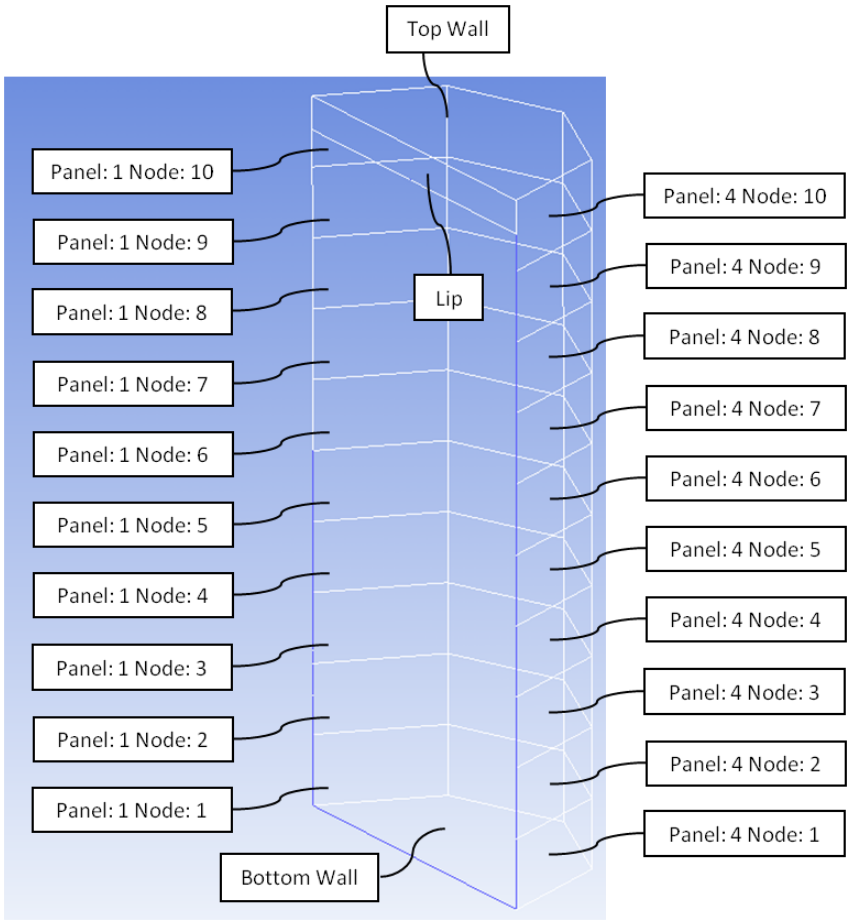

Figure 3.16: Surface description of the receiver configuration used for the Fluent-TRNSYS comparison in Chapter 6 (Receiver Configuration 1).

⇗4 Heat Transfer to the Working Fluid

In a central receiver CSP plant, the purpose of the receiver is to absorb concentrated solar energy radiation and transfer the energy to a working fluid for use in a conventional power cycle. Central receivers in CSP plants generally fall into one of two configurations: cylindrical and cavity. In a cylindrical receiver, the radiation absorbing surfaces are configured in the shape of a cylinder and wholly exposed to the ambient environment. In a cavity receiver, the active absorbing surfaces are shrouded in an enclosure. Concentrated solar radiation strikes the absorbing surfaces through a small aperture. The physical design of the cavity enclosure is not considered in the present project but the performance of the cavity receiver based on circuiting of the heat transfer fluid through the absorbing panels is considered and described in this chapter. In addition to the energy absorbed in the circulation of the heat transfer fluid through the panels, convective and radiative losses are modeled as described previously in Chapters 2 and 3

4.1 Heat Transfer Fluids

Two classes of coolants or heat transfer fluids are used in today's solar power towers: water in a latent energy change configuration and single phase sensible energy change salts. The Spanish PS10 cavity receiver is a latent energy change fluid design – producing steam from water. In this design, the receiver acts as the boiler in the steam power cycle and no intermediate heat exchanger is necessary, as it would be for two separate fluid cycles. Other examples, like the Solar Two power plant in California, use molten salt mixtures as the working fluid in the receiver tubes. Despite their higher capital costs, molten salts have potential advantages for thermal storage due to their higher density and lower pressure compared to steam. A widely used salt composition of 60% $NaNO_3$ and 40% KNO_3 can withstand relatively high operating temperatures (up to 866 K) and the high operating temperatures potentially permit greater turbine thermal efficiencies in the power cycles.

The main disadvantage of molten salts is their high freezing point temperature. For example, the 60% $NaNO_3$/40% KNO_3 mixture freezes at temperatures below 533 K. To prevent salt solidification in the receiver, the salt can be re-circulated from a "hot" storage tank to a second "cold" storage tank. Alternatively, the salt can be drained from the receiver at the end of an operating period. The first option continuously requires pumping power for the salt circulation, so the mass flow rates are kept as low as possible. Draining the receiver requires an initial heat load on the receiver surfaces to preheat the surfaces so that the salt does not freeze when it enters the tubes. A few heliostats can be used to preheat the panels for the startup at the start of every operation period.

Through personal communication with Dr. Kumar Sridharan from the Nuclear Department of the University of Wisconsin-Madison, Wagner (2008) obtained property data for twelve potential salt mixtures that were implemented in the TRNSYS receiver model property functions and also in the EES property database. The implemented salt mixtures and their applicable temperatures ranges are listed in Table 4.1. Some of the salts could be an option for the heat transfer medium in future solar plants that use high temperature steam turbine or Brayton gas turbine cycles, because of their high applicable maximum temperature. On the other hand, most of the candidates also have very high freezing temperatures, which complicate plant operation without salt freezing in the receiver tubes and the transport tubes between storage tanks and the receiver.

Salt Composition	Applicable Temperature Range
60% NaNO3, 40% KNO3	533 K - 866 K
59.5% NaF, 40.5% ZrF4	773 K -1623 K
59.5% LiCl, 40.5% KCl	628 K -1623 K
58% NaCl, 42% MgCl2	718 K - 1738 K
58% LiCl, 42% RbCl	586 K - 1323 K
58% KF, 42% ZrF4	773 K - 1623 K
49% LiF, 29% NaF	709 K - 1673 K
46.5% LiF, 11.5%NaF	727 K - 1843 K
31% RbF, 69% RbBF4	715 K - 1343 K
25% KF, 75% KBF4	733 K - 1343 K
8% NaF, 92% NaBF4	658 K- 969 K
68% KCl, 32% MgCl2	699 K - 1691 K

Table 4.1: Surface description of the receiver configuration used for the Fluent-TRNSYS comparison in Chapter 6 (Receiver Configuration 1).

4.2 Receiver Panel Energy Balance

The heat transfer from the absorbing panel/tube surface is limited by the thermal conduction resistance of the tube wall and the convection resistance from the inner panel surface to the fluid stream. In terms of a heat transfer resistance network, Equation (4.1) gives the heat transfer rate

$$\dot{q}_{HTF,i} = \frac{1}{R_{cond} + R_{conv}} \left(T_{s,i} - T_{HTF,avg,i}\right), \tag{4.1}$$

where $T_{s,i}$ and $T_{htf,avg,i}$ are the surface temperature and the average heat transfer fluid (HTF). Note that the index i denotes values that are evaluated on a nodal basis, where the nodes are defined as the vertical subdivisions of the receiver panels into discrete surfaces of

uniform temperature as described in Section 3.2.1.1. The average HTF temperature is calculated as the mean of the inlet and outlet HTF temperature at every node

$$T_{HTF,avg,i} = \frac{T_{HTF,i+1} + T_{HTF,i}}{2}. \tag{4.2}$$

The resistance to conduction of panel tubes is given by

$$R_{cond} = \frac{ln\left(\frac{D_{tube,in}}{D_{tube,out}}\right)}{2\,\pi\,\Delta l_{tube} k_{tube,i} N_{tubes}} \tag{4.3}$$

and the resistance to convection from the inner tube wall to the fluid is

$$R_{conv} = \frac{1}{h_{tube,i}\,\Delta l_{tube} D_{tube,in}\,\frac{\pi}{2} N_{tubes}}. \tag{4.4}$$

Factors that influence the heat transfer performance of the receiver including the conductivity of the tube material $k_{tube,i}$,the heat transfer coefficient $h_{tube,i}$ and the geometric parameters of the tube arrangement. Solving Equations (4.3) and (4.4) require the tube dimensions such as the inner and outer diameter of one tube, which are $D_{tube,in}$ and $D_{tube,out}$, respectively, the tube length per node Δl_{tube} and the number of tubes N_{tubes} that are parallel aligned in one panel. Assuming that only half of each receiver tube circumference is irradiated, only half of the inner tube surface area is considered in Equation (4.4). Conduction in circumferential direction in the tube wall can be neglected due to a much higher heat transfer resistance compared to the resistance in the radial direction. The heat transfer coefficients at every node $h_{tube,i}$ are determined using correlations for fully developed convection heat transfer in circular tubes; the correlations for laminar and turbulent flow are presented in Nellis and Klein (2009).

The heat transfer rate to the HTF per node can also be expressed through an energy balance on the coolant:

$$\dot{q}_{HTF,i} = \dot{m}_{HTF}\, c_{HTF,i}(T_{HTF,i+1} - T_{HTF,i}) \tag{4.5}$$

Besides the node inlet and outlet temperatures, $T_{HTF,i}$ and $T_{HTF,i+1}$, the energy rate is also a function of the mass flow rate through each panel node $\dot{m}_{HTF}$ and the specific heat of the fluid $c_{HTF,i}$. Given that the same mass flow rate is provided for each sequential node, conservation of mass is enforced throughout the model. Figure 4.1 illustrates the resistance network and explains the geometric quantities.

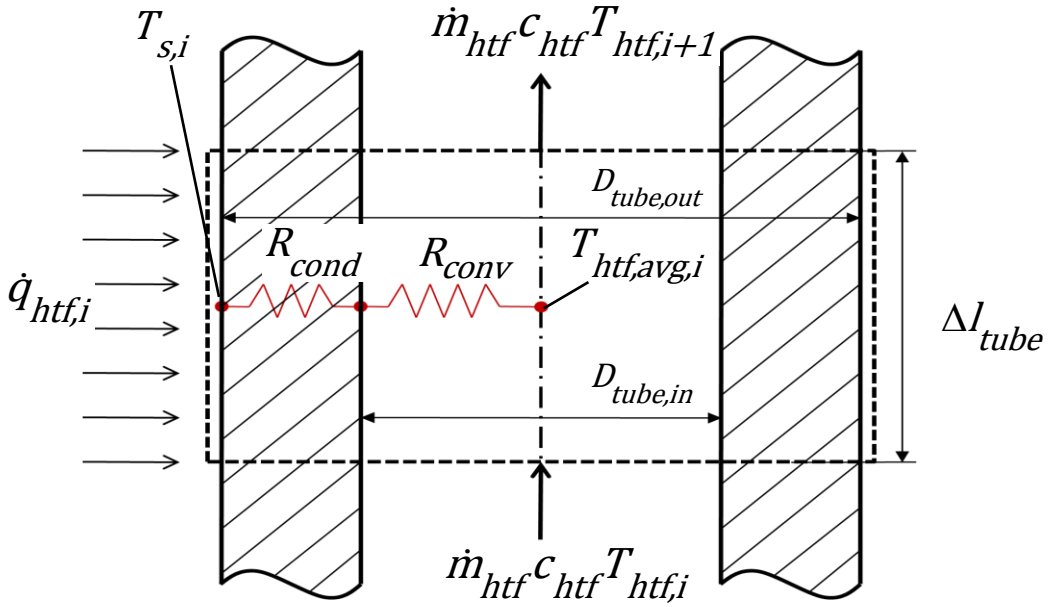

Figure 4.1: Receiver tube heat transfer model

4.3 Flow Configuration

For this cavity receiver model, it is assumed that each panel has a number of tubes (N_{tubes}) lined up in parallel in a serpentine arrangement from the bottom to the top as the simplified scheme in Figure 4.2 shows. The user of the model specifies the panel geometry by providing the panel width, the panel height and the outer tube diameter among others. In the example of Figure 4.2, the parallel tube bundle has 3 coils, where a single coil is defined as the tube arrangement marked by the dashed framing.

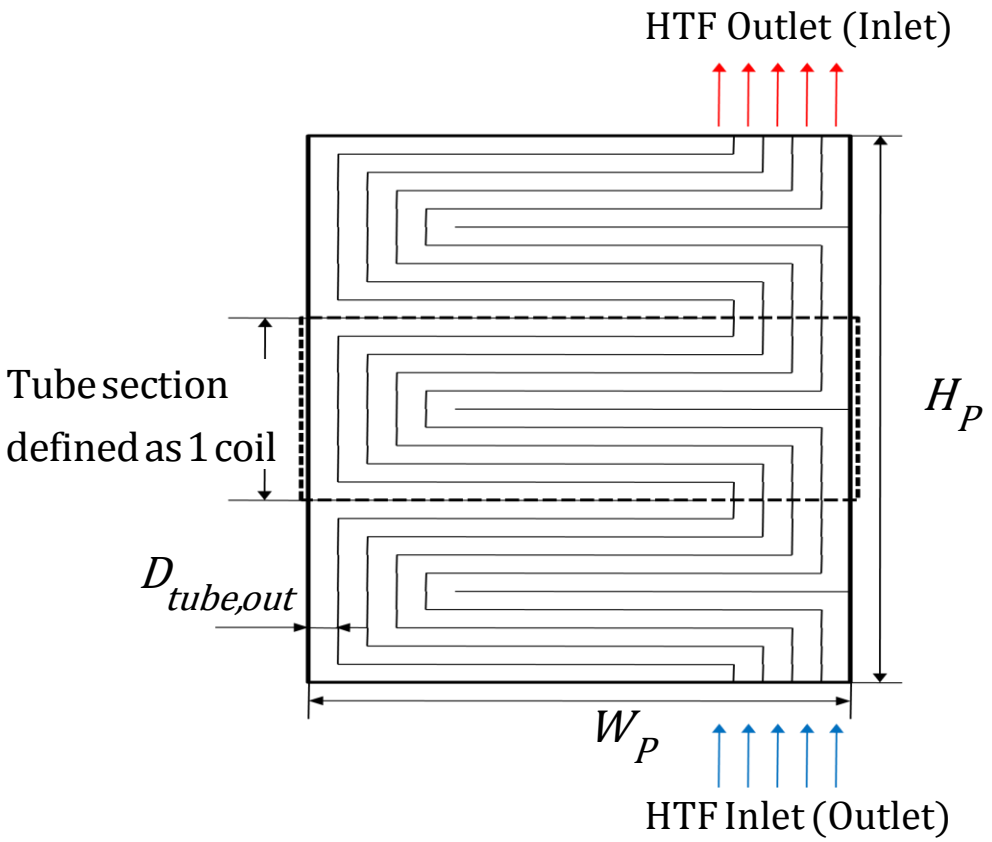

Figure 4.2: Simplified tube layout in each receiver panel (in the case shown above, the fluid flows from the bottom to the top)

The number of coils N_{coils} is arbitrarily fixed in the code to 6; but it can be easily changed; however, it is expected to have little influence on the performance of the receiver model.

Equations (4.3) and (4.4) require the number of tubes N_{tubes} per panel. Since a user-provided number would over specify the geometry, the tube number is calculated with

$$N_{tubes} = \left\lfloor \frac{H_P}{2\, N_{coils}\, D_{tube,out}} \right\rfloor. \tag{4.6}$$

By definition, the number of tubes can only be an integer value. In most cases, the combination of geometric parameters specified by the user will not return an integer from Equation (4.6). Then, the number of tubes is set equal the largest integer equal or smaller than the result. In the worst case it means that almost the area one tube would cover on each panel is not utilized for cooling.

The inlets and outlets of the four panels can be connected with each other in several ways. The cavity model utilizes eight different flow schemes that are shown in Figure 4.3. Flow patterns 1 and 2 have four parallel mass flows in the vertical direction. The hottest temperatures are at each panel in the top for the pattern 1 and the bottom for pattern 2. In contrast, flow types 3 and 4 have a serial connection between the panels such that only one stream is cooling each of the panels sequentially. For the remaining patterns 5 through 8, the total mass flow is split into two streams where each flows through two serially connected, adjacent panels. Flow patterns 5 and 6 have the fluid inlets at the outer panels while the inlets of patterns 7 and 8 are on the inner panels entering in the top and the bottom, respectively.

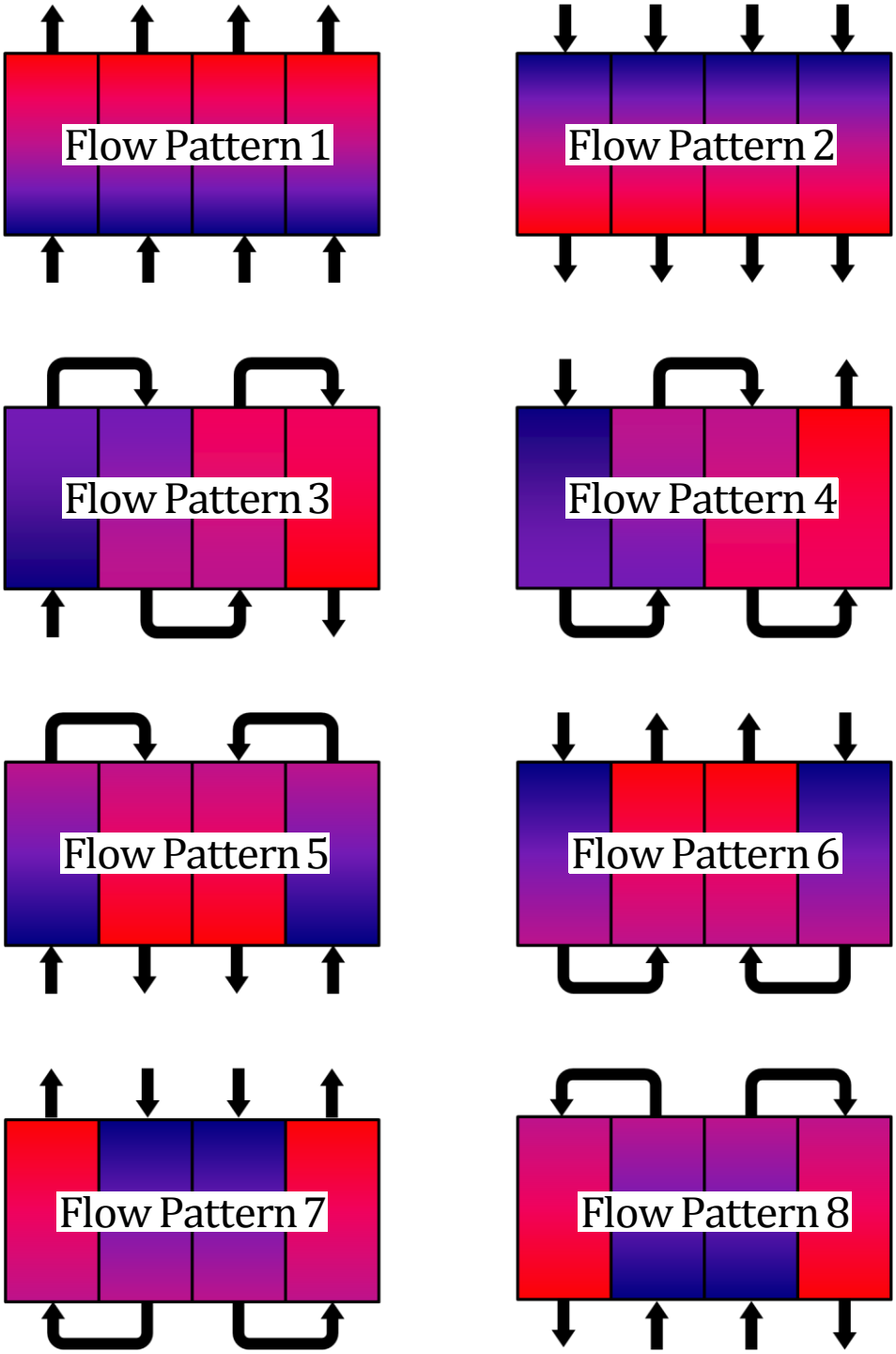

Figure 4.3: Eight different flow configurations based on combinations of different connections between the four panels. The colors mark the main temperature gradients of the coolant from the cold (blue) to the hot (red) inlet temperature.

4.4 Flow Side Plant Setup and Mechanical Pump Work

The coolant cycle is assumed to be an open system, where the fluid is pumped up to the receivers located near the top of the tower from a cold reservoir and returned to the hot storage unit after it is heated in the receiver. Therefore, the pumps have to provide the mechanical work to overcome the static head imbalance due to the tower height as well as the frictional pressure loss in the pipes.

As further explained in Chapter 5, the TRNSYS model adjusts the total mass flow rate of the tower to match the hot outlet temperature that is supplied by the user. For the flow patterns where the total fluid stream is split and routed through different panels, the received energy in each stream may differ due to the uneven flux distribution. Two methods to control the outlet temperature are considered:

1. The sub-streams have equal mass flow rates, and thus the receiver panel outlet temperatures will be different. After mixing of the sub-streams, the combined coolant flow will be at the final hot coolant temperature. Then the total mass flow rate can be adjusted to achieve the desired outlet temperature. The pressure drop is the same for each sub-stream.

2. Each sub-stream is controlled individually to achieve the desired receiver outlet temperature. That means, the mass flow rate and the pressure drop may be different for each panel.

For flow patterns 3 and 4, the methods are identical. Otherwise, the first option is technically less demanding because only one valve for the mass flow regulation and one temperature sensor are required. In comparison, the second option requires a valve at the inlet of each sub-stream and a temperature sensor at each outlet. The TRNSYS cavity receiver model assumes the second approach for the heat transfer modeling and for the calculation of the pressure drop. Even though the technical approach might be different, the overall pressure

drop and the total mass flow rate will approximately be the same for both methods. The static head difference due to the total tower height including the receiver height H_{tower} is calculated with

$$\Delta p_{tower} = g \rho_{HTF,cold} H_{tower}. \tag{4.7}$$

The density of the fluid ρ_{HTF} is evaluated at the temperature provided by the cold storage tank. The pressure loss caused by the panel pipe friction is calculated for every panel node separately:

$$\Delta p_i = \frac{1}{2} \rho_{HTF,i} u_{HTF,i}^2 \, f_{htf,i} \left(\frac{\Delta l_{tube}}{D_{tube,in}} + \frac{N_{bends,45}}{N_{nodes}} \, 16 \right) \tag{4.8}$$

The friction factor $f_{htf,i}$ is a function of the nodal Reynolds number

$$Re_{htf,i} = \frac{u_{HTF,i} \rho_{HTF,i} D_{tube,in}}{\mu_{htf,i}} \tag{4.9}$$

and the relative roughness of the inner tube surface is set to $45 \times 10^{-6} m / D_{tube,in}$, typical for commercial steel. The correlations for the friction factor calculation for laminar and turbulent flow are also summarized in Nellis & Klein (2009). In Equation(4.8), the dynamic pressure at each node is multiplied by the friction factor and the equivalent length divided by the inner diameter. The last summation term in Equation (4.8) accounts for the additional relative length due to the tube bends as presented in Figure 4.2. $N_{bends,45}$ is the number of 45° degree bends per panel and the corresponding relative length $L/D = 16$ was found in Fox, McDonald, & Pritchard (2006).

The nodal pressure drops are summed up for the pressure loss per panel.

$$\Delta p_{panel} = \sum_{i=1}^{N_{nodes}} \Delta p_i \tag{4.10}$$

For flow patterns 1 and 2, the total pressure drop due to friction effects in the receiver pipes is calculated by averaging the panel pressure losses:

$$\Delta p_{rec} = \frac{\dot{m}_{HTF,1}\,\Delta p_{panel,1} + \dot{m}_{HTF,2}\,\Delta p_{panel,2} + \dot{m}_{HTF,3}\,\Delta p_{panel,3} + \dot{m}_{HTF,4}\,\Delta p_{panel,4}}{\dot{m}_{HTF,total}} \qquad (4.11)$$

The indices 1 through 4 denote the different values for mass flow rate and pressure drop at each of the four receiver panels. $\dot{m}_{HTF,total}$ is the total receiver throughput of the heat transfer fluid. For flow patterns 3 and 4, the total pressure drop due to friction effects is simply the sum of all nodal pressure drops. The pressure losses for flow patterns 5 through 8 are calculated analogous to Equation (4.11).

The required overall pumping power is calculated with Equation (4.12):

$$\dot{W}_{pump} = \dot{m}_{HTF,total}\left(\frac{\Delta p_{tower}}{\rho_{HTF,cold}} + \frac{\Delta p_{rec}}{\rho_{HTF,avg}}\right)\frac{1}{\eta_{pump}} \qquad (4.12)$$

The density of heat transfer fluid is assumed to be independent of pressure but dependent on temperature therefore the density is changing as a function of the temperature. In Equation(4.12), the density is evaluated at the cold HTF temperature ($\rho_{HTF,cold}$) and the mean of the cold and hot temperature ($\rho_{HTF,avg}$). A pumping efficiency that has to be provided by the model user is also included.

All required heat transfer and flow concepts to model the thermal receiver behavior have been described in detail during the previous Chapters 2, 3, and 4. The next chapter describes the implementation of the presented models and correlations into the TRNSYS cavity receiver component.

⇗5 The TRNSYS Cavity Receiver Component

Initially, the solar power tower cavity-type receiver model was developed in EES (F-Chart, 2009) to simplify the solution process, because EES is capable of solving a set of implicit equations simultaneously through numerical iteration procedures. To utilize the developed cavity receiver thermal model in the "Solar Advisor Model", the existing EES code had to be transformed into Fortran suitable for use as a TRNSYS component. The Fortran code for the complete receiver component uses a skeleton that was created with TRNSYS to fulfill its format requirements. The newly created cavity receiver component is called *Type230*.

5.1 Introduction to TRNSYS

In TRNSYS, energy systems are simulated through a network of single components that resemble physical parts of the real system. A component usually contains numerical methods and equations to model the physics that describe the behavior of the specific system part. The components are connected by linking the outputs of one component to the inputs of another where the transferred data are usually time-dependent quantities.

For example, a solar power tower consists of the component models of the heliostat field, receiver, storage system, power cycle, and control system. The insolation level and the sun position are provided by a weather data component. Through the connection network, the components exchange information like coolant temperatures, fluid flow rates, heliostat field efficiency, fluid volumes in the tanks, etc.

For transient systems, TRNSYS iterates between all components at each time step until a state of equilibrium is found. The simulation then advances in time. That means each component can be called multiple times at a single time step until changes in the output values compared to the previous call are smaller than user-specified error tolerances.

5.2 Inputs/Outputs of the Cavity Receiver Component

All TRNSYS components have a list of inputs, outputs and parameters. The inputs are time-dependent quantities that are provided by other components, user-defined equations, or data files. The parameters are independent of time and they have to be specified in the component unit itself or they can be provided as constants by user-defined equations. The outputs are calculated quantities of interest for a component based on its inputs and parameters. Outputs of a component can be used as inputs for other units or printed as simulation results.

Table 5.1 lists the required parameters, inputs, and the returned outputs for the cavity receiver component – Type 230. The Fortran variable names used in *Type230* are listed in the first column. A brief description of the variables and their units are given in the second and last columns, respectively.

Parameters		
Variable	**Description**	**Units**
R_rec	Radius of the vertical cavity cylinder	m
H_rec	Height of a receiver panel	m
RecAngle	Section of the cavity circle covered with panels	deg
H_lip	Height of the upper lip of the cavity	m
THT	Total height of the solar tower	m
D_tube_out	Outer diameter of a single tube	mm
th_tube	Wall thickness of a single tube	mm
HTF	Flag indicating the heat transfer fluid	-
FlowPattern	Flag indicating coolant flow scheme	-
LU_flux	Logical unit for the flux map file	-
LU_status	Logical unit for the status file	-
LU_viewfactor	Logical unit for the view factor file	-

Inputs		
Variable	**Description**	**Units**
hour	Hour of the day	hr
azimuth	Solar azimuth angle	deg
zenith	Solar zenith angle	deg
T_amb	Ambient atmospheric temperature	C
T_dp	Ambient dew point temperature	C
P_amb	Ambient atmospheric pressure	atm
P_htf	Pressure of the heat transfer fluid	bar
I_bn	Direct (beam) normal irradiation	kJ/m^2-hr
efficiency_field	Overall efficiency of the heliostat field	-
efficiency_pump	Efficiency of the pump for the working fluid	-
hel_stow_deploy	Heliostat field stow/deploy solar angle	deg
T_htf_cold	Inlet temperature of the heat transfer fluid	C
T_htf_hot	Desired hot outlet temperature of the working fluid	C

Outputs		
Variable	**Description**	**Units**
Q_thermal	Thermal energy absorbed by the heat transfer fluid	MWt
Q_radiation_loss	Thermal radiation losses from the receiver	MWt
Q_convection_loss	Thermal convection losses from the receiver	MWt
W_pump	Estimated power for pumping the working fluid	MWe
m_htf_total	Total mass flow rate of the working fluid	kg/hr
efficiency_thermal	Thermal efficiency of the receiver	-
T_htf_hot	Outlet temperature of the heat transfer fluid	C
-not named-	Receiver power prior to thermal losses	MWt

Table 5.1: Parameters, Inputs and Outputs of the Type230 TRNSYS Cavity Receiver

The parameters contain mainly quantities that determine the receiver geometry (*R_rec*, *H_rec*, *H_lip*, and *theta*), tower height (*THT*) and specifications for the receiver's fluid tubes (*D_tube_out* and *th_tube*). Furthermore, the number of vertical temperature nodes per panel has to be specified (*N_nodes* can be 1, 2, 5, or 10). The heat transfer fluid (*HTF*) is selected using integer values ranging from 1 to the maximum number of available options in the list, which are eleven different molten salts at this point. The variable *FlowPattern* must be given an integer between 1 and 8, which determines the coolant flow scheme through the receiver panels as described previously in Chapter 4.

Some of the inputs for the receiver unit might be set to constant values for a yearly simulation run. For example, the efficiency of the pump that moves the HTF fluid (*efficiency_pump*), the hot fluid outlet temperature, or the minimum solar elevation angle to start up the power plant might be variables that will probably be constant over the course of the year.

5.3 Information Stored on External Files

Aside from the connections with other components, the cavity receiver component accesses external files that are stored in the same folder as the input file for the TRNSYS project. The input file, also called "deck" file, identifies the components, the connection network and controls the simulation.

5.3.1 The Flux Map File

As mentioned in Chapter 3, the initial plant optimization and the heliostat field layout for the solar power tower are determined during a pre-processing step using DELSOL3 and PTGen. PTGen is a program that Wagner (2008) developed as a front-end to facilitate the use of the DELSOL power tower simulation code. DELSOL itself is limited to computing a single flux map at each performance run. Since this procedure is impractical for the application in TRNSYS at each time step, PTGen creates a file called *fluxmap.csv* that contains 96 flux maps in total. The 96 flux maps represent the hourly flux distributions for 8 representative

days during half of a year. The days are equally spaced by solar declination angle from the winter to the summer solstice and a mirror image of the maps is applied from the summer solstice to the winter solstice. Figure 5.1 shows the uniformly distributed solar positions as a function of the azimuth and zenith angle.

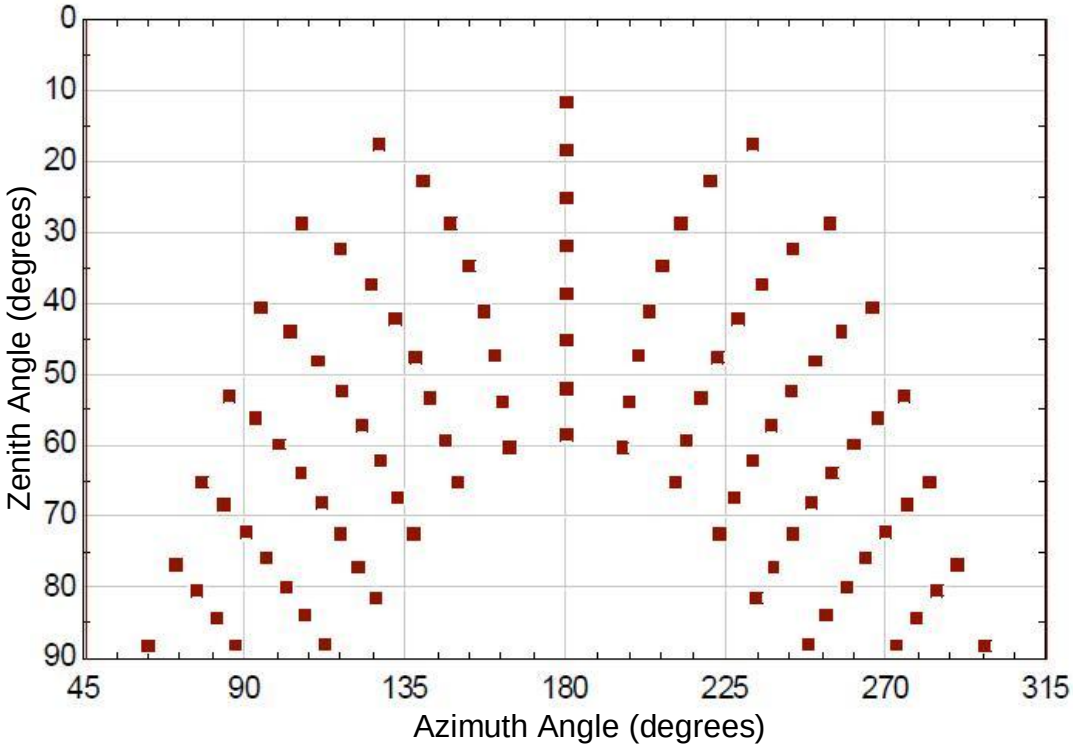

Figure 5.1: Solar positions used for the flux maps spaced equally by declination angle (Wagner, 2008).

During each time step in Type 230, TRNSYS uses the flux map corresponding to the solar position for the current time closest to the solar positions provided in the *fluxmap.csv* file. In a sensitivity study, Wagner (2008) showed this approximation affects the total solar flux by maximal 0.53% and it was considered an appropriate technique. Each flux map approximates the flux distribution onto the active receiver panels through a two-dimensional array with 10 values for the vertical distribution at 12 horizontal positions. Examples of the flux distributions are given in Figures 3.1 and 3.2.

Apart from the flux distribution, the heliostat performance is characterized by the field efficiency as defined in Chapter 3. PTGen outputs an array of field efficiency factors

dependent on the solar position and stores the efficiency values in the *eff_array.dat* file. This file is read and interpreted by the TRNSYS heliostat field component originally developed by R. Pitz-Paal and modified by Wagner (2008). The field efficiency is then provided to the receiver component as an input value.

5.3.2 The View Factor File

In a yearly simulation run, the geometry of the cavity receiver itself is constant; therefore, it is convenient to compute and store the radiation view factors for each of the interior surfaces of the receiver as well as the aperture once before the transient simulation starts so that they can be accessed at each time step. Since the analytical view factor relationships described in Section 3.2.2.1 were implemented in an EES program, the results are stored on an external file that is read by the TRNSYS component. The EES program calculates and stores the view factors in a file called *viewfactor.csv*.

5.4 First Call Manipulations of the Receiver Component

Before the transient simulation starts, a few variables are calculated in the first call of the receiver unit. As explained in the previous section, some of the necessary view factors were calculated with a program written in EES and stored on the *viewfactor.csv* file. The missing factors are determined with subroutines that apply the Monte-Carlo method explained in Section 3.2.2.2. Because TRNSYS provides a storage array variable for each unit, it is convenient to write the resulting view factors into a storage array that can be accessed at every call to the cavity receiver unit.

For this model setup, the coolant flow rate is calculated such that its outlet temperature matches the initially specified parameter for the hot fluid temperature. Hence, the temperature gradient of the fluid flowing through the receiver panels and the panel surface temperatures are approximately constant - independent of the level of solar radiation. When

the beam radiation is low, which occurs especially in the morning or evening times, the radiation and convection losses, which are only dependent on the surface temperatures, are larger than the total incident solar radiation. In this situation, the simulation is not able to converge because the desired outlet temperature cannot be achieved. To reduce wasted computation time at the hours of insufficient solar radiation, the first call to the receiver unit before each yearly simulation identifies this critical radiation level (CRL). If the total incident radiation is below the CRL, the simulation will indicate that the power outputs and mass flow rates are 0. Then the receiver unit returns control to the main TRNSYS program without further iteration.

The critical solar radiation level is determined by calling the *CavityReceiverModel* routine during the initial receiver unit call. The user-specified set of parameters and a set of reasonable inputs that are specified in the code are passed to the routine. It returns values for the heat losses which are assumed to be relatively constant with little variation due to changing ambient conditions. The critical solar radiation level is specified as the sum of the absolute values for the radiation and convection heat losses out of the receiver. This variable is also passed to the storage array to make it available at every unit call.

5.5 Transient Program Flow in Fortran

At each time step, the *Type230* TRNSYS component calls the subroutine *CavityReceiverModel* and passes it the required inputs and parameters. In this subroutine, the computations for the thermal modeling are performed and the output variables are returned to the main body of the *Type230* program. Before *Type230* returns control to the TRNSYS kernel, the storage variables are updated and output values are converted to the externally used units.

After entering the *CavityReceiverModel* routine and declaring the variables, the code checks the solar position and the direct normal radiation. If no radiation is available or the solar

elevation is below the minimum defined by the *hel_stow_deploy* variable, the power output values are set to 0, the outlet HTF temperature is set equal the inlet temperature, and control is returned to the main program.

At daytime hours, where the solar position is valid and the radiation is greater than 0, the inputs and parameters are converted to the SI unit system. Wagner (2008) wrote functions to perform all necessary unit conversions for this application. In addition, all required geometric quantities are calculated from the inputs and parameters. In the next step, the array in the *viewfactor.csv* is read and distributed to local view factor array variables. Subsequently the incident radiation onto each surface node has to be determined. The function *getFluxMap* picks one flux map from the *fluxmap.csv* file that has the closest match of solar angles and returns the flux values in a two-dimensional array with 10 rows and 12 columns. Since DELSOL3 assumes a direct normal irradiance (DNI) of $950\ kW/m^2$ and no losses from the heliostat field for the flux map calculation, the actual DNI (I_{bn}) value and the field efficiency (η_{field}) is used to scale the flux map correctly for every hour.

```
DO i=1,10
    DO j=1,12
        fluxarray(i,j)=fluxarray(i,j)/(950.0)*I_bn*efficiency_field
    ENDDO
ENDDO
```

Note that the receiver model approximates the temperature and flux distribution with four nodes in the horizontal direction based on the geometry with four panels. Also the vertical number of nodes might not conform to the amount of vertical flux values provided in the flux map. In the final component, the number of nodes in the vertical direction was set to 10 for the radiation calculations. A sensitivity study in the next section shows the proportions for deviations in thermal performance and computational time due to the different node numbers. However, during the model development the node number was kept as a variable at first and fixed later to 10 in the beginning of the program code. For the algorithm that averages the 10 provided vertical flux values for the number of vertical nodes, the possible numbers for the node parameter were constrained to 1, 2, 5, or 10. This limitation simplifies the algorithm, because 10 divided by one of these four input numbers results in an integer instead of a

fraction. Limitation of the vertical node parameter also facilitates the programming by implementing only four different cases for every possible node input. This averaging routine is called *translateFluxArray* and it transforms the 10x12 flux array into an array with four columns and the same number of rows as number of vertical nodes for the model were specified (i.e. 1, 2, 5, or 10). Note that the input and output arrays to the *translateFluxArray* routine have equal overall average irradiation values. To obtain the absolute solar radiation on each surface node, the flux values are multiplied by the nodal area in the next step. The radiation rate values are converted from kW to W.

```
DO i=1,N_nodes
    DO j=1,N_panels
        q_solar(i,j) = 1000.0*A_node*solarflux(i,j)
    ENDDO
ENDDO
```

The sum of the absolute solar radiation array results in the total incident radiation. A further check is performed: If the total incident radiation is higher than the critical radiation level (CRL) determined at the first simulation call, the code continues normally. Otherwise, it returns zeros for the power outputs, the mass flow rate and thermal efficiency and sets outlet HTF temperature equal the inlet temperature and gives the control back to the *Type230* main program.

When the incident radiation exceeds the CRL, guess values are allocated to all surface temperatures, the coolant temperatures at each node and the coolant mass flow rates. The hot HTF outlet temperature is assigned to the surface temperature and the component iterates to find the fluid flow rate that achieves the hot HTF at the desired temperature leaving the receiver. For the stability of the code, good guess values of the coolant flow rates and temperatures are important. The distribution of the fluid temperatures and the stream arrangement is dependent on the flow pattern. A sample code is shown for flow type 1.

```
IF (FlowPattern.EQ.1) THEN
    DO j=1,N_panels
        m_htfX(j) = efficiency_thermalX*q_solar_panel(j)&
                  /(c_htf_avg*(T_htf_hot-T_htf_cold))
        DO i=1,N_nodes
            T_htfX(i,j) = T_htfX(i-1,j)&
                        + efficiency_thermalX *q_solar(i,j)&
                        /(m_htfX(j)*c_htf_avg)
            T_htf_avgX(i,j) = (T_htfX(i,j)+T_htfX(i-1,j))/2.0
        ENDDO
    ENDDO
```

First, guesses for mass flow rates are calculated by dividing the total solar radiation on one panel by the product of the average specific heat and the temperature difference between the hot outlet and the cold inlet temperature of the fluid. This quotient is multiplied by a guess value for the total thermal efficiency, which is set to 0.9. This value was determined by a runtime evaluation. The average specific heat of the fluid is evaluated at the mean of the hot and cold coolant temperature. Knowing the guess values for the mass flow rates, the fluid temperatures are calculated at each node by balancing the thermal energy gain in the fluid with the product of the incident solar radiation per node and the thermal efficiency. All variables marked with a capital x are guess values. Note that for different flow patterns the calculation of the mass flow rates and temperatures are analog to the example above, but some of the looping structures are more complex due to different boundary conditions and flow setups.

After the guess values for flow rates and temperatures have been assigned, the simulations runs through an iteration loop that solves the implicit energy balances for all nodes numerically. At first, the relative errors for the convergence criteria are defined:

$$error_{temp} = \frac{\left|T_{htf,hot} - T_{htf,hotX}\right|}{T_{htf,hot}} \tag{5.1}$$

$$error_{flow} = \frac{\left|\dot{m}_{htf} - \dot{m}_{htfX}\right|}{\dot{m}_{htfX}} \tag{5.2}$$

The temperature error in Equations is the difference between the hot HTF set temperature provided by the user and the updated guess value for the outlet temperature divided by the

desired temperature in degrees Kelvin. Equation (5.2) calculates the difference between the most recently updated mass flow rate and the preceding value divided by the newest guess value. Assuming a flow pattern with multiple separate fluid streams was chosen, the single errors for each stream are added together. If the error sum is smaller than the defined convergence criteria (see Figure 5.5), the iteration is exited. In case the calculations do not converge after a certain number of iteration, the routine returns the zero set for the output power and mass flow rates.

Next, the fluid properties and flow conditions at each node are updated with every iteration step. To compute the heat transfer resistances to conduction and convection as explained in Section 4.2, the fluid density, viscosity, specific heat and conductivity are required. For the thermal resistance to conduction of the tube wall, the conductivity of the tube material is needed. The properties are calculated with functions written by Wagner (2008) that contain polynomial curve fits to the experimental property data of the molten salts and the assumed tube metal "Stainless Steel AISI316". With the property values and mass flow rates, the dimensionless numbers that characterize the flow are computed. Then, the Reynolds and Prandtl numbers are provided to the *PipeFlow* that was also written by Wagner (2008) for the external receiver model. This routine calculates the friction factor and the Nusselt number with correlations for fully developed internal pipe flow as described in Section 4.2.

The radiation exchange rate between surface i and the surroundings surfaces $j = 1..N$ is proportional to the surface temperature $T_{s,i}$ to the fourth power. By re-arranging Equation (3.2) the radiation term can be expressed as a linear function of the surface temperature $T_{s,i}$:

$$\dot{q}_{rad,net,i} = \sigma A_i \sum_{j=1}^{N} F_{i-j}(T_{s,i}^4 - T_{s,j}^4) = A_i \sum_{j=1}^{N} h_{rad,i-j}(T_{s,i} - T_{s,j}) \qquad (5.3)$$

However, the radiation heat transfer coefficients are still a function of the surface temperature:

$$h_{rad,i-j} = \sigma F_{i-j}(T_{s,i}^2 + T_{s,j}^2)\,(T_{s,i} + T_{s,j}) \qquad (5.4)$$

The coefficients are calculated with the guess values for the surface temperatures that are successively updated in every iteration step. Accordingly, the energy balances around each surface node can be solved to calculate new surface temperatures. The general energy balance around every surface node i is described by:

$$\dot{q}_{solar,inc,i} = \dot{q}_{HTF,i} + \dot{q}_{rad,net,i} \tag{5.5}$$

The incident solar radiation values on each node $\dot{q}_{solar,inc,i}$ were obtained at an earlier point in the code, but the other two terms in Equation (5.5) are still unknown and can be expressed as following:

$$\dot{q}_{solar,inc,i} = \frac{T_{s,i} - T_{htf,avg,i}}{R_{cond,i} + R_{conv,i}} + A_i \sum_{j=1}^{N} h_{rad,i-j}\left(T_{s,i} - T_{s,j}\right) \tag{5.6}$$

The index i represents the ith surface of constant temperature and N is the number of total surfaces. Equation (2.3) is solved for the surface temperature $T_{s,i}$:

$$T_{s,i} = \frac{\dot{q}_{solar,inc,i} + A_i \sum_{j=1}^{N} h_{rad,i-j} T_{s,j} + \dfrac{T_{htf,avg,i}}{R_{cond,i} + R_{conv,i}}}{\dfrac{1}{R_{cond,i} + R_{conv,i}} + A_i \sum_{j=1}^{N} h_{rad,i-j}} \tag{5.7}$$

Note that the energy balances (5.5)–(5.7) do not include terms for the convective heat losses. It was shown in Section 2.2.3 that the effect of the convection losses to the ambient is negligible on the surface temperatures. Also the convection loss correlations are formulated for the total losses from the receiver, but how the total losses influence the temperatures for each part of cavity surface cannot be directly determined. Thus, the total convection losses are computed after the iteration loop has determined the surface temperatures. As shown in Section 2.2, the surface temperatures are slightly higher compared to calculations with a model where the convection heat transfer to the ambient, the radiation exchange and the heat transfer to the fluid are all coupled in the energy balances. This technique provides a conservative estimate for the total thermal energy gain in the fluid because overestimation of the surface temperatures results in a higher heat loss rate from the receiver. The heat transfer

rate to the coolant is determined using Equation (4.1). With these new values for the thermal energy transfer to the fluid, the mass flow rates and the fluid temperatures can be updated similar to the way it was done for the initial guess values. Again, the looping structure depends on the flow pattern.

After the energy balances for all active surface nodes are solved and the fluid flow rates and temperatures are updated, the temperatures of the inactive, adiabatic surfaces are computed. This is accomplished with energy balances analogous to Equation , except the heat transfer rate to the fluid is zero. When the accepted accuracy is achieved and the iteration loop is exited, the convection heat losses to the ambient are determined with a subroutine that applies the Clausing model (Clausing, 1987) that was described in Chapter 2. A routine for the Siebers & Kraabel (1984) model was also included and can be applied by simply changing the variable *ConvectionModel*. After subtracting the convection losses from the total energy gain in the fluid, the total mass flow rate is updated and the thermal efficiency of the receiver is determined by dividing the heat transfer rate to the coolant by the total incident radiation onto the receiver panels. Finally, the pressure losses and the pumping power are computed according to the method presented in Section 4.4. Back in the *Type230* program, the output values are converted to the external units that used in the TRNSYS simulation.

In this analysis, the weather data were provided by TMY (Typical Meteorological Year) files, which provide the data on an hourly basis. Assuming the system dynamics happen within timescales much smaller than one hour, the receiver component can be modeled as quasi-steady: When the input quantities change for the next time step, the system iterates until it finds the equilibrium between all parameters. This equilibrium remains constant until the next hourly change. Thus, all balance equations within the model describe steady-state processes.

Figure 5.2 illustrates the flow scheme for the TRNSYS cavity receiver component. Note that the element shown as *ViewFactorRoutines* consists of six subroutines:

OuterPanel_Floor: View factors between surface nodes of the outer panel and the floor

InnerPanel_Floor: View factors between surface nodes of the inner panel and the floor

Lip_Ceiling: View factors between the lip surface and the top surface

Lip_Floor: View factors between the lip surface and the bottom surface

Opening_Floor: View factors between the aperture (cavity opening) and the floor

Opening_Ceiling: View factors between the aperture (cavity opening) and the ceiling

The following section of this chapter shows how the model responds to different settings for the flow patterns, the surface discretization, the convergence criteria, etc.

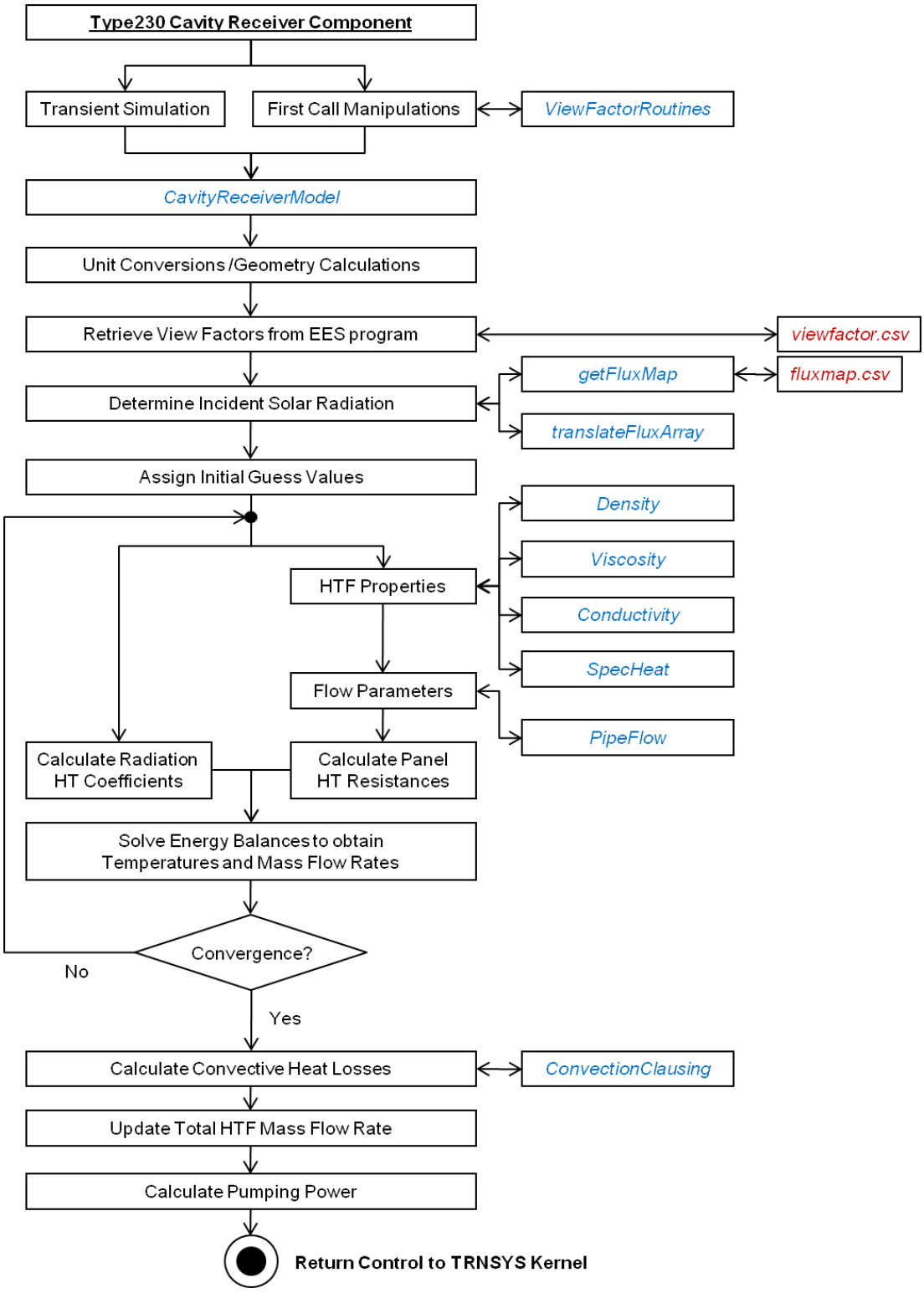

Figure 5.2: Flow chart of the Type230 cavity receiver component (blue elements are subroutines, red elements indicate external files).

5.5 HTF Flow Pattern Testing

The possible choices for the flow pattern parameter were presented in detail in Section 4.3. Figure 4.3 showed the inlet and outlet position for the heat transfer fluid and the predicted coolant temperature gradients across the panels. In this study, simulations with each flow type were run over a typical meteorological year in Daggett, California and the influence of the flow pattern on the thermal receiver performance was estimated.

Abengoa's PS10 11MW cavity receiver power plant was used to represent the plant design for this test. However, the 60% NaNO3/40% KNO3 salt mixture is used for the working fluid instead of steam as for the Abengoa plant. The simulated plant utilizes two storage tanks: one for storing hot molten salt heated by the receiver and the other for storing cooler salt returning from the power block. A Rankine steam cycle converts thermal energy into electricity. The boiler in the power cycle is "fueled" by the heat from the hot salt delivered by the receiver and/or hot storage tank at a temperature of 565°C. The cooler salt leaving the boiler is returned to the cold tank at temperature of approximately 290°C with small variations. Important values for the receiver geometry are given in Figure 2.3. DELSOL3/PTGen was used to optimize the north-based heliostat field and generate the flux map file.

Two different yearly simulations were conducted for each flow pattern. First, the single point aiming technique in DELSOL3 was utilized for the flux map generation. To account for a more uniform flux distribution, the two-dimensional smart aiming technique was also applied. In Section 3.1, these heliostat focusing techniques are explained in detail, and Figure 3.1 and 3.2 show flux distribution examples for both cases. Figure 5.3 shows the monthly average thermal efficiencies for flow patterns 3 through 8 when the single point aiming techniques were applied. Flow types 1 and 2 were not included because in these cases the code was not able to converge for this aiming technique. Focusing the solar flux on the central part of the receiver causes insufficient energy gain in the outer panels in order to have significant flow rates. Note that flow patterns 1 and 2 have four parallel mass flow streams: one independent flow rate through each receiver.

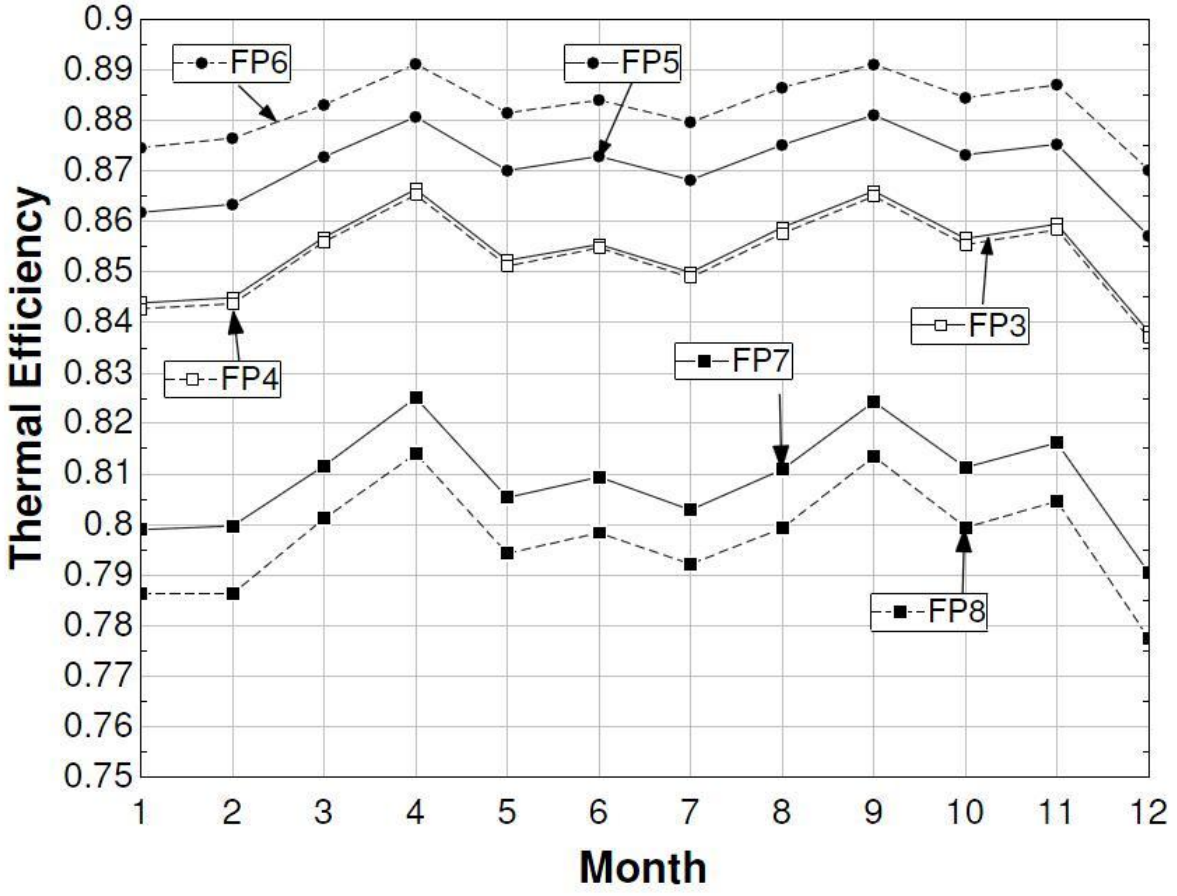

Figure 5.3: Monthly averaged thermal receiver efficiencies applying the single point aiming technique for the solar flux distribution.

Application of the smart 2D aiming technique shows converged results for all flow patterns in Figure 5.4. However, the results for flow patterns 1 and 2 still show convergence issues for a few hours of the year. These problems can be observed in the differently shaped graphs for flow pattern 1 and 2 compared to the remaining plots. The thermal efficiency in both graphs is defined as:

$$\eta_{thermal} = \frac{\dot{q}_{solar,inc,total} - \left(\dot{q}_{loss,rad} + \dot{q}_{loss,conv}\right)}{\dot{q}_{solar,inc,total}} \tag{5.8}$$

Clausing's convection loss model (Clausing, 1987) is used to compute the convection heat losses from the receiver in Equation (5.8).

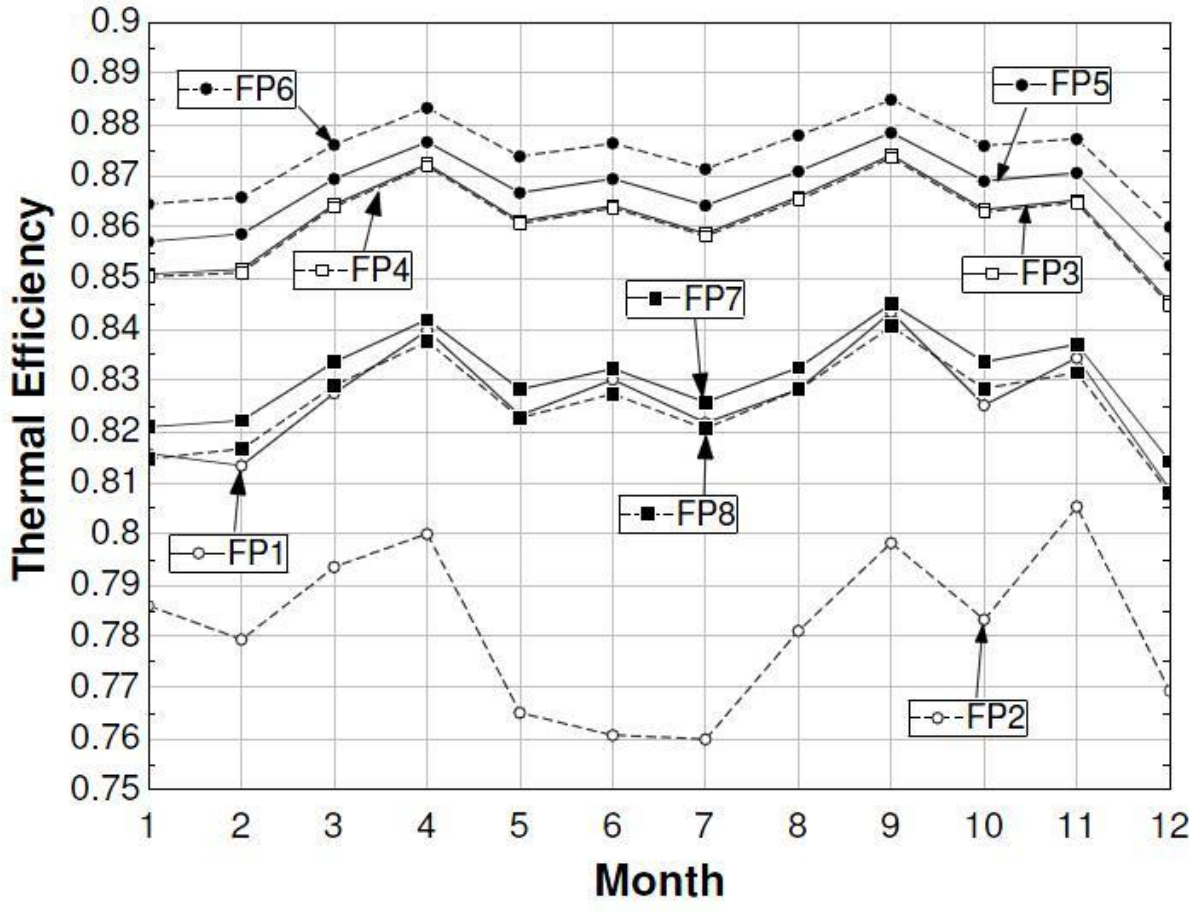

Figure 5.4: Monthly averaged thermal receiver efficiencies applying the 2D smart aiming technique for the solar flux distribution.

Both figures show the lowest average heat loss rates for flow types 5 and 6 followed by patterns 3 and 4. Apart from the constant parameters, e.g. the receiver geometry, the radiation and natural convection heat losses are only a function of the wall temperatures inside the cavity and the ambient temperature. Higher efficiencies are correlated to a lower average surface temperature of the wall area inside the cavity. The coolant and wall temperatures are directly influencing each other due to their coupling through conductive and convective heat transfer. Since the inlet and outlet temperatures of the working fluid are provided as inputs, the surface temperature distribution is also a function of the input values for the fluid temperatures. Despite the attempt to spread the flux with the smart aiming technique, the major part of the solar radiation is incident on the center part of the active

receiver area. This causes the strongest temperature increase in the fluid and surface temperature on the inner two panels. Flow patterns 5 and 6 each have their fluid outlets at the inner panels; thus, the part of the fluid that is at the highest temperatures travels a relatively small distance until it exits the receiver. Flow pattern 6 also shows a higher efficiency compared to flow type 5 because the part at maximum temperature is located in the top of the receiver which is shielded to the ambient by the upper lip and therefore reduces heat losses.

In contrast, flow patterns 7 and 8 have the coolant inlets at the inner position. In these cases, the fluid gets heated directly after it enters the receiver and it flows at a very high temperature through the tubing system. Uneven flux distributions that focus most of the solar radiation onto the central receiver part cause the fluid to reach its highest temperature in the area of the concentrated flux. Then the fluid cools in the outer panels because the heat loss rates exceed the relatively low incoming radiation. The mass flow rate is adjusted such that after the initial temperature increase and the cooling in the outer panels, the desired outlet temperature is achieved. The efficiency of these distributions is comparatively low because of high average surface temperatures. Furthermore, the maximum fluid temperature exceeds the desired outlet temperature when it passes the high flux region. This could lead to a decomposition of the molten salts and also damage if the temperature exceeds the applicable range.

Multiple outlets where the fluid is heated to the specified outlet temperature or above (see flow types 1 and 2) also have a negative effect on the thermal efficiency because it increases the hot surface area on the receiver.

In summary, the average surface temperature should be minimized if the thermal receiver efficiency is the primary goal. Specifying low inlet and outlet temperatures of the receiver will lead to low surface temperature and higher mass flow rate, but the low temperature fluid might not be useful for energy conversion anymore. The simulations with different flow patterns showed that positioning the fluid outlet of the panel close to the area with the highest flux will decrease the overall surface temperature. On the other hand, flux limitations and

receiver life time considerations may set boundaries for this approach. In this case, it should be considered to cool the highest flux regions with the coolant at the lowest temperature because of material flux limitations.

5.6 Sensitivity Studies

A few sensitivity studies were conducted to gain further understanding of the model and the influence of certain parameters. The sensitivity to the vertical number of nodes on the thermal performance of the model is tested. In addition, the influence of some parameters like the minimum error at which convergence of the model is assumed and the boundary condition for the aperture are investigated.

5.6.1 Influence of the Node Number

Testing of the TRNSYS receiver conducted was conducted to gain information on the sensitivity of the model results towards the number of nodes used for the energy balances and the property evaluation, where a uniform temperature is assumed on each node. Additionally, the dependence on the temperature at which the fluid properties are evaluated is tested. Tables 5.1 and 5.2 show the results of the simulations executed at a fixed outlet temperature of 866 K for the 60% $NaNO_3$/40% KNO_3 molten salt mixture. With a salt inlet temperature of 533 K, the simulations examine the extremes of the property evaluation for this specific fluid.

Radiation Nodes	HTF Nodes	$\dot{q}_{inc}$	$\dot{q}_{HTF}$	$\dot{q}_{rad}$	$\dot{q}_{conv}$
		kW	kW	kW	kW
10	10	40,002	34,427	3,280	2,293
10	1	40,002	34,576	3,200	2,225
5	5	40,002	34,433	3,266	2,302
5	1	40,002	34,570	3,194	2,237
2	2	40,002	34,756	2,952	2,292
2	1	40,002	34,896	2,870	2,235
1	1	40,002	34,931	2,773	2,297

Table 5.1: Model sensitivity to the node number for radiation calculations and HTF property evaluation (absolute results in kW for steady-state computations)

Radiation Nodes	HTF Nodes	$\dot{q}_{HTF}$	$\dot{q}_{rad}$	$\dot{q}_{conv}$	$\dot{q}_{HTF}$-Diff.	$\dot{q}_{rad}$-Diff.	$\dot{q}_{conv}$-Diff.
		%	%	%	%	%	%
10	10	86.06	8.20	5.73	0.00	0.00	0.00
10	1	86.44	8.00	5.56	0.43	2.44	2.97
5	5	86.08	8.16	5.75	0.02	0.43	0.39
5	1	86.42	7.98	5.59	0.42	2.62	2.44
2	2	86.89	7.38	5.73	0.96	10.00	0.04
2	1	87.24	7.17	5.59	1.36	12.50	2.53
1	1	87.32	6.93	5.74	1.46	15.46	0.17

Table 5.2: Model sensitivity to the node number for radiation calculation and HTF property evaluation (relative results in percentage of the total incident radiation plus the percentage differences to the 10/10 reference configuration)

The first column indicates the number of radiation nodes used for each panel. The second column indicates how many different fluid temperatures were used for the evaluation of the heat transfer fluid properties for each panel. The tables show that the accuracy of the radiation losses (quantified by $\dot{q}_{rad}$-Diff.), for example, is significantly reduced, when the number of nodes was reduced from 5 to 2 vertical nodes per panel. Using the average HTF temperature between inlet and outlet temperature to evaluate the properties (value in the second column is 1), instead of applying a different fluid temperature at every surface node, also affects the radiation and convection losses. This usually shows in a difference of approximately 2-3% compared to the values where the properties were evaluated at each

radiation node. Although the thermal efficiency of the receiver is only affected by less than 1.5%, the number of surface nodes will be kept as a variable the user of the simulation tool will be able to choose. How the simulation time is affected by the node number is shown for the following yearly simulations.

Instead of a steady solar radiation flux on the receiver, the accumulated thermal energy from solar radiation ($\dot{q}_{inc}$) over the course of a year is shown in the third column of Table 5.3. Columns 4, 5, and 6 show the summation of total energy gain in the HTF ($\dot{q}_{HTF}$), the total radiation ($\dot{q}_{rad}$) and convection heat losses ($\dot{q}_{conv}$).

Radiation Nodes	HTF Nodes	$\dot{q}_{inc}$	$\dot{q}_{HTF}$	$\dot{q}_{rad}$	$\dot{q}_{conv}$
		GJ	GJ	GJ	GJ
10	10	358,624	305,504	26,880	23,873
10	1	358,624	305,725	26,832	23,685
5	5	358,624	305,485	26,841	23,899
5	1	358,624	305,707	26,804	23,713
2	2	358,624	306,830	25,715	23,793
2	1	358,624	307,088	25,656	23,623
1	1	358,624	306,894	25,486	24,063

Table 5.3: Long-term model sensitivity to the node number for radiation calculation and HTF property evaluation (absolute results in GJ for the yearly simulations)

Table 5.4 contains the relative values in percentage of the yearly incident radiation energy and the percentage differences to the results from the simulation utilizing the maximum number of 10 nodes for the surface subdivision and the HTF property evaluation. The last column includes the computation time for each yearly simulation. The CPU time was evaluated with an Intel Core 2 Duo E8500 CPU at 3.16 GHz with 2.96 GB of RAM.

Radiation Nodes	HTF Nodes	$\dot{q}_{HTF}$	$\dot{q}_{rad}$	$\dot{q}_{conv}$	$\dot{q}_{HTF}$-Diff.	$\dot{q}_{rad}$-Diff.	$\dot{q}_{conv}$-Diff.	Timing
		%	%	%	%	%	%	s
10	10	85.19	7.50	6.66	0.00	0.00	0.00	20.98
10	1	85.25	7.48	6.60	0.07	0.18	0.79	13.70
5	5	85.18	7.48	6.66	0.01	0.14	0.11	12.97
5	1	85.24	7.47	6.61	0.07	0.28	0.67	9.89
2	2	85.56	7.17	6.63	0.43	4.33	0.34	9.75
2	1	85.63	7.15	6.59	0.52	4.55	1.05	8.45
1	1	85.58	7.11	6.71	0.45	5.19	0.80	8.97

Table 5.4: Long-term model sensitivity to the node number for radiation calculation and HTF property evaluation (relative results in percentage of the yearly incident radiation energy plus the percentage differences to the 10/10 reference configuration)

Tables 5.3 and 5.4 show similar trends for the deviations compared to the results from the steady state simulations. However, the influence of the different numbers of nodes is much smaller: the maximal differences between the energy gains in the fluid are approximately 0.5% compared to 1.5% in Table 5.2. All relative deviations of the long-term simulations are approximately by a factor of 3 smaller compared to the steady state simulations. Although the accuracy suffers slightly from a reduced number of nodes, the last column in Table 5.4 shows that computational time for the transient simulations decreases with decreasing node numbers.

According to this sensitivity analysis, the code was modified to use 10 radiation nodes and 1 node for the fluid property evaluation. Then, all HTF properties are computed at the mean of the user-specified inlet and outlet temperature. This option shows the highest reduction in computational time with a negligible difference in the total yearly energy gain compared to the 10/10 node option.

5.6.2 Additional Sensitivity Studies

In this section, the influence of the convergence criteria tolerance on the thermal performance and the transient simulation time is investigated. Figure 5.5 shows the influence of convergence criteria tolerances on the annual simulation time and predicted thermal energy gain. The heat transfer calculations are assumed to be converged when the change of the heat transfer fluid mass flow rates within the specified error tolerance as described in Section 5.5. Additionally, the outlet temperature must match the initially specified heat transfer fluid hot temperature. While the real time for the simulation of the typical meteorological year significantly decreases with lower convergence tolerances, a notable difference for the total yearly energy gain does not occur until the tolerance is larger than 1E-03. Based on this study, the simulation is considered as converged when the sums of the temperature and mass flow errors (described in Equations (5.1) and (5.2)) for each separate HTF stream both become smaller than the specified convergence tolerance of 1E-04.

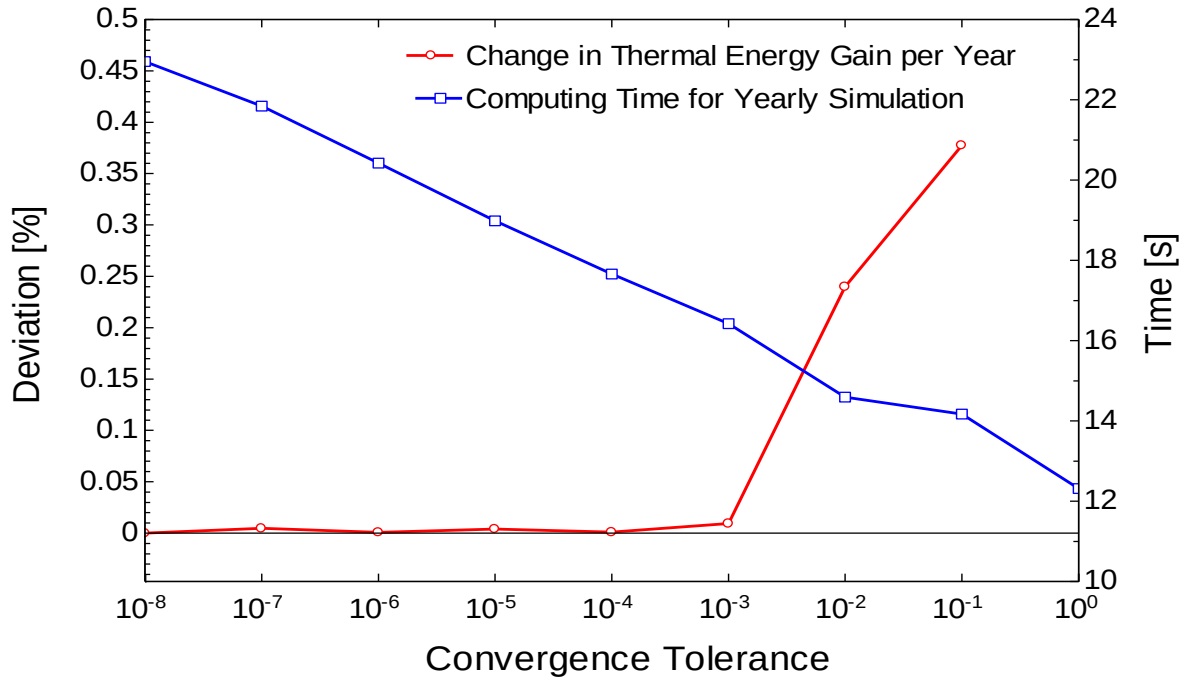

Figure 5.5: Percentage deviation of the yearly thermal energy gain and the transient simulation time as a function of the error tolerance for the iteration convergence.

It was explained in Section 5.4 that before each yearly simulation, the view factors between vertical wall nodes and the horizontal bottom and top surfaces are calculated employing the Monte-Carlo ray tracing technique. In case of 10 nodes per receiver panel, the total number of surfaces is 44: 4 panels with 10 nodes each, the top and bottom surface, the upper lip and the aperture surface. This requires 84 view factors. Most of them can be easily determined through symmetry and reciprocity. In total, the code computes 24 view factors. Since the Monte-Carlo method is a statistical technique, its accuracy is dependent on the number of rays that are used for each view factor computation. Larger number of rays also increases the computational time. Figure 5.6 shows the simulation time required during of the first call to compute all 24 view factors as a function of the totally emitted number of rays per view factor. The accuracy was neglected because in the shown range it only affected the totally absorbed thermal energy by a maximum of 0.01%. According to this analysis, a number of 100000 emitted rays per view factor computation is fixed in the code. Note that the time consumption for this computation is only a minor issue because it is only performed once at the beginning of each transient simulation.

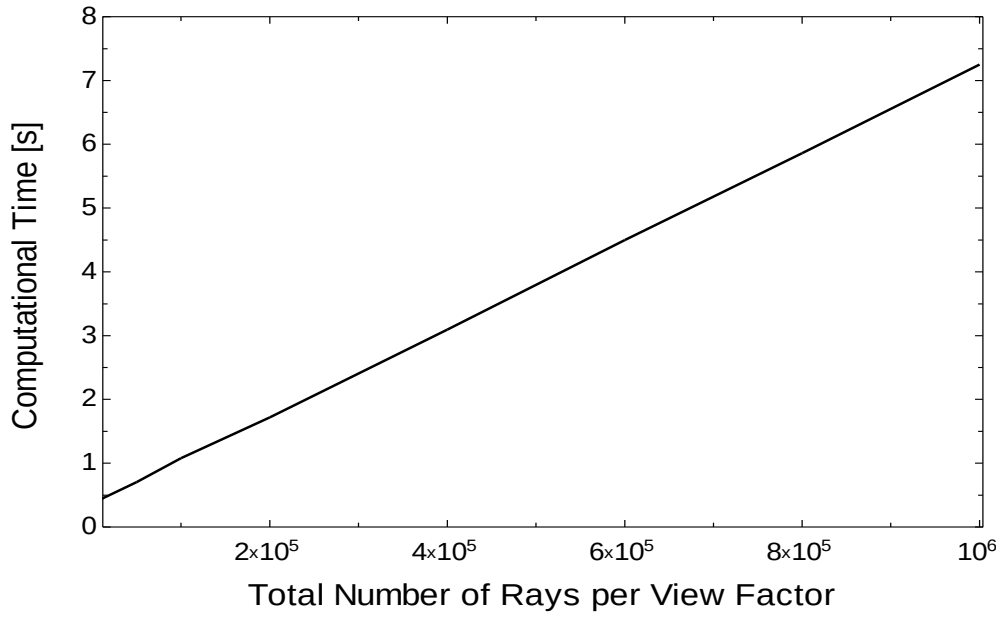

Figure 5.6: Total first simulation call computational time over the total number of rays per view factor calculation with a total of 24 view factors.

The radiation losses are calculated as the portion of the re-emitted radiation from the interior cavity walls that "hits" the aperture surface. This heat loss rate is also a function of the specified aperture temperature. Depending on the position in the cavity, the specific part "sees" the ground that surrounds the tower through aperture or the sky. Therefore, it is assumed that specifying either the ground temperature or the sky temperature for the entire aperture will show the extremes for the influence of this boundary condition. The ground temperature is approximated with the ambient temperature. A yearly simulation with TMY2 data from Daggett, California showed that this parameter affects the total thermal energy absorbed by the fluid over the year by only 0.011%. In the program code, the aperture was specified to be at sky temperature for the radiation exchange because it is usually a few degrees lower that the ambient temperature and therefore a conservative estimate. With Equation (5.9), which can be found in Duffie and Beckman (2006), the sky temperature T_{sky} is calculated as a function of the ambient temperature T_{amb}, the dew point temperature T_{dp}, and the hour of the day. All three inputs are provided by the TMY data table.

$$T_{sky} = T_{amb}(0.711 + 0.0056\,T_{dp} + 0.000073\,T_{dp}^2 + 0.013\cos\left(\left(\frac{180 - 15\,hour}{180}\right)\pi\right)^{\frac{1}{4}} \quad (5.9)$$

The TRNSYS cavity-type receiver model is completed after implementing all required components of the program presented in this chapter. The Fortran code for the component is provided in the digital supplement as described in Appendix D.

⇗6 CFD vs. TRNSYS Model Comparison

The cavity receiver model described in Chapters 2 through 5 has been implemented into TRNSYS and carefully checked for internal consistency. However, the literature does not offer sufficient data for a complete validation of the model against measurements obtained from a real cavity receiver. Clifford K. Ho and Siri Sahib S. Khalsa (C.K. Ho & S.S.S. Khalsa, personal communication, 2009) provided results from CFD simulations conducted for a variety of cavity receiver configurations developed in an effort to benchmark the present model. The 3D simulations were conducted with Fluent (Fluent Inc., 2009) – a computational fluid dynamics program. Using Fluent, the radiation exchange for the receiver surfaces was calculated with the surface-to-surface view factor method and the flow fields, due to free convection, were computed with a k-epsilon turbulence model in Fluent using the standard wall functions for the near wall resolution. It must be clarified that the generation of Fluent results are not part of the present thesis. The Fluent results were prepared independently by Ho and Khalsa for the purpose of comparison with the present model. Thus, the author cannot take credit or responsibility for the accuracy of the CFD results presented here.

6.1 Cavity Receiver Geometry Variations

To account for the influence of different geometries on the thermal losses from the receiver, the receiver configurations are based on the variation of three independent input parameters: aperture area, receiver aspect ratio, and upper lip length. Two different aperture sizes were chosen (large: 200 m^2, small: 50 m^2). The aspect ratio of the receiver is defined by the aperture height to aperture width ratio (H_A/W_A). Aspect ratios of 2 (tall and thin receiver) and 0.75 (short and wide receiver) are considered. Finally, the height of the upper lip was varied from a low value of 1 m to a maximum value of 5 m. Eight different configurations (Table 6.1) were developed with the permutations of these three receiver geometric parameters. Table 6.1 also summarizes the resulting dependent quantities. The definition of

most geometric parameters is described in Section 3.2.1. In addition, the aperture area is the product of aperture width, W_A, and aperture height, H_A. The convective zone is defined by Clausing (1987) as the part of the receiver underneath the shear layer that is defined by the horizontal plane passing through the bottom of the upper lip. Since this model was used for calculating the natural convection from the receiver in the TRNSYS component, the values for the convective zone volume was included in Table 6.1.

Configuration		**1**	**2**	**3**	**4**	**5**	**6**	**7**	**8**
Independent Variables	**Unit**								
Aperture Area	m^2	200	50	200	50	200	50	200	50
H_A/W_A Ratio	-	2	2	2	2	0.75	0.75	0.75	0.75
Lip Height H_L	m	1	1	5	5	1	1	5	5
Angle θ_{rec}	deg	180	180	180	180	180	180	180	180
Dependent Quantities									
Radius R_{rec}	m	5	2.5	5	2.5	8.165	4.082	8.165	4.082
Aperture Height H_A	m	20	10	20	10	12.25	6.124	12.25	6.124
Aperture Width W_A	m	10	5	10	5	16.33	8.165	16.33	8.165
Internal Height H_P	m	21	11	25	15	13.25	7.124	17.25	11.124
Panel Width W_P	m	3.827	1.913	3.827	1.913	6.249	3.125	6.249	3.125
Convective Zone Volume	m^3	707.1	88.39	707.1	88.39	1155	144.3	1155	144.3

Table 6.1: Geometric variations of the cavity receiver model

The eight possible configurations are drawn to scale in Figure 6.1. Configurations 1, 3, 5, and 7 are large because the aperture area was chosen to be four times as big as for the even numbered configurations. Furthermore, the first four configurations show tall and thin shapes because of the aperture width to height ratio of 2 in contrast to the wide and short shapes of configurations 5, 6, 7, and 8. For an increased lip height of 5m, the volume of the lip zone was increased by 4m in height compared to the corresponding configuration with a 1m lip. Note that the angle θ_{rec} was kept constant at 180° to limit the possible number of configurations to 8.

It is understood that most of the shapes probably would not serve well for a realistic receiver construction – the purpose for considering them here is to provide a wide range of configurations for the purpose of comparison with the present model. Starting from the initial receiver geometry of the PS10 tower, the input parameters were chosen to generate rather extreme examples of cavity receiver geometries to examine the influence of geometry on the two loss mechanisms.

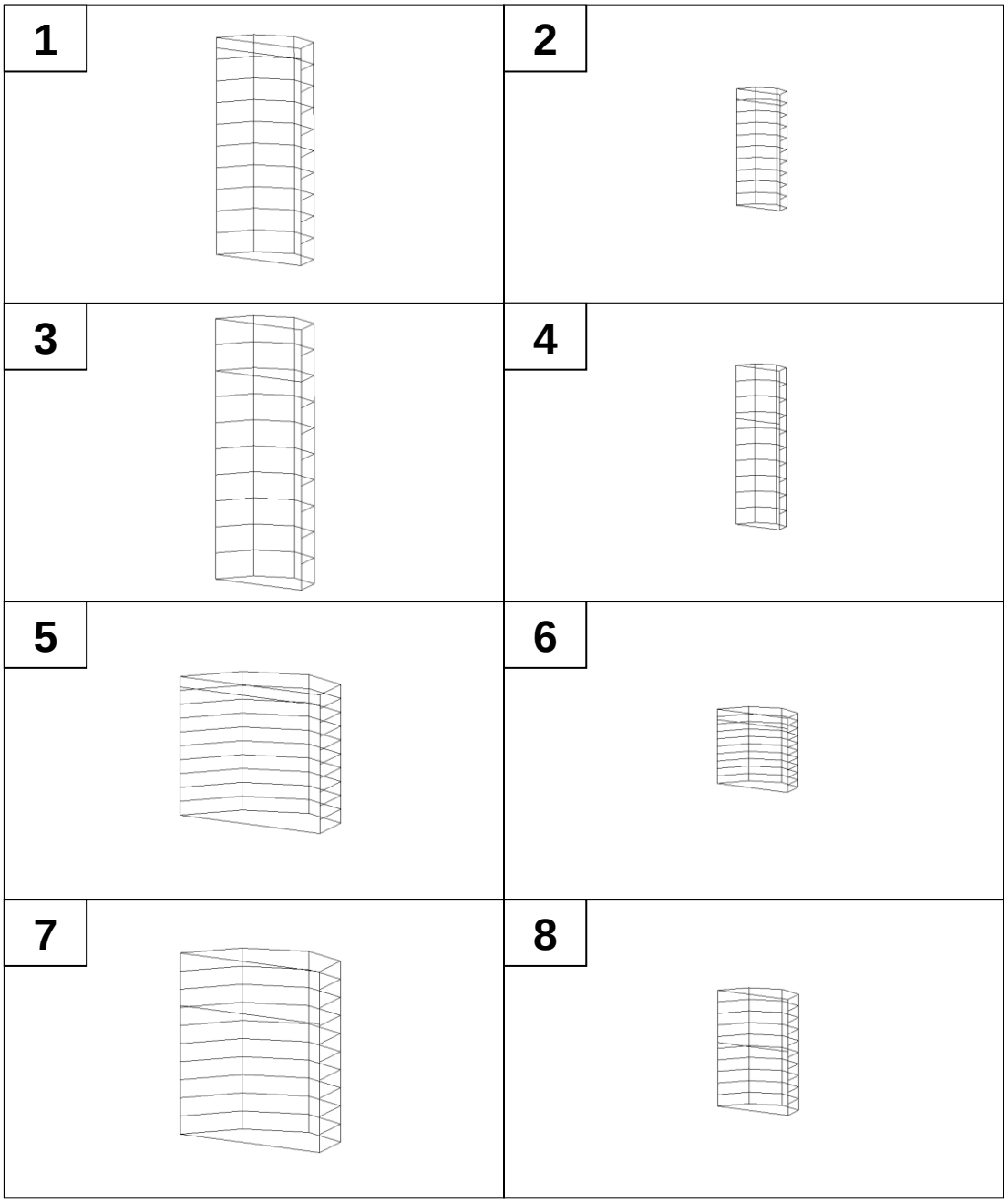

Figure 6.1: Geometric variations of the cavity receiver model showing the vertical division of each panel into 10 subpanels.

6.2 Assumptions and Boundary Conditions

Assuming a "bottom to top" flow distribution of the molten salt in each receiver panel according to flow pattern 1, the TRNSYS cavity receiver component predicts an increasing fluid temperature over the height of the panels. The surface temperatures, which result in heat losses from the receiver to the ambient, are approximately proportional to the fluid temperature.

Modeling the heat transfer fluid flow through the heat exchanger pipes of the panels would be very complex in Fluent. Therefore, the original TRNSYS model of the power tower component was simplified to allow a direct comparison of heat loss estimates predicted by the Fluent model. In the revised TRNSYS model, the complete flow configuration of the heat transfer fluid was neglected, including the piping, temperature dependent flow and heat transfer characteristics and flow direction. Instead, the receiver panels are assumed to be flat surfaces. To enforce realistic surface temperature distributions across the panel height, different convection resistances to an imaginary fluid in the back of the panel were specified at the temperature nodes. The free-stream temperature of the fluid was set to 300 K. To produce a temperature distribution in response to the incoming solar flux that resembles a "bottom to top" flow configuration, the heat transfer coefficients in Figure 6.2 were applied for the 10 temperature nodes. These approximations provide a realistic variation in surface temperatures of the cavity, which are then used for free convection and radiation correlations.

For all configurations, a constant solar flux of 50 MW enters the cavity uniformly and perpendicular to the aperture plane. The ambient temperature was also set to 300 K. The total convection losses from the receiver were calculated neglecting forced convection due to ambient winds. Therefore, a zero velocity field was specified in Fluent.

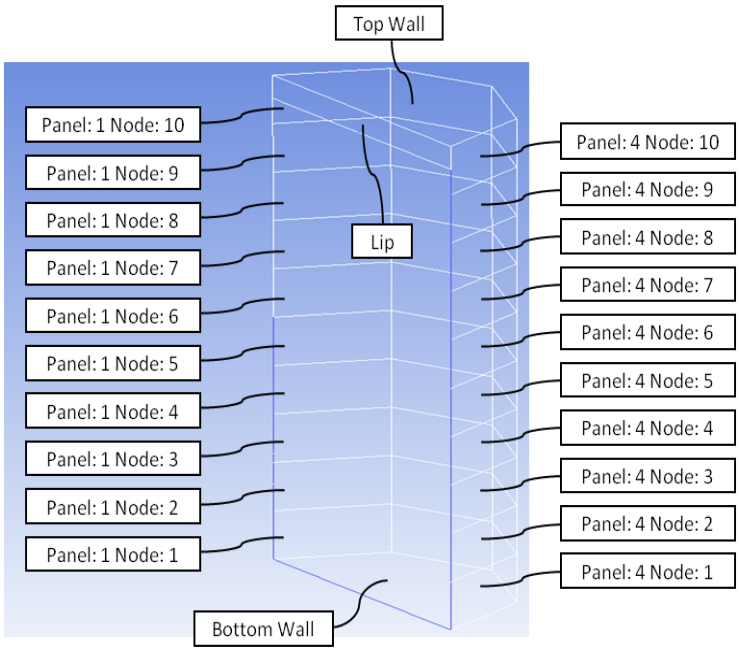

Vertical Panel Node	Heat Transfer Coefficient (W/m^2-K)
10	282
9	303
8	327
7	355
6	388
5	427
4	476
3	538
2	617
1	725

Figure 6.2: Heat transfer coefficient distribution over the vertical nodes of each panel

6.3 Comparison of the Results

The first comparison of the two modeling techniques showed huge differences in the convective heat losses (Figure 6.3) and also the radiation losses (Figure 6.4) did not match very well. In the Fluent simulations, the surface temperatures were determined at a thermal equilibrium for an energy equation that includes radiation heat exchange with the surroundings and two convective heat transfer mechanisms. The first transport term describes the heat transfer to a free-stream at 300 K in the back of the panel. The second mechanism is a convective heat loss to the ambient air. In contrast, the TRNSYS model neglects the influence of the convection to the ambient air on the panel surface temperatures. Convective losses to the ambient air are included in the energy balances, but they are quantified after the panel surface temperatures are determined. The reasons and the verification for this decoupling of the convective losses from the surface node energy balances in the TRNSYS model were explained in Chapter 2.

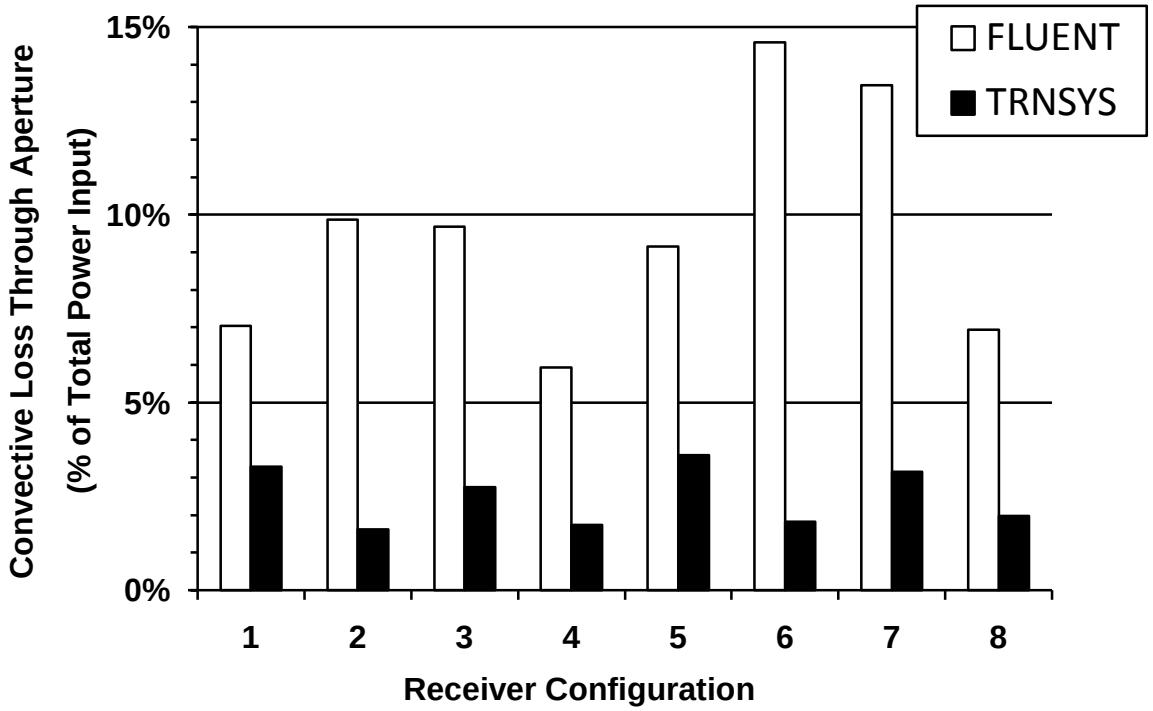

Figure 6.3: Convective heat loss through the aperture in % of the total incoming radiation (50MW).

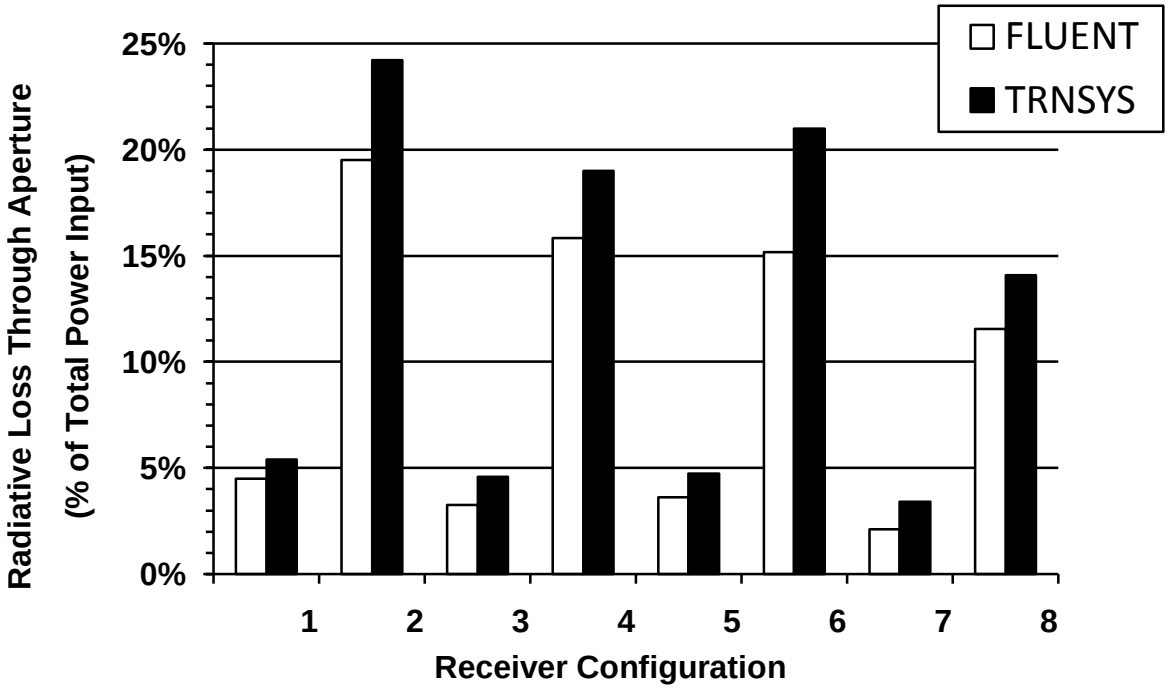

Figure 6.4: Radiation heat loss through the aperture in % of the total incoming radiation (50MW).

Since the Fluent simulations estimated large natural convection loss rates (Figure 6.3), their influence on the surface temperatures are not negligible which causes a reduction of the radiation losses compared to the TRNSYS results (Figure 6.4). In addition, the Fluent simulations were conducted with a panel surface long-wave absorptivity and emissivity of 0.9 compared to the black body radiation in TRNSYS, which likely accounts for a small portion of the differences observed.

The radiation losses show up to almost five times higher values for the small receivers. A constant uniform radiation load of 50 MW was assumed for all configurations. This results in roughly a a factor of two higher surface temperatures for the receiver with half the aperture area as seen in Figure 6.5. Consequently, the radiation loss rate is affected very significantly as it is described proportionally to the fourth power of the surface temperature (Equation (3.2)). Figure 6.5 shows the resulting surface temperatures of an outer panel over the vertical axis from bottom (node 1) to the top (node 10). The surface temperatures of the Fluent simulations are generally lower than the temperatures predicted with TRNSYS which is consistent with the radiation losses described in Figure 6.4.

The temperature profiles show a positive slope up to vertical positions that level the bottom edge of the upper lip. The rise in temperatures is the effect of the linearly distributed coefficients for heat transfer to a free stream at 300 K as specified in Figure 6.2. The upper lip shields the top part of the cavity from the solar flux that enters the aperture perpendicularly, which also explains the sudden temperature drop in that region. Note that this effect would not occur for an active receiver with flow configurations that allows the hot fluid to enter the upper region, which is covered by the lip. Also a realistically distributed flux from a heliostat field that is located below the receiver level contributes to higher temperatures in the top part of the receiver.

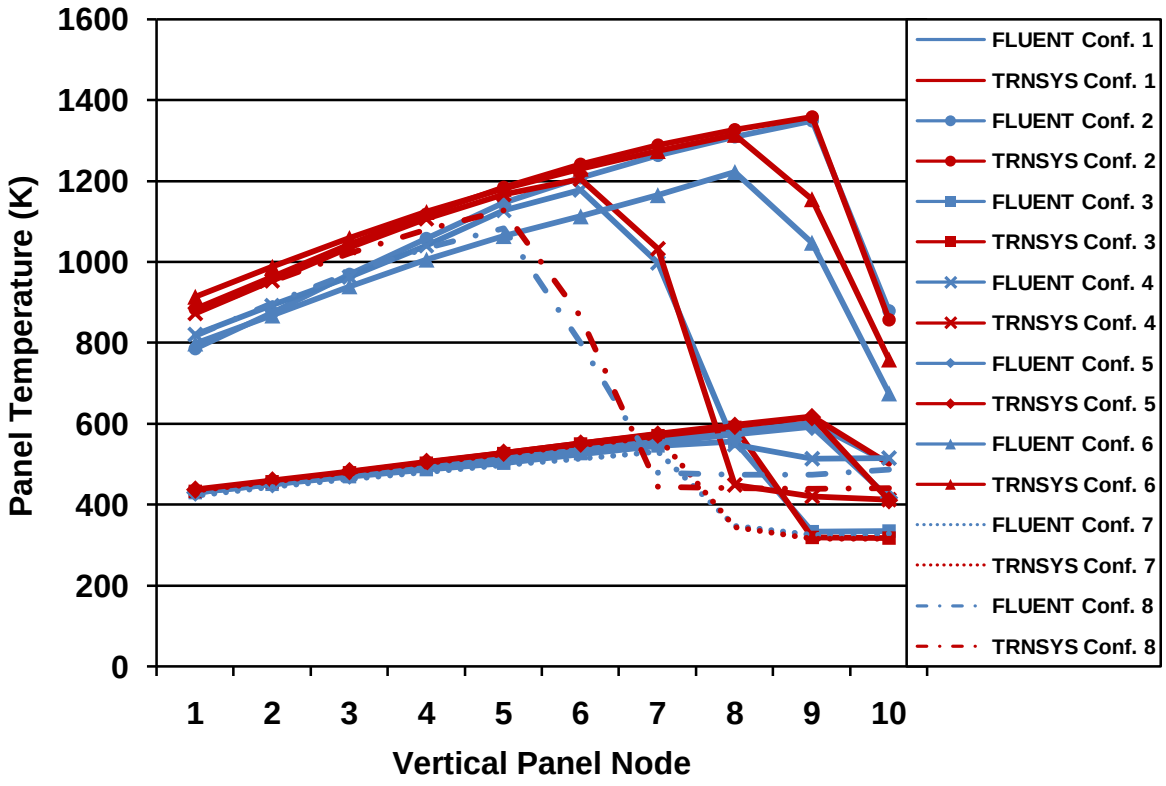

Figure 6.5: Surface temperatures in Kelvin along the vertical axis (10 positions) of an outer receiver panel (Fluent: blue, TRNSYS: red).

Figure 6.6 shows good agreement between the radiation models when both simulations are conducted with the same assumptions (i.e. same energy balance formulation for the surface temperature computation and black body assumptions). The influence of the convection losses on the temperatures was neglected for this simulation set in the CFD method and the TRNSYS calculation. Small deviations (less than 5%) are mostly caused by the comparatively coarse surface temperature discretization of 10 vertical nodes per panel in TRNSYS. Also the numerically computed view factors in Fluent and TRNSYS differ slightly and contribute to the small differences.

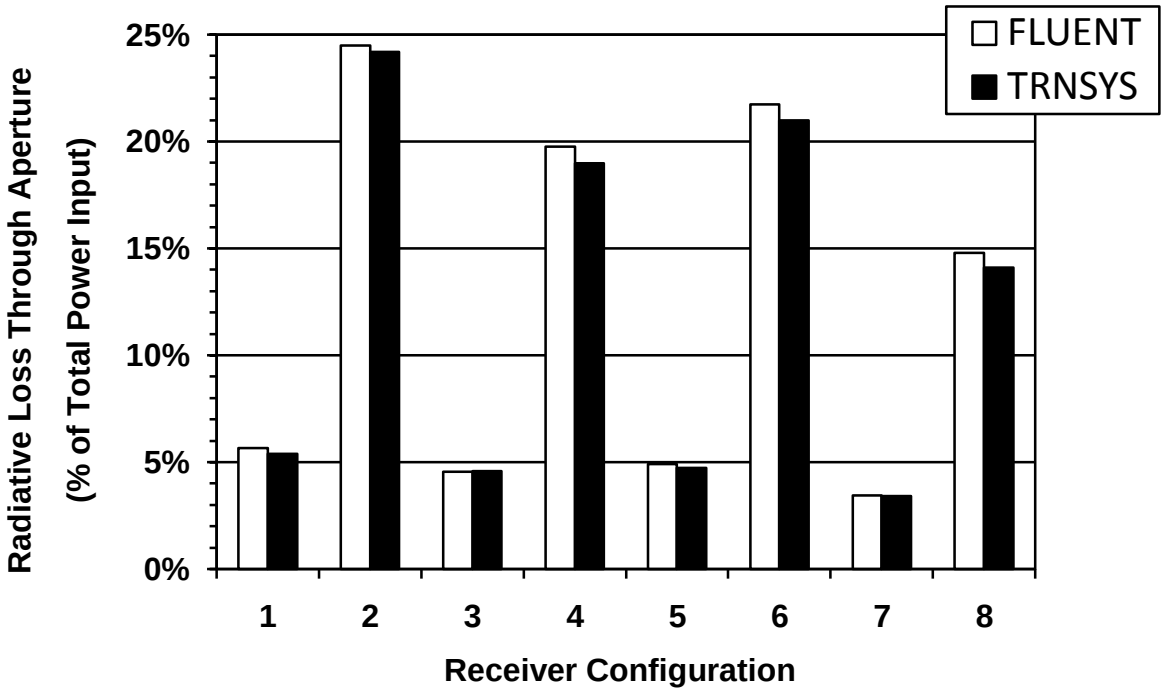

Figure 6.6: Radiative heat loss through the aperture in % of the total incoming radiation (50MW). Natural convection is turned off and the panel absorptivity is set to 1.0.

Further investigation of the natural convection heat losses (Figure 6.3) is necessary due to the huge differences between the Fluent and TRNSYS results. Besides the large absolute differences of the convection loss rates, Figure 6.3 does not show similar trends between the two computation methods of the loss estimates for the eight configurations. The magnitude of the Fluent results shows no direct dependency on the receiver aperture size. Higher losses can be observed for each wide and short configuration ($H_A/W_A = 0.75$) compared to their corresponding tall and thin configuration ($H_A/W_A = 2$). Among shapes with the same aperture aspect ratio, the small receivers (aperture area of 50m2) with a short lip (1m), closely followed by the large shapes (aperture area of 200m2) with a high lip (5m), show the highest convection losses estimated with the CFD method.

In contrast to the CFD results, the TRNSYS model not only computes much lower convective heat losses, but it also shows different tendencies for the eight configurations. The convection losses for the small geometries 2, 4, 6, and 8 are consistently smaller than the

convective heat transfer from the large geometries. Since the total convection losses in TRNSYS are calculated with a function (see Equation (2.16)) that is proportional to both the area of the convective zone (see definition in Chapter 2) and the averaged wall temperature, it is reasonable that the total loss rate decreases when the area is decreased by a factor of 4 while the average surface temperature is only increased by a factor of approximately 2 (Figure 6.5). Additionally, the Clausing convection models were developed for isothermal cavities with a range of wall to ambient temperature ratios from 1 to 3. Figures 2.8 and 2.9 illustrate how the heat transfer coefficient decreases a wall to ambient temperature ratio higher than 2. Regarding the extremely high average surface temperatures above 1000K of the receiver configurations with the small aperture area, the corresponding convection loss results must be neglected because the applied natural convection correlations are not verified for such a temperature range. In the following investigation of the convection losses generated with additional convection correlations, only the odd numbered configurations (1, 3, 5, and 7) with large aperture areas (200 m^2) and reasonable surface temperatures were considered.

6.4 Additional Investigation of the Convection Losses

The TRNSYS model calculates the convection of thermal energy out of the aperture with correlations developed from experiments on cubical cavity receivers (Clausing, 1987). For a comparison, the free convection was also calculated with an older correlation from Clausing (1983) and the Siebers and Kraabel correlation (1984). In addition, the free convection heat loss from a vertical flat plate was investigated by applying two different correlations (Siebers and Kraabel (1984) and Nellis and Klein (2009)). The two natural convection correlations for the vertical flat plate are presented in Section 2.2.3 with Equations (2.22) and (2.23). The flat plate's dimensions are determined by a height equal to the aperture height of the corresponding cavity configuration and a width that results in a surface area equal to the total

interior surface area of the cavity. Figure 6.7 illustrates the geometry of the flat plat and cavity.

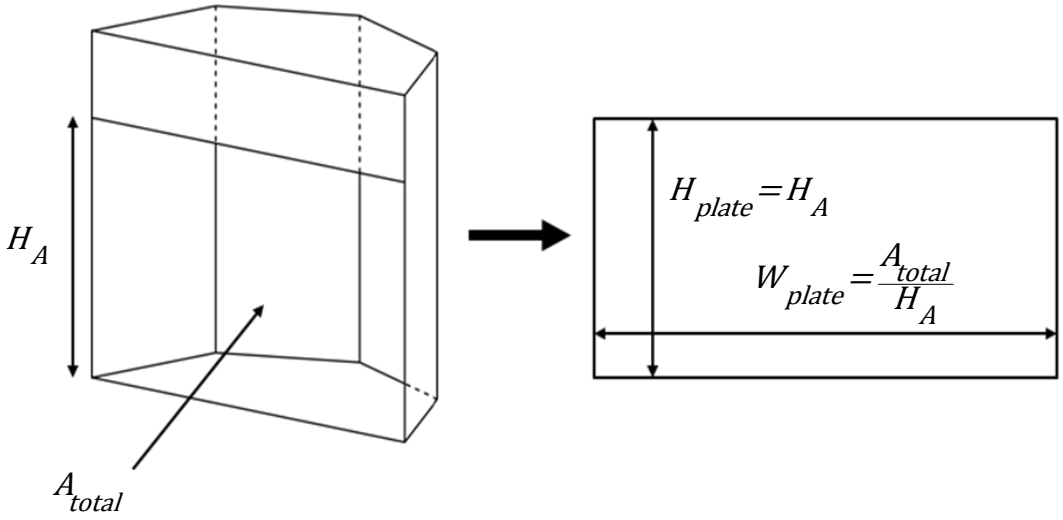

Figure 6.7: Vertical flat plate with the same height as the cavity aperture and the surface of the total interior surface area of the cavity receiver.

The results in Figure 6.8 show the natural convection heat loss results from Fluent compared with the five previously mentioned convection correlations for 4 out of the 8 initial receiver geometric configurations. Receiver configurations 2, 4, 6, and 8 were not considered because their surface temperatures were too high for the applicable range of the heat transfer correlations as explained in the previous section.

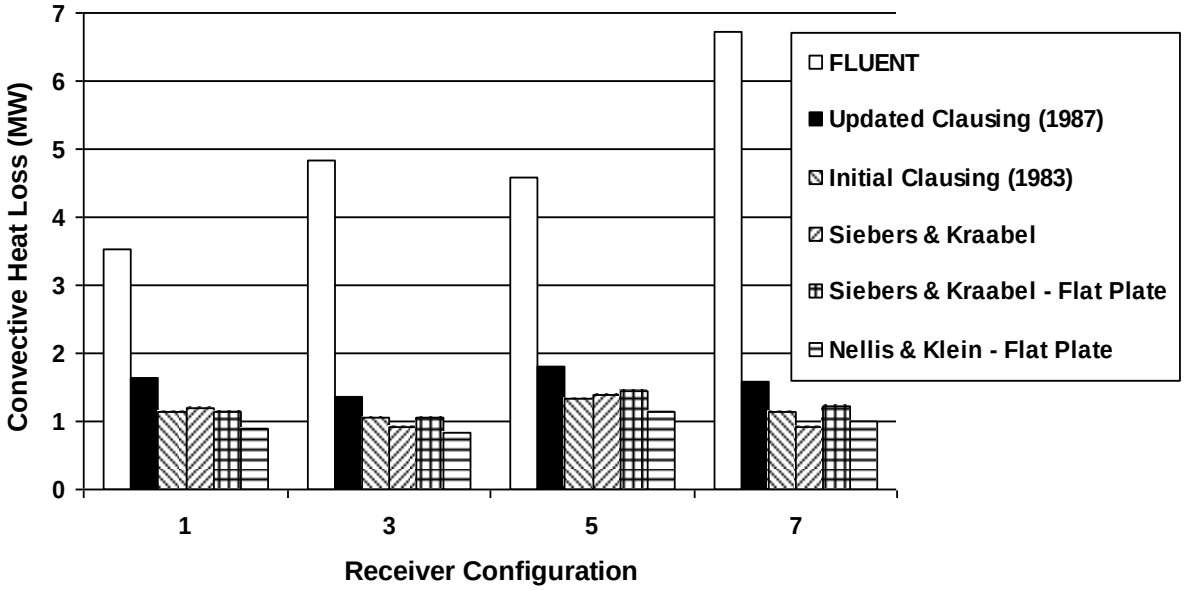

Figure 6.8: Convective heat losses from cavities and flat plates at 4 different configurations.

Figure 6.9 shows the estimates of an averaged heat transfer coefficient for the total losses. The heat transfer coefficient is defined by:

$$h = \frac{\dot{q}_{convection}}{A_{total}(T_w - T_\infty)} \qquad (6.1)$$

A_{total} is the total interior surface area of the corresponding receiver configuration. T_w and T_∞ are the overall averaged wall temperature and the ambient temperature (300K), respectively.

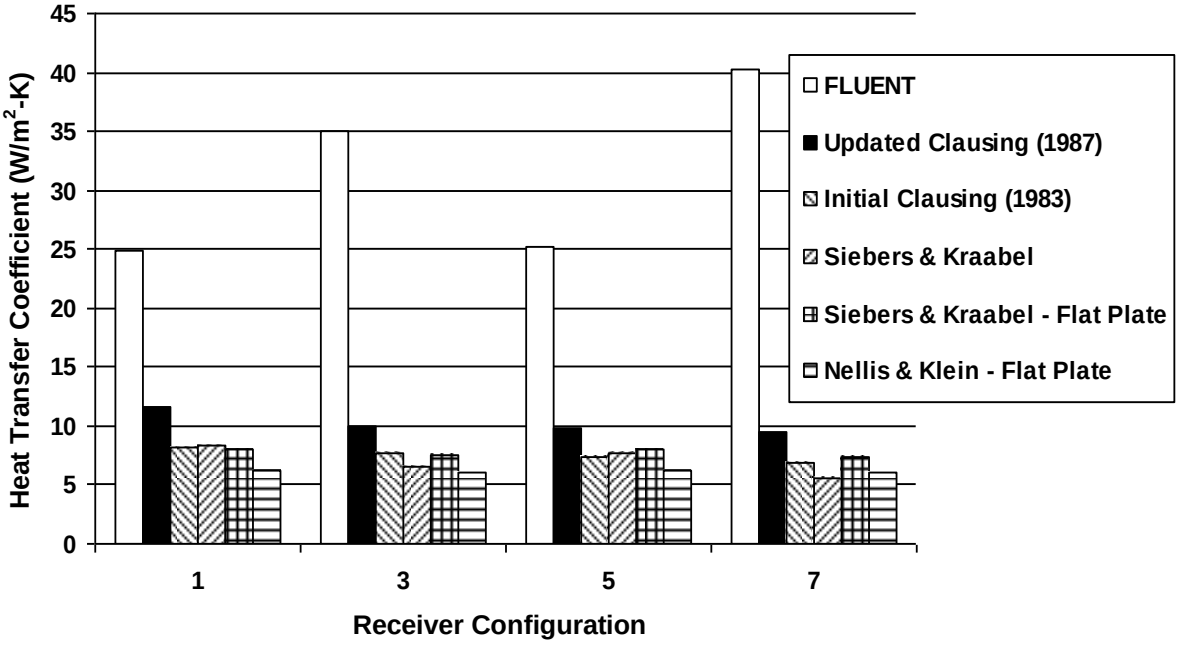

Figure 6.9: Averaged heat transfer coefficients for the total convective energy loss of the large cavity configurations (1, 3, 5, and 7) to the ambient.

The results from Fluent exceed the values obtained with correlations by a factor in the range of approximately 2-4. Note that the experimental correlations were developed in Rayleigh number ranges below 1×10^{12}. The presented receiver configurations (cavities are very large) cause Rayleigh numbers up to 3.5×10^{13} and therefore the correlations should not be applied for accurate results without further validation. However, a rough estimate should be sufficient for this comparison. As expected, cavity and flat plate correlations show results in the similar ranges. Also, the interesting findings in Section 2.2.3 that the flat plate correlations predict lower free convection rates than the cavity correlations are confirmed in Figures 6.8 and 6.9. The updated Clausing model (1987) predicts the highest losses compared to the older Clausing formulation and the Siebers & Kraabel correlation. A check of the average wall temperatures (approximately 550-650K) with the coherence of the heat transfer coefficient and the surface temperatures in Figures 2.8 and 2.9 affirms this difference.

6.5 Conclusions for CFD vs. TRNSYS Comparison

The radiation heat transfer modeling in the CFD simulations and the TRNSYS component produce reasonable results and agree well assuming the same boundary conditions. However, the convection heat losses from the receiver show significant differences between the Fluent simulations and the available correlations found in the literature. Since there has been no verification for the Fluent results and the published correlations agree reasonably well, the convection heat losses for presented cavity-type receiver model will be furthermore estimated with the Clausing model from 1987 since it provides the most conservative estimate compared to the old Clausing model from 1983 and the Siebers & Kraabel correlation. In case very high surface temperatures are expected, the Siebers & Kraabel correlation should be used because it exceeds the Clausing model above surface temperatures larger than approximately 800K to 900K depending on the receiver geometry.

Despite the decision to use the latest Clausing model from 1987 in presented modeling approach of cavity receiver component, the results of the CFD computations demand further investigations on the convection losses via experimental measurements on real receivers and verified CFD simulations that show good agreement to experimental data of basic reference cases.

⇗7 Cavity vs. External Receiver Comparison

7.1 Steady-State Receiver Comparison

To better understand potential performance advantages of cavity receivers, simulations were run using the newly developed cavity-type receiver model and the results compared with a comparably sized external receiver using the model previously developed by Wagner (2008). Because the geometry and therefore some of the model parameters are different for the two receiver types, a number of specific parameters had to be identified as constant in order to obtain a valid comparison. Both towers are assumed to be at a height of 120 m to make the calculated pumping power comparable. Furthermore, the panel area (301.6 m^2), the panel height (12 m) as well as the receiver inlet and outlet temperatures were assumed to be equal. The three cases shown in Table 7.1 resemble the hours 8, 10, and 12 (in solar time) whose azimuth and zenith angles resemble the solar position of a typical day in May. The average incident solar radiation flux ranged from 20-40 MW in 10 MW increments in order to reflect realistic input loads for the corresponding times assuming a typical spring day in Daggett, California. The receiver surfaces for both models are assumed to be black. The solar fluxes are spread over the panel surfaces according to flux map distributions generated with DELSOL3 for the specified solar azimuth and zenith angle. As explained in Chapter 5, the flux distributions are read into the TRNSYS cavity receiver component from the *fluxmap.csv* file based on the solar position.

Case	Receiver Type	Hour	Azimuth (0 = South)	Zenith	Radiation Power	Receiver Diameter	Inlet Temp	Outlet Temp
		hr	deg	deg	MW	m	C	C
1	Cavity	8	-76.59	69.74	20	16.42	290	565
	Cylinder	8	-76.59	69.74	20	8	290	565
2	Cavity	10	-52.66	47.49	30	16.42	290	565
	Cylinder	10	-52.66	47.49	30	8	290	565
3	Cavity	12	-10	33	40	16.42	290	565
	Cylinder	12	-10	33	40	8	290	565

Table 7.1: Input parameters for the cavity-type and the cylindrical receiver models

For each receiver, the coolant flow pattern yielding the highest collection efficiency was chosen. Based on his analysis of the cylindrical receiver design, Wagner showed the maximum efficiency is achieved using flow type no. 2 as shown below in Figure 7.1 (Wagner, 2008). By way of comparison; other flow patterns for the external receiver model analyzed by Wagner are presented in Figure 7.1. Flow types 1 through 4 have two separate flow paths and they are symmetric along the north-south axis. Both fluid inlets are at the same receiver position, while the outlets are on the opposite side of the cylinder. In contrast, the single-flow-path patterns have the fluid inlet and outlet at the same circumferential position of the receiver. It is important to emphasize that the results for these flow patterns are based on northern-positioned heliostat fields.

Wagner (2008) found maximum efficiencies net energy collection is achieved for flow patterns 2 and 4. An analogous reasoning as for the cavity receiver flow study can be applied: the maximum solar flux is on the northern side of the tower. When the fluid travels under comparatively low radiation conditions from the southern inlet to the northern outlet position, the greatest temperature increase occurs close to the outlet due to the high solar flux. Therefore, the overall average temperature of the cylindrical receiver surface is lower when compared to the remaining flow patterns.

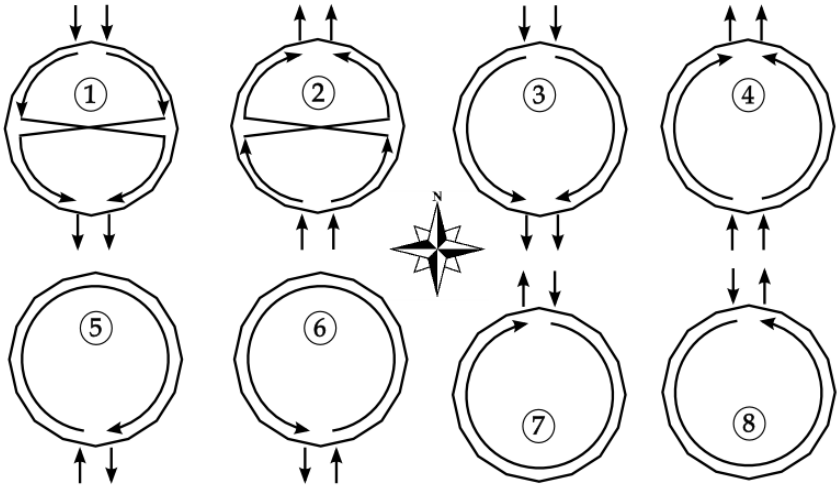

Figure 7.1: Cross-sectional view on the receiver cylinder with eight possible flow configurations (Wagner, 2008).

For the cavity-type receiver, the most efficient flow pattern 6 was chosen. This flow pattern utilizes two separate flow-paths that receive the maximum flux close to the fluid outlets as seen in Figure 7.2.

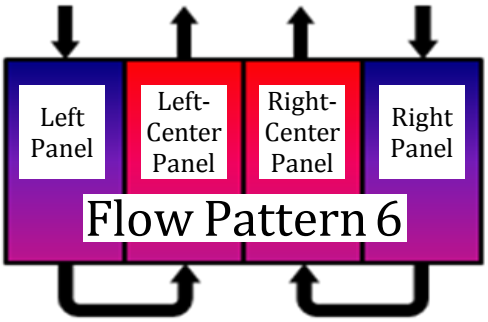

Figure 7.2: Most efficient flow pattern of the cavity-type receiver model. The colors mark the expected temperature gradients (blue: cold, red: hot).

Table 7.2 shows the simulation results for the three different levels of incident radiation. Interestingly, the cylindrical receiver shows a slightly higher thermal efficiency due to smaller convection losses. Note that forced convection due to wind is not considered in either tower model. The effect of the wind on thermal efficiency is likely smaller for the cavity receiver, depending on the wind direction. The thermal efficiency is defined here as the ratio of the energy gain in the heat transfer fluid to the total incoming incident short-wave

radiation. As expected, the radiation losses are lower for the cavity-type receiver due to its enclosure geometry.

Case	Receiver Type	HTF Flow Rate	Thermal Efficiency	Pump Power	Convection Loss	Radiation Loss	Thermal Power	Power Before Losses
		metric tons/hr	-	MW	MW	MW	MW	MW
1	Cavity	138.26	0.7953	0.057	1.953	2.142	15.906	20.00
	Cylinder	139.66	0.8031	0.057	0.741	3.197	16.067	20.00
2	Cavity	224.70	0.8591	0.090	1.968	2.182	25.849	30.00
	Cylinder	226.09	0.8669	0.093	0.746	3.244	26.010	30.00
3	Cavity	311.02	0.8944	0.128	1.988	2.235	35.780	40.00
	Cylinder	312.67	0.8992	0.130	0.751	3.282	35.970	40.00

Table 7.2: Absolute results of the comparison between the cavity-type and cylindrical receiver

Table 7.3 contains the percentage differences between the cavity vs. cylindrical receiver results in Table 7.2.

Case	HTF Flow Rate	Thermal Efficiency	Pump Power	Convection Loss	Radiation Loss	Thermal Power
1	1.01%	0.98%	1.22%	90.01%	39.54%	1.01%
2	0.62%	0.90%	3.23%	90.04%	39.12%	0.62%
3	0.53%	0.54%	1.67%	90.38%	37.96%	0.53%

Table 7.3: Percentage differences between the results for the cavity and the cylindrical receiver in Table 7.2

Assuming that the diameters for the cylindrical receiver are large and the cylindrical shape is approximated by the arrangement of rectangular panels, the convection losses in the external receiver model (Wagner, 2008) are computed with the Siebers & Kraabel (1984) natural convection correlation that was developed with experiments on vertical flat plates. This correlation was included in the earlier convection comparisons in Chapter 2 and 6.

Table 7.1 reports 90% higher convection heat losses from the cavity than from the external receiver. Previous computations in Chapter 2 and 6 also showed higher losses for cavities

than for flat plate correlations (Siebers and Kraabel, 1984) (compare Figure 2.4, Figures 6.8 and 6.9), but the difference was not as significant. The much higher difference between the two correlations in the current case results from different area definitions compared to the computations in Chapter 2 and 6. Since an equal active surface area was specified for the comparison between the external cylindrical and cavity-type receivers in the present case, the cavity has a larger total interior area than the cylinder. The cavity receiver because it has an additional heated interior surface due to the bottom, top and lip surfaces. Bottom, top and lip surfaces are assumed to be inactive, but they participate in radiation exchange inside the cavity and thus increase the convection heat transfer from the cavity. In summary, the previous comparisons, the correlations were compared by setting the total interior cavity area (including bottom, top and lip surfaces) equal to the flat plate/cylinder surface area as opposed to defining equal active areas (i.e. only the vertical back panels in the cavity, but the total circumferential area for the cyclinder) in the current case. In conclusion, the totally heated surface area, which proportionally influences the convection loss rate, is larger for the cavity (bottom and top surfaces act like heated fins) than for the cylinder.

For the comparison shown above, the cavity is assumed to have an upper lip with a height of 3 m and a receiver angle (θ_{rec}, defined in Section 3.2.1.2) of 180°. A larger lip decreases the convection (Figure 2.7) and radiation losses. The effect of the receiver angle on the thermal efficiency is shown in Figure 7.3. To keep the panel surface area and the panel height constant at 301.6 m^2 and 12 m, respectively, the receiver radius was varied for different receiver angles. Instead of a steady state simulation with constant flux, the thermal efficiency is averaged over a yearly simulation with TMY2 weather data from Daggett, California.

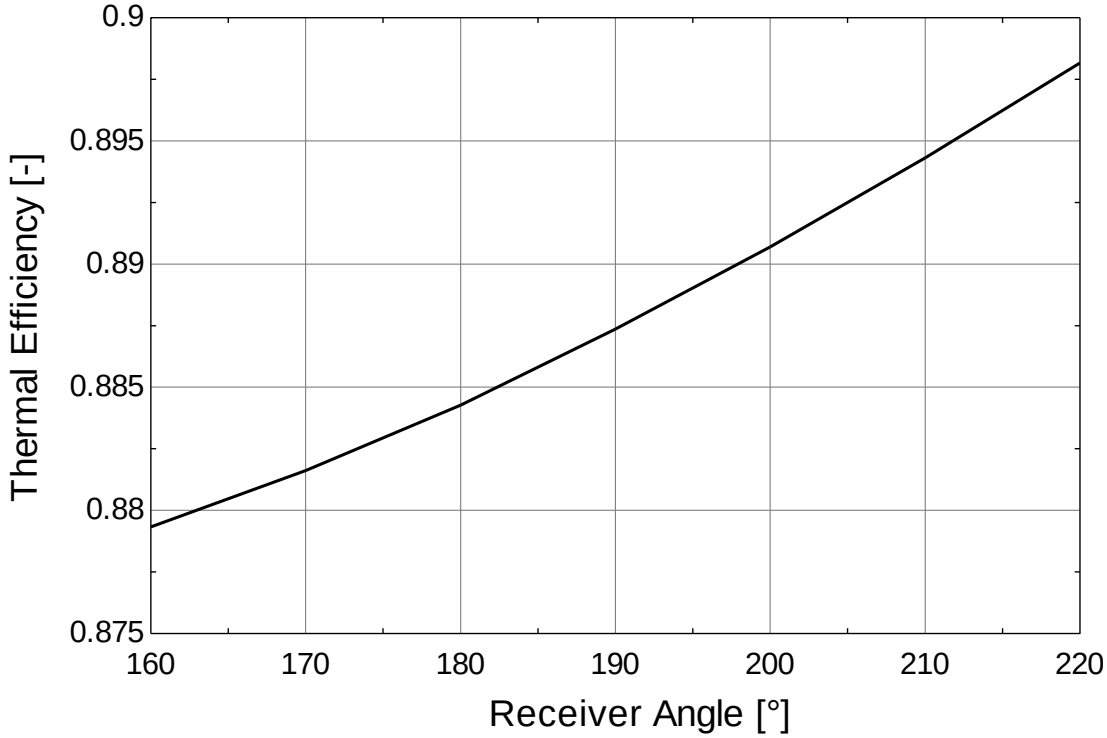

Figure 7.3: Annual averaged thermal receiver efficiency as a function of the receiver angle

As for the lip effect, the increasing efficiency with a larger receiver angle can be easily explained with the decrease of the aperture area, which leads to lower total heat losses to the ambient. One has to consider for the real application, that it might not be able to distribute the solar flux equally well for smaller aperture areas (larger lip or larger receiver angle) as for larger aperture areas where the heliostats can be easily focused on different parts of the panel area.

7.2 Transient Plant Analysis

7.2.1 Plant Design with PTGen

To examine the comparative performance for both the cavity-type and cylindrical-type receivers, in the context of a complete power plant analysis, transient solar tower power plant analyses were conducted over an annual period with under varying plant operating conditions. The respective heliostat fields and tower designs were optimized using Wagner's (2008) PTGen program and the DELSOL3 code (Kistler, 1986). Both plants were specified to generate 30 MW (nominal) of electrical power. The input data for the PTGen optimization are presented in Table 7.4. The components of the power plants that generate the thermal energy (i.e. heliostats and receiver) are oversized by a factor of 2. This allows the power block to generate the nominally desired electricity output of 30 MW for an extended period of time, which is twice as long as the operational periods of the heliostat field and the receiver. For an ideal case, where the sun shines 12 hours every day in the year with a constant insolation, the receiver would generate enough thermal energy to drive the steam cycle for 24 hours each day. The excess thermal energy in the hot salt that is not directly fed to the power cycle is stored in a large tank. However, this scenario is not realistic because the radiation periods are much shorter in the winter such that the received thermal energy is too small for continuous electricity generation at the desired level. On the other hand, during the summer not all available solar energy can be utilized because of limited storage capacities. In the presented comparison, the system oversize factor was arbitrarily chosen as 2 to allow for electricity generation at peak load periods in the evening.

Equally sized heliostats with default values from DELSOL for the cant panels and the surface properties are specified for both power towers. Two parameters can be specified for the cylindrical receiver design: receiver diameter and panel height; the cavity receiver requires more variables: aperture height and width, the radius of the semi-cylindrical absorber surface, the azimuth and zenith angle for the orientation of the aperture and the structure width. All specified values for the receivers are guess values that will be optimized by the DELSOL

code. Furthermore, a receiver surface absorptivity of 1.0 and a flux limit of 1.5 MW/m^2 were assumed. The tower height is also optimized by the DELSOL code.

Table 7.5 summarizes the optimization results. These values, the generated flux maps, and field efficiency files are used as inputs for the power plant analysis in TRNSYS as explained in the following section. During the plant analysis, it was found that the total incident solar power onto the receiver onto the absorber panels is much lower for the cavity receiver than for the external receiver. This difference is mainly caused by different average flux levels in the flux maps. The assumptions and settings in the PTGen/DELSOL that cause the code to generate different solar loads depending on the receiver type requires a careful check of the programs. The further receiver comparisons were conducted by manually scaling of the flux maps to equal average flux values manually.

External Receiver Plant			Cavity Receiver Plant		
Parameter	**Value**	**Units**	**Parameter**	**Value**	**Units**
System Sizing			*System Sizing*		
Desired electric power output (fixed	30.0	MW	Desired electric power output (fixed	30.0	MW
Solar multiple / system oversize	2.0	-	Solar multiple / system oversize	2.0	-
Heliostat Field			*Heliostat Field*		
Total heliostat height	10.0	m	Total heliostat height	10.0	m
Total heliostat width	10.0	m	Total heliostat width	10.0	m
No. of vertical cant panels (default)	8	-	No. of vertical cant panels (default)	8	-
No. of horizontal cant panels (default)	2	-	No. of horizontal cant panels (default)	2	-
Panel width (default)	4.88	m	Panel width (default)	4.88	m
Panel height (default)	1.22	m	Panel height (default)	1.22	m
Mirror reflectivity (default)	0.91	-	Mirror reflectivity (default)	0.91	-
Receiver			*Receiver*		
Receiver type	Externa		Receiver type	Cavity	
Panel height (guess value)	10	m	Aperture height (optimize value)	10	m
Receiver diameter (guess value)	10	m	Aperture width (optimize value)	10	m
			Cavity Radius (optimize value)	10	m
			Receiver zenith (optimize value)	90	deg
			Receiver azimuth (optimize value)	180	deg
			Structure width (optimize value)	20	m
Receiver absorptivity	1.0		Receiver absorptivity	1.0	
Maximum flux	1500	kW/m^2	Maximum flux	1500	kW/m
Tower height (guess value)	100	m	Tower height (guess value)	100	m

Table 7.4: Input values for the plant optimization with PTGen for the external (cylindrical) receiver and the cavity-type receiver plant.

External Receiver Plant			Cavity Receiver Plant		
Parameter	**Value**	**Units**	**Parameter**	**Value**	**Units**
Number of heliostats	2890	-	Number of heliostats	2711	-
Size of each heliostat	97	m^2	Size of each heliostat	97	m^2
Total mirror surface area	280330	m^2	Total mirror surface area	262967	m^2
Receiver panel height	9.6	m	Receiver panel height	10.56	m
Receiver width/diameter	8	m	Aperture height	9.6	m
			Aperture width	16	m
			Cavity radius	8	m
Tower height	140	m	Tower height	140	m

Table 7.5: Optimization output values from PTGen/DELSOL for the plant design

7.2.2 TRNSYS Solar Power Tower Analysis

The weather input for the plant simulations was provided in form of the TMY2 data format with local information from Daggett, California. Both, the cavity-type receiver and the external receiver plant, apply the 60 wt% NaNO3 and 40 wt% KNO3 molten salt mixture that was used in the Solar Two project (Pacheco, 2002) as the receiver coolant and the thermal storage medium. The hot fluid is stored in a large tank that serves as a thermal energy reservoir for the power cycle. Another storage tank of the same size stores the cold fluid that leaves the power cycle heat exchanger and feeds the receiver. Except for the central receiver system, both plants use exactly the same component setup in TRNSYS: the heliostat field (Type221) reads the flux map file *fluxmap.csv* and the efficiency array *eff_array.dat*, the receiver component (Type222/230), the hot and cold storage tanks (Type39), the Rankine cycle (Type224), and the tower logic component (Type223). The inputs and parameters for every component are listed in Appendix C. The TRNSYS component setup is illustrated in Figure 7.1.

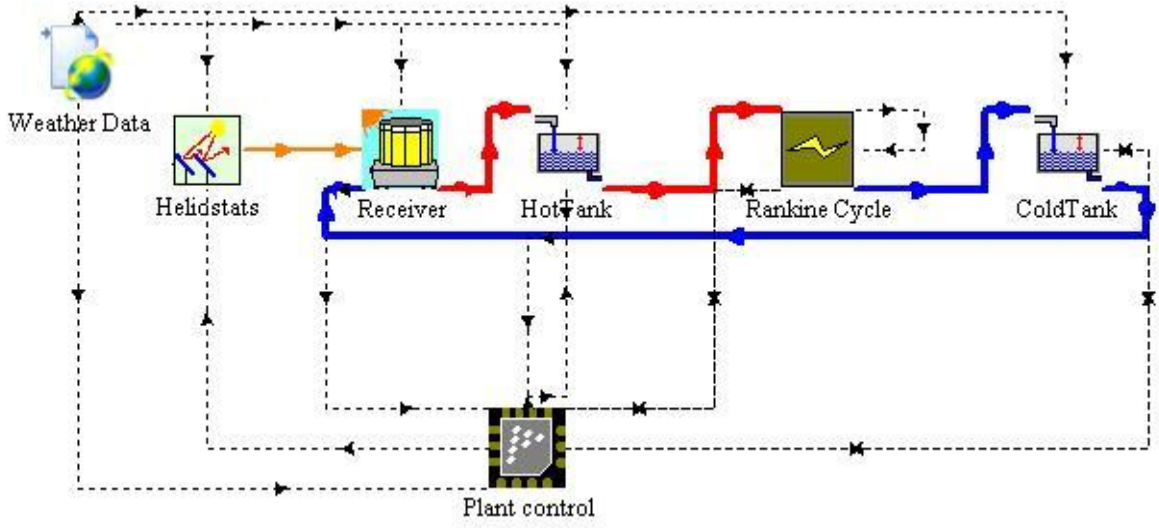

Figure 7.4: Plant setup for the cylindrical/cavity-type receiver power plants (cylindrical receiver is shown). Red/blue connections symbolize the hot/cold molten salt flow path.

With the output information from the PTGen optimization, the receiver design, the heliostat field efficiency and the flux distribution are provided depending on the solar position. Both plants were designed for a nominal electrical output of 30 MW. Since the simulations in Section 7.1 revealed that the cylindrical and cavity receiver operate with similar efficiencies according to the TRNSYS models, it is expected that the total solar flux from the heliostat field is similar as well as long as the same weather data, specifically the direct normal irradiation, is provided. In contrast, the simulations showed that the yearly accumulated radiation onto the cavity receiver is approximately 20% lower than that onto the external receiver when the originally generated flux maps by PTGen/DELSOL3 are used for the annual simulations. As reported in Section 7.2.1, the DELSOL3 code in combination with the PTGen program generates significantly different solar loads for cavity receivers than for the external receiver assuming equal desired plant electricity outputs, although the receiver efficiencies are comparable. The settings and assumptions in PTGen and DELSOL have to be investigated to resolve this problem.

In order to conduct the simulations for both plants assuming equal total energy inputs, the flux maps were scaled such that the total yearly solar energy radiated onto the receiver surface is equal. A negligible difference of 0.05% is due to numerical errors in the flux map

scaling and different incident radiation computation methods in both receiver models. In addition, the plant control component (Type223) checks the storage tank volumes and if the hot receiver tank reaches its maximum fluid volume, the heliostat field is defocused from the receiver. This situation can occur at different times for the two plant types if the receiver efficiencies are not equal. Therefore, the different hours at different flux levels that were removed from the solar load on the receiver cause small differences in the total annual solar radiation on the receiver. Scaling the flux maps to an equal average flux onto the receiver also requires the receivers have equal surface areas as the total radiation is calculated with Equation :

$$\dot{q}_{solar,total} = A_{rec}\, \dot{q}''_{inc} \tag{7.1}$$

where A_{rec} is the total absorber surface and the average flux incident on the receiver is $\dot{q}''_{inc}$. The diameter of the external receiver was adjusted from 8 m (Table 7.5) to 7.796 m and the panel height from 9.6 m to 10.56 m such that the active surface areas for both receivers are 258.6 m^2. The remaining geometric quantities were unchanged as presented in Table 7.5. Furthermore, the inlet and outlet HTF temperatures were set to 290K and 565K, respectively, for both plants. The cavity receiver is assumed to be at a receiver angle of 180° due north, which is consistent with the standard assumptions in DELSOL3.

As mentioned in Chapter 2, the literature does not provide adequate models for forced convection from large-scale cavity-type receivers depending on wind speed and direction, although Clausing (1983) claims that the internal heat transfer resistances of the cavity are dominant for the convective heat losses. Therefore, wind would only have a significant influence on the losses if it enters the cavity (depending on direction) and reduces the heat transfer resistances from the wall to the internal bulk flow. In conclusion, the forced convection will likely have a much smaller influence on the total convection for the cavity than for the completely exposed, external cylinder. The cylindrical receiver model, however, utilizes forced convection correlations that were presented in Siebers & Kraabel (1984). To include the effect of wind in the simulations, the simulations for the external receiver were

conducted: first, assuming constantly zero wind speed and; second, assuming the wind velocities provided in the weather data. The results are summarized in Table 7.6.

Receiver Type	Thermal Efficiency	Pump Energy	Convection Loss	Radiation Loss	Thermal Energy	Energy Before Losses	Electric Energy Output
	-	GJ	GJ	GJ	GJ	GJ	GJ
Cavity (no wind)	0.954	6.87E+03	3.270E+04	3.850E+04	1.476E+06	1.547E+06	5.193E+05
External (no wind)	0.955	4.45E+03	1.040E+04	5.899E+04	1.476E+06	1.546E+06	5.183E+05
External (wind)	0.952	4.45E+03	1.496E+04	5.890E+04	1.474E+06	1.548E+06	5.176E+05

Table 7.6: Yearly simulation results from cavity-type and external CRS systems.

Comparison	Thermal Efficiency	Pump Energy	Convection Loss	Radiation Loss	Thermal Energy	Energy Before Losses	Electric Energy Output
	%	%	%	%	%	%	%
Cavity (no wind) External (no	0.119	42.62	103.5	42.03	0.043	0.077	0.185
Cavity (no wind) External (wind)	0.178	42.79	74.46	41.88	0.128	0.049	0.331
External (wind) External (no	0.297	0.177	35.96	0.154	0.171	0.126	0.146

Table 7.7: Percentage differences between results of the three simulation runs in Table 7.3

The values in Table 7.7 show the percentage differences between the cavity and the external receiver simulations results given in Table 7.6. It can be observed that the total yearly efficiencies show smaller relative differences compared with those from the steady state analysis in Table 7.1. One reason is the higher efficiency of approximately 95% compared to 90% for case 3 (40 MW) in Table 7.2, which results in a smaller influence of differences in the losses on the total efficiency. The differences in convection and radiation heat losses between the cavity and the cylindrical receiver are both higher because of a slightly different geometry for the cavity, specifically the lip. The lip for the transient simulation was defined

by the DELSOL code as 0.96 m compared to the larger lip (3 m) that was used in the steady-state simulations.

Due to a difference in tower height of 40 m, the cavity receiver requires approximately 40% more pumping energy than the lower external receiver. The required tower heights were estimated with DELSOL. In the last column of Table 7.6, the total yearly incident radiation on the receiver shows not only small differences between the cavity and the external receiver plant as described before, but also a difference of 0.126% is noted between both external receiver simulation runs (wind/no wind). This difference is mainly due to the previously mentioned defocus signal from the control logic.

Figure 7.2 shows the fluid volumes in the storage tanks over the annual simulation. Both storage tanks have a total volume of 15000 m^3 and they begin the year with 7500 m^3 of fluid loaded (initial condition). During periods of the year with days are shorter and incident radiation is lower, the solar tower cannot constantly provide enough thermal energy to operate the Rankine cycle with the specified period of 15 hours (8 am till 23 pm) at 30 MW each day. Therefore, the hot tank is depleted very quickly during plant operation. In contrast, during the summer months in the middle of the year the hot tank is usually filled up to the maximum volume after each tower operation period. If the hot fluid tank is full before the daily period of solar radiation is over, the heliostats are defocused and the additional daily radiation must be neglected.

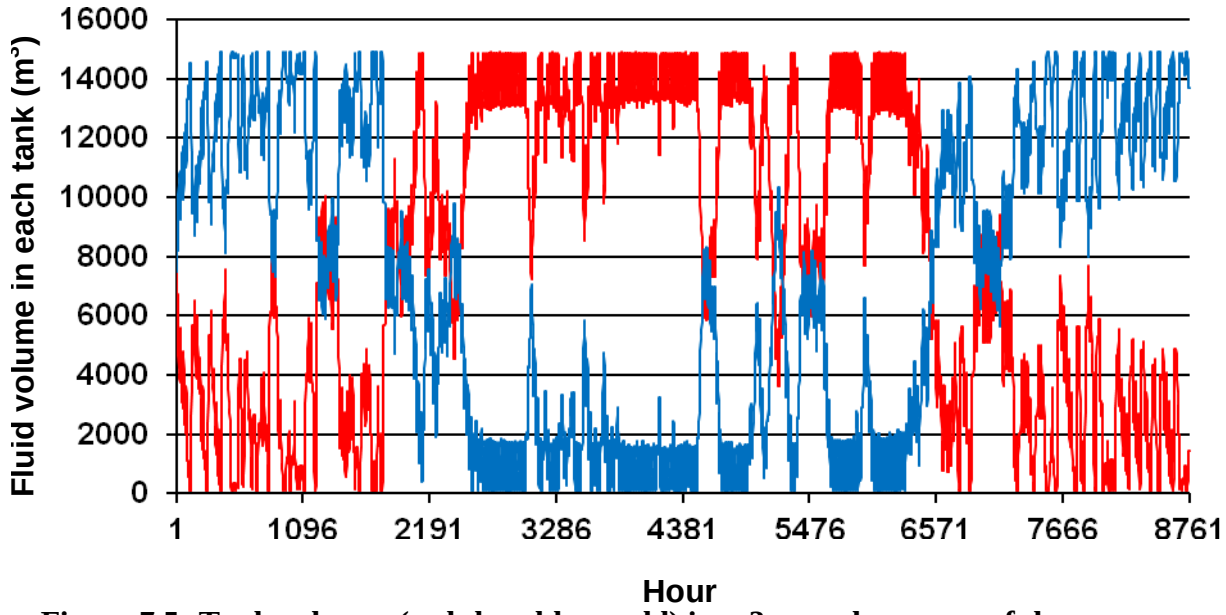

Figure 7.5: Tank volumes (red: hot, blue: cold) in m3 over the course of the year.

The daily plant operation periods are exemplified showing the thermal energy output of the receiver and the electricity output of the power cycle for six days in January (Figure 7.3) and six days in July (Figure 7.4).

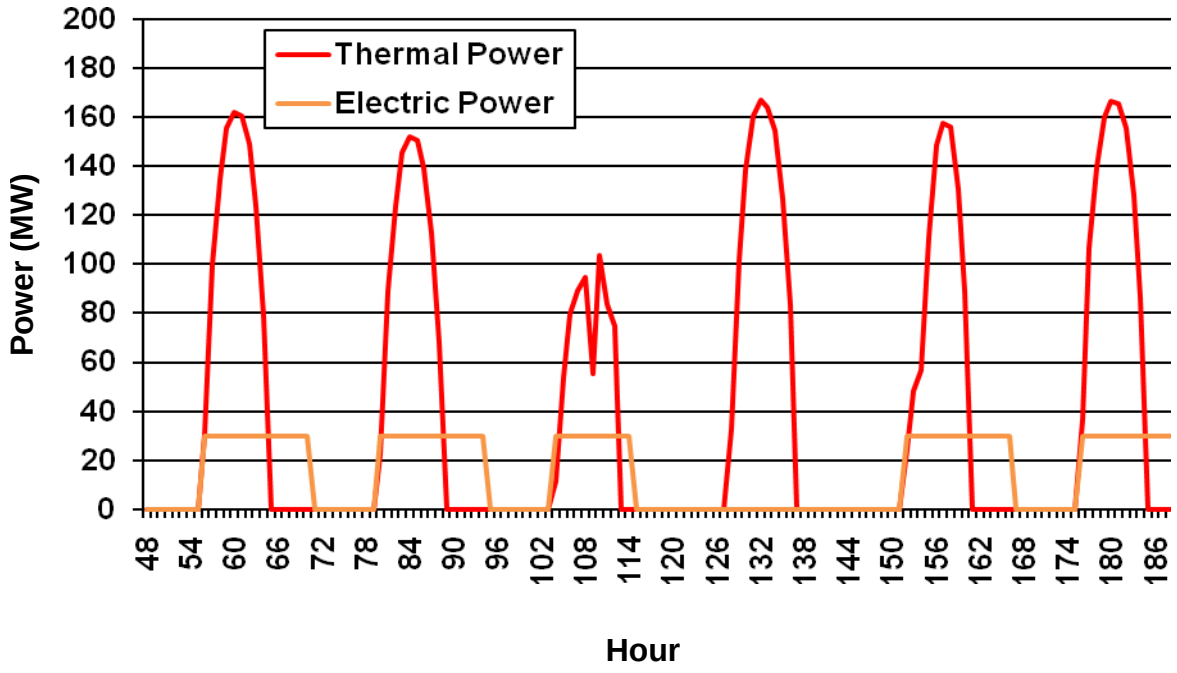

Figure 7.6: Thermal power generated by receiver (red) and electricity generated by the Rankine cycle (orange) from January 3rd through 9th in Daggett, California.

The comparison shows that the periods of significant solar radiation are much shorter for the days in January than those in July. During the winter times, the radiation is just sufficient to operate the power cycle at sunny days. For example, on January 5th (hours 96-120) the power cycle stops operation after 10 hours because the hot tank has reached its minimum fluid volume. The next day, the Rankine cycle operation is completely stopped and radiation is used to recover the tank for a full day of operation. In contrast, days in July are longer (Figure7.4) and therefore more thermal energy is accumulated to operate the cycle in every 15 hour period.

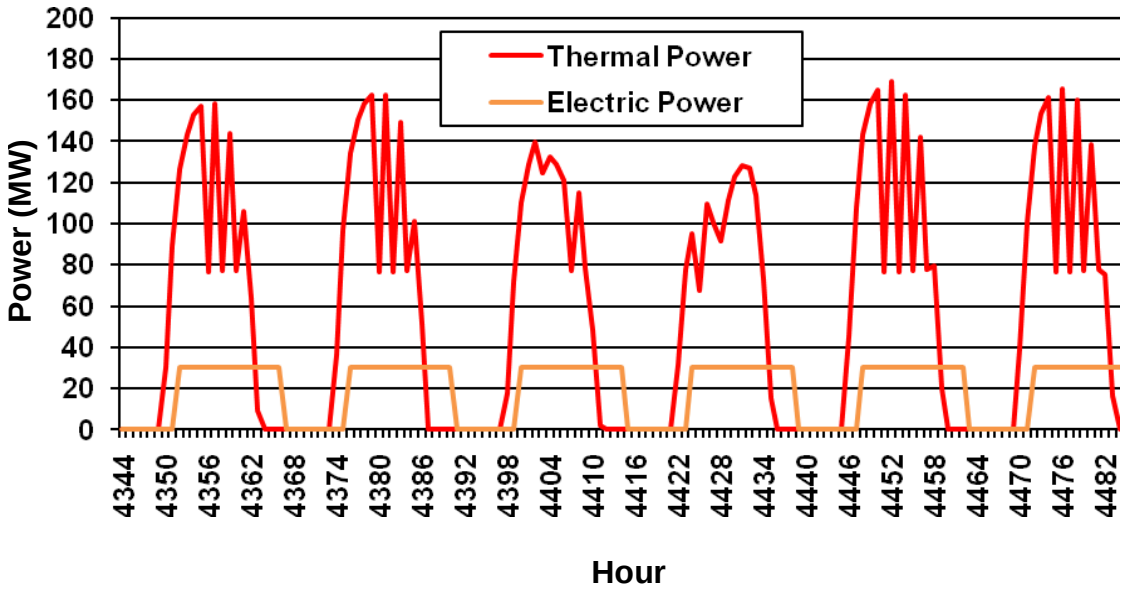

Figure 7.7: Thermal power generated by receiver (red) and electricity generated by the Rankine cycle (orange) from July 1st through 6th in Daggett, California.

In conclusion, the calculations predicted comparable performances for the two considered receiver geometries when the influence of wind flow past the receiver on the convection losses is neglected. It is assumed that wind will increase the forced convection losses from the external receiver more significantly because of the sheltering influence of the cavity shape. Furthermore, the heat losses in a cavity can be reduced by reducing the aperture size while ensuring that the spillage from the heliostat field is not increased due to a smaller aiming zone. Problems were encountered for the cavity-type CRS plant design with PTGen, which should be reviewed to produce comparable solar loads for both receiver types.

8 Conclusions and Recommendations

8.1 Summary

The main purpose of this research project was to develop a thermal model of a cavity-type receiver component for solar power towers in the TRNSYS simulation code. The model developed estimates the full thermal performance of a cavity receiver including total energy absorbed from incoming solar radiation, thermal losses, (natural convection and long-wave radiation) and total energy absorbed into a secondary heat transfer fluid. The convection losses were found to be higher than those from external receivers. This rather non-intuitive behavior agrees with experimental data from convection loss measurements on cubical cavities found in the literature (Siebers & Kraabel, 1984). Because actual measurements on large-scale cavity receivers are limited, a detailed validation of the model was not possible.

Because the cavity receiver does experience thermal losses, a portion of the incoming solar radiation from the heliostat field is lost to the surrounding ambient environment before the remaining portion can be transferred to secondary working fluid. The receiver model provides geometric flexibility in a sense that the basic shape elements are predefined (absorber surface panels approximate the inside surface of a vertical hemi-cylinder) but the length scales and quantities can be modified by the user. Different options of the coolant flow scheme were evaluated and their influence on the losses was investigated.

In attempts to provide some form of an independent verification of the cavity receiver model, comparisons of the model results with CFD simulations were made. Data for the radiation heat losses from different cavity configurations estimated with CFD methods and the TRNSYS cavity model agreed well. In contrast, the CFD model predicted higher free convection losses by a factor of 2 to 4.

Tests were also conducted for the incorporation of the receiver model into a TRNSYS two-tank plant setup, which was compared to a two-storage-tank plant that utilizes the external

receiver version by Wagner (2008). The external vs. cavity receiver comparison estimated similar overall thermal performance for both receiver types. The radiation losses are smaller for cavity due to the shielding effect of the non-cooled cavity walls surrounding the absorbing surfaces of the receiver. However, the non-cooled interior surfaces in the cavity get heated by the internal radiation exchange and contribute significantly to the higher convective losses of the cavity-type receivers. In summary, the annual receiver comparison predicts similar performances when forced convection due to wind is neglected.

8.2 Recommendations

8.2.1 Central Receiver Design

The influence of forced convection on the thermal performance is assumed to be more significant for the external receiver than for the cavity receiver. The presented results suggest that the cavity is an almost equally good candidate for the receiver shape and could even outperform the external receiver depending on the geometry (e.g. decreasing the aperture size while keeping irradiated absorption surface area constant), especially when the influence of ambient winds is considered.

Testing of eight different flow circuiting options for the coolant revealed significant differences in the thermal performance of the cavity receiver depending on the chosen flow distribution. Shortly summarized, the convection losses depend proportionally on the surface temperatures whereas the radiation losses are a function of the surface temperatures to the fourth power. Additionally the total losses are proportionally dependent on the surface area. The heat transfer modeling showed that the local surface temperature is mainly influenced by the fluid temperature at the same location. The most efficient flow distributions produce the lowest average surface temperatures assuming a constant surface area. Practically this can be obtained by concentrating the flux on a small part of the surface area which is located close to a heat transfer fluid outlet. Aside from the flow distribution, a total decrease of the receiver surface area and the receiver increases the efficiency by keeping the average surface

temperature constant due to the specified inlet and outlet fluid temperatures. The increased flux is absorbed by higher coolant flow rates. Considering that the panel materials limit the approaches of higher flux concentration, a major part of future research needs to be directed towards the development of improved absorber materials.

The efficiency of the receiver could possibly be increased by applying materials for the inactive surfaces that have very low absorptivity and therefore high reflectivity for long-wave radiation, so that a large fraction of the radiation that is emitted from the hot absorber panels gets reflected and does not heat the approximately adiabatic, inactive walls. These surfaces should be oriented such that a large fraction of the radiation is reflected in direction of the absorbing surfaces. Since the temperature profile of the active surfaces is mainly guided by the specified inlet and outlet temperatures and the flow pattern, the efficiency will increase because the flow rate is adjusted to receive the same outlet temperatures while absorbing more heat through the additionally received radiation. Furthermore, the total interior surface temperature will be lower such that also the radiation and also the convective heat losses are decreased compared to a cavity with only black interior surfaces. To simulate cavities with high-reflective, inactive, interior surfaces, a grey-body radiosity method could be included in the radiation modeling.

8.2.2 Convection Loss Estimations

As mentioned earlier, the utilized correlations for the present cavity receiver model account only for natural convection and neglect the influence of wind velocity and direction on the energy losses. Clausing (1987) pointed out that the internal resistances are dominant for the mixed convection. In detail, thermal energy is transported away from the heated interior surfaces to the bulk air flow inside the cavity. This bulk air mass is at a temperature which is not significantly higher than ambient temperature; therefore, the heat transfer coefficients for the convective energy transport are only influenced by winds if they enter the cavity and increase the flux. Clausing (1989) claims that the air flow inside the cavity is mostly driven

by buoyancy forces and that ambient wind has only a small influence in the range of common wind velocities and receiver sizes for solar power towers. However, some measurements at the IEA (International Energy Agency) receiver in Spain show different influences of the wind. Carefully conducted measurements need to be done to get a realistic estimate of the influence of wind on the cavity receiver convective heat losses. Also the natural convection correlations need further comparison to data from real receivers, because CFD simulations indicated the possibility of much higher convection loss rates than predicted with the presented correlations. Future CFD simulations must be validated against experimental data for a confident use of the results. This can be approached by starting with simplified basic cases where experimental data is easily available, for example isothermal cubical cavities. If the verification is successful, the model can be modified to predict the energy losses from more complex receiver setups.

8.2.3 PTGen/DELSOL

The PTGen program (Wagner, 2008), which utilizes the DELSOL3 code, was used to lay out the heliostat field and generate the flux maps for the solar radiation distribution on the tower. While generating heliostat fields for the external and the cavity receiver plants with equal desired electrical output in Chapter 7, a comparison showed that DELSOL3 computes a much lower annual solar load (approximately 20%) for the cavity receiver than for the external receiver. Since the thermal performances of the receivers are comparable, the cavity receiver generates less thermal energy and the power block generates less electricity than the desired 30 MW. During the present study, this problem was solved by manually adjusting the flux maps such that the solar load is equal for both plants, but for the incorporation into the Solar Advisor Model, a revision of the DELSOL performance and the settings in PTGen is required.

References

Clausing, A. (1983). Convective Losses from Solar Central Receivers - Comparisons Between Analytical Predictions and Experimental Results. *Journal of Solar Energy Engineering , 105*, 29-33.

Clausing, A. M., Lister, L. D., & Waldvogel, J. M. (1989). Combined Convection from Isothermal Cubical Cavities with a Variety of Side-Facing Apertures. *International Journal of Heat and Mass Transfer , 32*, 1561-1566.

Clausing, A. (1987). Natural Convection from Isothermal Cubical Cavities with a Variety of Side-Facing Apertures. *Journal of Heat Transfer , 109*, 407-412.

Fluent Inc. (2009). Fluent 6.3 Documentation. www.fluent.com.

Fox, R., McDonald, A., & Pritchard, P. (2006). *Introduction to Fluid Mechanics.* John Wiley and Sons, Inc.

Gross, U., Spindler, K., & Hahne, E. (1981). Shapefactor-Equations for Radiation Heat Transfer Between Plane Rectangular Surfaces of Arbitrary Position and Size with Parallel Boundaries. *Letters in Heat and Mass Transfer , 8*, 219-227.

Häberle, A., Zahler, C., Lerchenmüller, H., Mertins, M., Wittwer, C., Trieb, F., et al. (2002). The Solarmundo line focussing Fresnel collector. Optical and thermal performance and cost calculations. *International Symposium on Concentrated Solar Power and Chemical Energy Technologies.*

Kistler, B. L. (1986). A User's Manual for DELSOL3: A Computer Code for Calculating the Optical Performance and Optimal System Design for Solar Thermal Central Receiver Plants. Albuquerque, NM: Sandia National Laboratories. SAND86-8018.

Klein, S. A. (2008). EES – Engineering Equation Solver. F-Chart Software. http://www.fchart.com.

Kraabel, J. (1983). An Experimental Investigation of Natural Convection from a Side-Facing Cubical Cavity. *ASME-JSME Thermal Engineering Joint Conference Proceedings 1*, (pp. 299-306). Honolulu, Hawaii.

Krishnaprakas, C. (1997). View Factor Between Inclined Rectangles. *AIAA Journal of Thermophysics and Heat Transfer , 11* (3), 480-481.

Lata, J. M., Rodriguez, M., & Lara, M. A. (2006). *High Flux Central Receivers of Molten Salts for the New Generation of Commercial Standalone Solar Power Plants.* SolarPACES.

LeQuere, P., Penot, F., & Mirenayat, M. (1981). Experimental Study of Heat Loss Through Natural Convection From an Isothermal Cubic Open Cavity. *Proceedings DOE/SERI/SNLL Workshop on Convective Losses from Solar Receivers* (pp. 165-174). Livermore, California: Sandia national Laboratories. SAND81-8014.

Litwin, R. Z. (2002). Receiver System: Lessons Learned from Solar Two. Albuquerque, NM: Sandia National Laboratories. SAND2002-0084.

Ma, R. Y. (1993). *Wind Effects on Convective Heat Loss From a Cavity Receiver for a Parabolic Concentrating Solar Collector.* Sandia National Laboratories. SAND92-7293.

Mancini, T. R. (1997). *Solar-Electric Dish Stirling System Development.* Albuquerque, NM: Sandia National Laboratories.

Nellis, G., & Klein, S. (2009). *Heat Transfer.* Cambridge University Press.

Ortega, J. I., Burgaleta, J. I., & Téllez, F. M. (2008). Central Receiver System Solar Power Plant Using Molten Salt as Heat Transfer Fluid. *Journal of Solar Energy Engineering , 130.*

Pacheco, J. E., Reilly, H. E., Kolb, G. J., & Tyner, C. E. (2000). Summary of the Solar Two Test and Evaluation Program. Albuquerque, NM: Sandia National Laboratories. SAND2000-0372C.

Point in polygon (ray casting algorithm). (2009, November 21). *www.rosettacode.org*. Retrieved December 19, 2009, from http://rosettacode.org/wiki/Point_in_polygon_(ray_casting_algorithm)

Prakash, M., Kedare, S., & Nayak, J. (2008). Investigations on heat losses from a solar cavity receiver. *Sol. Energy* .

Richter, D. C., Teske, S., & Short, R. (2009). *Concentrating Solar Power Global Outlook 2009 - Why Renewable Energy is Hot.* Greenpeace, SolarPACES, ESTELA.

Romero-Alvarez, M., & Zarza, E. (2007). Concentrating Solar Power. In *Handbook of Energy Efficiency and Renewable Energy.* Taylor & Francis Group, LLC.

Sandia National Laboratories. (2008, February 12). *Sandia, Stirling Energy Systems set new world record for solar-to-grid conversion efficiency*. Retrieved December 17, 2009, from http://www.sandia.gov/news/resources/releases/2008/solargrid.html

Sargent & Lundy LLC Consulting Group. (2003). *Assessment of Parabolic Trough and Power Tower Solar Technology Cost and Performance Forecasts.* NREL.

Siebers, D., & Kraabel, J. (1984). *Estimating Convective Energy Losses from Solar Central Receivers.* Sandia National Laboratories. SAND84-8717.

Siegel, R., & Howell, J. R. (2001). A Catalog of Radiation Heat Transfer Configuration Factors. In R. Siegel, & J. R. Howell, *Thermal Radiation Heat Transfer.* New York: Taylor and Francis.

Solar Millennium. (2008). *The parabolic trough power plants Andasol 1 to 3. The largest solar power plants in the world – Technology premiere in Europe.* Retrieved December 17, 2009, from http://www.solarmillennium.de/upload/Download/Technologie/eng/Andasol1-3engl.pdf

Solúcar. (2006). *10 MW Solar Thermal Power Plant for Southern Spain.*

Stine, W. B., & Geyer, M. (2001). *Power From The Sun*. Retrieved December 18, 2009, from http://www.powerfromthesun.net/Chapter10/Chapter10new.htm

Stone, K., & Jones, S. (1999). *Analysis of Solar Two Heliostat Tracking Error Sources.* Sandia National Laboratories, Albuquerque, NM, and The Boeing Company, Huntington Beach, CA. SAND99-0239C.

Taumoefolau, T., Paitoonsurikarn, S., Hughes, G., & Lovegrove, K. (2004). Experimental Investigation of Natural Convection Heat Loss From a Model Solar Concentrator Cavity Receiver. *Journal of Solar Energy Engineering , 126*.

TRNSYS. (2009). TRNSYS – A Transient System Simulation Program. Thermal Energy Systems Specialists, LLC; University of Wisconsin-Madison Solar Energy Laboratory. www.trnsys.com.

U.S. Department of Energy. (2008). *Concentrating Solar Power Commercial Application Study: Reducing Water Consumption of Concentrating Solar Power Electricity Generation.* U.S. Department of Energy.

Wagner, M. J. (2008). Simulation and Predictive Performance Modeling of Utility-Scale Central Receiver System Power Plants. Madison, Wisconsin: Solar Energy Laboratory, University of Wisconsin-Madison.

Appendices

The main code for the TRNSYS component is enclosed as a digital supplement that is attached to this thesis (further description in Appendix D). Note that Appendix B only shows one of the six ray-tracing subroutines. The remaining view factor routines are also provided in Appendix D.

Appendix A: Analytical View Factor Routine

The program that calculates all view factors between vertical surfaces as described in Section 3.2.2.1 uses the EES subroutines F3D_30. This subroutine was written during the course of this research and included in the standard EES view factor library.

```
"View factor calculcations for the given PS10 geometry"

"Instructions: Specify receiver specifications under 'Receiver data'.  This programs returns the view factors from each panel 1-4, counted from one outer panel to the other side (assuming symmetric setup), to its surroundings."

$tabstops 1 2 4 6 8 cm
$UnitSystem SI MASS RAD PA C K J

Procedure panelviewfactors(N,theta,R,H,L:F_A_B[1..n],F_A_C[1..n],F_A_D[1..n],F_A_O[1..n],F_A_L[1..n],F_B_O[1..n],F_B_L[1..n])

"Geometric relations"
alpha  = theta/4
H_N    = H/N                  "height of a panel node"
W      = 2*R*sin(alpha/2)     "panel width if panels have equal size"
c      = 2*R*sin(PI-2*alpha)  "distance between the vertical aperture edges if the aperature is considered to be at the outer edges of the outer panels"
z      = R*cos(PI-2*alpha)    "distance between the aperature plane and the centerline of the panel circle"
phi_1  = PI-alpha             "angle between two adjacent panels"
phi_2  = PI-2*alpha           "angle between two non-adjacent panels with one panel in between"
phi_3  = PI-3*alpha           "angel between two non-adjacent panels with two panels in between"
phi_4  = (theta-alpha)/2      "angle between the aperture plane and an outer panel (1)"
phi_5  = alpha/2              "angle between the aperture plane and an inner panel (2)"
a_1    = W/(2*cos(alpha))     "distance from inner panel edge to intersection edge of both panel planes for view factor calculation of panels with one panel in between"
a_2    = R*sin(alpha)/sin((pi-3*alpha)/2)      "distance from inner panel edge to intersection edge of both panel planes for view factor calculation of panels with two panels in between"
```

```
a_3      = (R+z)/sin(alpha/2)-W              "distance from panel 2 to intersection edge of panel planes 2 and a"
a_4      = (R+z)/tan(alpha/2)-c/2            "distance from panel a to intersection edge of panel plane 2 and a"

i:=0
REPEAT
        i:=i+1;

        "View factors between nodes of panel A and nodes of panel B"
        F_A_B[i] = F3D_30(0[m],W,0[m],H_N,(i-1)*H_N,i*H_N,0[m],W,phi_1)
        "View factors between nodes of panel A and nodes of panel C"
        F_A_C[i] = F3D_30(a_1,a_1+W,0[m],H_n,(i-1)*H_n,i*H_n,a_1,a_1+W,phi_2)
        "View factors between nodes of panel A and nodes of panel D"
        F_A_D[i] = F3D_30(a_2,a_2+W,0[m],H_n,(i-1)*H_n,i*H_n,a_2,a_2+W,phi_3)
        "View factors between nodes of panel A and opening (O)"
        F_A_O[i] = F3D_30(0[m],W,(i-1)*H_n,i*H_n,L,H,0[m],c,phi_4)
        "View factors between nodes of panel A and lip (L)"
        F_A_L[i] = F3D_30(0[m],W,(i-1)*H_n,i*H_n,0[m],L,0[m],c,phi_4)
        "View factors between nodes of panel B and opening (O)"
        F_B_O[i] = F3D_30(a_3,a_3+W,(i-1)*H_n,i*H_n,L,H,a_4,a_4+c,phi_5)
        "View factors between nodes of panel B and opening (L)"
        F_B_L[i] = F3D_30(a_3,a_3+W,(i-1)*H_n,i*H_n,0[m],L,a_4,a_4+c,phi_5)

UNTIL (i>=N)

End

"Receiver data"
N        = 10                               "number of nodes in the vertical direction"
R        = 5.358 [m]                        "radius of circle where the common panel edges are located"
theta    = 180[deg]*convert(deg,rad)        "angle of that circle which is covered by panels"
H        = 12 [m]                           "panel height"
L        = 3 [m]                            "height of the upper lip"

H_N      = H/N
W        = 2*R*sin(alpha/2)                 "panel width if panels have equal size"
alpha    = theta/4
c        = 2*R*sin(PI-2*alpha)              "distance between the vertical aperture edges if the aperature is considered to be at the outer edges of the outer panels"

Call
panelviewfactors(N,theta,R,H,L:F_A_B[1..N],F_A_C[1..N],F_A_D[1..N],F_A_O[1..N],F_A_L[1..N],F_B_O[1..N],F_B_L[1..N])

$SaveTable 'Arrays' 'viewfactors.csv'
```

Appendix B: Monte-Carlo Ray-Tracing Routine

The Monte-Carlo ray-tracing routine that calculates the view factors from all vertical nodes of an outer receiver panel to the bottom surface is listed below. It makes use of the *Points_Module* and the *Ray_Casting_Algo* modules that include the *point-in-polygon* routines. These modules and the subroutines for the remaining view factors are saved on the enclosed disc.

```
!View factor calculation via Monte Carlo Ray Tracing
!technique for the cavity receiver model
!by Lukas Feierabend

subroutine OuterPanel_Floor(N_nodes,H_rec,H_lip,R_rec,RecAngle,F_AF)
! view factor from all the nodes of an outer panel to the floor surface
use Points_Module
use Ray_Casting_Algo
implicit none
! Inputs
! N_nodes   number of panel H_node in the vertical direction
! H_rec     receiver panel height
! R_rec     radius of circle where the common panel edges are located
! RecAngle  section of circle which is covered by panels

! Outputs
! F_AF      view factor array for panel A

integer::N_nodes,N,ict,hit,i
double precision::alpha,RecAngle,H_node,H_rec,H_lip,W,c,R_rec,R1,R2,&

x,y,yv(5),zv(5),yvR(4),zvR(4),Ptheta,theta,Pphi,phi,y_i,z_i
double precision,dimension(N_nodes),intent(out)::F_AF
double precision,parameter::pi=3.14159265
type(polygon):: targetpolygon
type(point):: pts(5),p
logical::inside
integer,dimension(N_nodes)::hits


! number of rays to generate
N = 500000

! Geometric calculations
alpha = RecAngle*0.25                ! angle coverage of the receiver
circle by each of the 4 panels
H_node = H_rec/dble(N_nodes)         ! height of a panel node
W = 2.d0*R_rec*sin(alpha/2.d0)         ! panel width if panels have equal
size
```

```
c = 2.d0*R_rec*sin(pi-2.d0*alpha)    ! distance between the vertical
aperture edges if the aperature is considered to be at the outer edges of
the outer panels


! Vertices of the floor polygon
yv = (/0.d0, W, W*(1.d0+cos(alpha)),
W+2.d0*R_rec*sin(alpha)*cos(alpha+acos(R_rec*sin(alpha)/W)),
c*cos(3.d0/2.d0*alpha)/)
zv = (/0.d0, 0.d0, W*sin(alpha),
2.d0*R_rec*sin(alpha)*sin(alpha+acos(R_rec*sin(alpha)/W)),
c*sin(3.d0/2.d0*alpha)/)
! Create the polygon
pts = (/ point(yv(1),zv(1)), point(yv(2),zv(2)), point(yv(3),zv(3)),
point(yv(4),zv(4)), point(yv(5),zv(5))/)
targetpolygon = create_polygon(pts, (/ 1,2, 2,3, 3,4, 4,5, 5,1 /) )
! Vertices of the bounding box for the polygon
yvR = (/0.d0, W*(1.d0+cos(alpha)), W*(1.d0+cos(alpha)), 0.d0/)
zvR = (/0.d0, 0.d0, c*sin(3.d0/2.d0*alpha), c*sin(3.d0/2.d0*alpha)/)

!Initialize random number generation
CALL RANDOM_SEED
!Initialize ray and hit counters
ict = 0
hits = 0
do
    ! ray counter
    ict = ict+1
    if(ict>N) exit
    do i = 1,N_nodes
        ! randomly selected ray direction
        call RANDOM_NUMBER(Ptheta)  ! uniformly distributed random number
between 0 and 1
        call RANDOM_NUMBER(Pphi)    ! uniformly distributed random number
between 0 and 1
        theta= asin(sqrt(Ptheta))   ! determine the polar angle
        phi=Pphi*2.d0*pi             ! determine the azimuthal angle

        ! check if ray goes through floor plane
        if ((pi/2.0.LE.phi.AND.phi.LE.3.0/2.0*pi).OR.(theta.EQ.0.0)) then
            hit=0                                    ! 0 indicates that
the ray does not hit the surface
        else
            ! randomly selected ray origin
            call RANDOM_NUMBER(R1)
            call RANDOM_NUMBER(R2)
            x = (dble(i)-1.0+R1)*H_node
            y = R2*W
            ! determine the intersection point
            y_i = y+tan(phi)*(H_rec-x)
            z_i = (H_rec-x)/(cos(phi)*tan(theta))
            if (y_i<yvR(1)) then
                hit=0
            elseif (y_i>yvR(2)) then
```

```
                hit=0
            elseif (z_i<zvR(1)) then
                hit=0
            elseif (z_i>zvR(4)) then
                hit=0
            else
                p = point(y_i,z_i)
                inside = point_is_inside(p, targetpolygon)
                if(inside) then
                    hit=1
                else
                    hit=0
                endif
            endif
        ! hit counter
        if (hit.EQ.1) hits(i) = hits(i)+1
        endif
    enddo
enddo

do i = 1,N_nodes
    F_AF(N_nodes+1-i) = DBLE(hits(i))/DBLE(ict)
enddo


end subroutine
```

Appendix C: TRNSYS Plant Setup

Inputs and parameters for the plant components as shown in Figure 7.4 for the annual cylindrical vs. cavity receiver comparison in Chapter 7 are listed in the tables below.

Heliostats (Type 221)		
Parameters	**Value/Connection**	**Units**
Unit no of Input file	10	-
No of zenith angle data points	8	-
No of azimuth angle data	12	-
Number of heliostats	0	-
startup energy of unit	0	J
power to track 1 unit	0	kJ/hr
max allowed windspeed	999.9	m/s
Inputs	**Value**	**Units**
wind speed	Weather data	m/s
Defocus factor	Weather data	-
solar zenith angle	Weather data	-
solar azimuth angle	Weather data	-
External Files		
eff_array.dat		

Cavity Receiver (Type 230)		
Parameters	**Value/Connection**	**Units**
Cavity Radius	8	m
Cavity Height	10.56	m
Lip Height	0.96	m
Tower Height	140	m
Receiver Angles	180	degrees
Logical Unit for the Flux Map File	57	-
Outer Fluid Tube Diameter	63.5	mm
Tube Wall Thickness	4.19	mm
Heat Transfer Fluid	1	-
Flow Pattern	6	-
Logical Unit for the Status File	58	-
Logical Unit for the Viewfactor File	59	-
Inputs	**Value**	**Units**
Hour of the Day	Weather data	hr
Solar Azimuth Angle	Weather data	degrees
Solar Zenith Angle	Weather data	degrees
Ambient Temperature	Weather data	C
Dew Point Temperature	Weather data	C
Ambient Pressure	Weather data	atm
HTF Pressure	1.01325	bar
Direct Normal Radiation	Weather data	kJ/hr-m2
Field Efficiency	Heliostats (Type 221)	-
Pump Efficiency	0.8	-
Heliostat Stow Solar Angle	5	degrees
Cold Inlet Temperature of the HTF	Cold Tank (Type 39)	C
Hot Outlet Temperature of the HTF	565.0	C
External Files		
fluxmap.csv		
viewfactors.csv		

External Receiver (Type 222)		
Parameters	**Value/Connection**	**Units**
Number of panels	12	-
Receiver diameter	7.796	m
Panel height	10.56	m
Tower height	100	m
Tube outer diameter	63.5	mm
Tube wall thickness	4.19	mm
Material	1	-
Coolant	1	-
Flow pattern	2	-
Plant latitude	35	degrees
Logical Unit	50	-
Emissivity	1.0	-
Efficiency Factor	1.0	-
Flux Elevation Points	1.0	-
Azimuthal Flux Points	12.0	-
Inputs	**Value**	**Units**
azimuth	Weather data	degrees
zenith	Weather data	degrees
Outlet fluid temp	565	C
Inlet fluid temp	Cold Tank (Type 39)	C
Wind velocity	Weather data	m/s
Ambient pressure	Weather data	atm
Pump efficiency	0.8	-
Hour of the day	Weather data	hr
Dewpoint temperature	Weather data	C
Direct Normal Radiation	Weather data	kJ/hr-m2
Field eff	Heliostats (Type 221)	-
Dry Bulb temperature	Weather data	C
Night Recirculation Mode	0	-
Heliostat Deploy Angle	5.0	-
External Files		
fluxmap.csv		

Hot Tank (Type 39)		
Parameters	**Value/Connection**	**Units**
Tank operation mode	1	-
Overall tank volume	15000	m3
Minimum fluid volume	100	m3
Maximum fluid volume	14900	m3
Tank circumference	97.12	m
Cross-sectional area	750	m2
Wetted loss coefficient	.1	kJ/hr-m2-K
Dry loss coefficient	.1	kJ/hr-m2-K
Fluid specific heat	1.545	kJ/kg-K
Fluid density	1729	kg/m3
Initial fluid temperature	565	C
Initial fluid volume	7500	m3
Inputs	**Value**	**Units**
Inlet temperature	Receiver (Type 222/230)	C
Inlet flow rate	Receiver (Type 222/230)	kg/hr
Flow rate to load	Plant Control (Type 223)	kg/hr
Environment temperature	Weather data	C

Cold Tank (Type 39)		
Parameters	**Value/Connection**	**Units**
Tank operation mode	1	-
Overall tank volume	15000	m3
Minimum fluid volume	100	m3
Maximum fluid volume	14900	m3
Tank circumference	97.12	m
Cross-sectional area	97.12	m2
Wetted loss coefficient	.1	kJ/hr-m2-K
Dry loss coefficient	.1	kJ/hr-m2-K
Fluid specific heat	1.499	kJ/kg-K
Fluid density	1905	kg/m3
Initial fluid temperature	290	C
Initial fluid volume	7500	m3
Inputs	**Value**	**Units**
Inlet temperature	Rankine Cycle (Type 224)	C
Inlet flow rate	Rankine Cycle (Type 224)	kg/hr
Flow rate to load	Plant Control (Type 223)	kg/hr
Environment temperature	Weather data	C

Rankine Cycle (Type 224)		
Parameters	**Value/Connection**	**Units**
Reference Power	30000	kW
Reference Efficiency	0.34	-
Reference heat source inlet temp	565	C
Reference heat source outlet temp	290	C
Reference condenser water dT	20	C
HTF specific heat slope	0.00020562	any
HTF specific heat constant	1.4326514	J/kg-K
Standby mode thermal fraction	0.15	-
Boiler Saturation Pressure	100	BAR
Inputs	**Value**	**Units**
Mode of operation	1	-
Heat source inlet temperature	Hot Tank (Type 39)	C
Heat transfer fluid mass flow rate	Plant Control (Type 223)	kg/hr
Cooling water inlet temp	12.8	C
Cooling water mass flow rate	Cal. ref. CW rate (Type224)	kg/hr
Demand variable	30000	any
Standby control	Plant Control (Type 223)	-

Plant Control (Type 223)		
Inputs	**Value/Connection**	**Units**
Hour of the day	Weather data	hr
Start hour	8	hr
End hour	23	hr
Solar zenith angle	Weather data	degrees
Storage hot outlet temp	Hot Tank (Type 39)	C
Min temp to load	500	C
Load flow demand	Rankine Cycle (Type	kg/hr
Storage cold outlet temp	Cold Tank (Type 39)	C
Max temp to heat source	350	C
Flow from heat source	Receiver (Type 222/230)	kg/hr
Temp from heat source	Receiver (Type 222/230)	C
Hybridization mode	0	-
Cycle standby period	2	hr
Maximum flow rate to heat source	3000000	kg/hr
Hot Tank Volume Level	Hot Tank (Type 39)	-
Cold Tank Volume Level	Cold Tank (Type 39)	-
Actual hot tank HTF volume	Hot Tank (Type 39)	m3
Standby mode thermal fraction	0.15	-
Reference HTF Mass flow rate	Rankine Cycle (Type	kg/hr
HTF fluid density	1850	kg/m3

Appendix D: Digital Supplement

The digital supplement to this thesis contains all relevant codes for the view factor modeling and the thermal receiver modeling. The disc (CD-ROM) contains three folders (i.e. EES cavity receiver files, TRNSYS cavity receiver files, and view factor files). The following provides a brief description of the enclosed files.

EES cavity receiver files:

1. cavity receiver model – initial clausing model – uniform flux.EES:

The cavity receiver model uses the 1983 Clausing model to compute the natural convection losses. The solar flux is uniformly distributed across the absorbing surfaces.

2. cavity receiver model – initial clausing model.EES:

Same as 1, except a prototypical flux map is applied.

3. cavity receiver model – initial clausing+updated clausing model.EES:

The natural convection losses are calculated with an approach that combines the 1983 and 1987 Clausing models to estimate the influence of convection on the surface temperatures.

4. cavity receiver model – siebers & kraabel – uniform flux.EES:

The Siebers & Kraabel convection model is used to calculate natural convection losses. The solar flux is uniformly distributed across the absorbing surfaces.

5. cavity receiver model – siebers & kraabel.EES:

Same as 4, except a prototypical flux map is applied.

6. cavity receiver model – updated clausing – uniform flux.EES:

The 1987 Clausing convection model is used to calculate natural convection losses. The solar flux is uniformly distributed across the absorbing surfaces.

7. cavity receiver model – siebers & kraabel.EES:

Same as 6, except a prototypical flux map is applied.

TRNSYS cavity receiver files:

Type230.for:

This is the final TRNSYS component code for the cavity-type solar central receiver.

Type230 – properties not averaged.for:

The code formulation in this receiver component allows for property evaluation at the coolant temperature of every radiation node.

view factor files:

view factors cavity receiver.EES:

The EES program calculates the view factors between all vertical surfaces in the cavity. A listing of this program is included in Appendix A.

modules.f90:

The Fortran code contains modules and routines for the "point-in-polygon" checks that are used in the view factor ray-tracing algorithms.

viewfactors.f90:

This Fortran file contains the Monte-Carlo ray-tracing algorithms to calculate the view factors between the vertical surfaces in the cavity and the horizontal bottom and top surface, respectively.